TECHNISCHE UNIVERSITÄT MÜNCHEN
LEHRSTUHL FÜR HOCHFREQUENZTECHNIK

Driven Eigenproblem Computation for Periodic Structures

Huanlei Chen

Vollständiger Abdruck der von der Fakultät für Elektrotechnik und Informationstechnik der Technischen Universität München zur Erlangung des akademischen Grades eines

- *Doktor-Ingenieurs* -

genehmigen Dissertation

Vorsitzender :		Univ.-Prof. Dr.-Ing. Eckehard Steinbach
Prüfer der Dissertation :	1.	Univ.-Prof. Dr.-Ing. Thomas Eibert
	2.	Prof. Dr. Wenquan Che, Nanjing University of Science and Technology/China

Die Dissertation wurde am 15.04.2013 bei der Technischen Universität München eingereicht und durch die Fakultät für Elektrotechnik und Informationstechnik am 30.09.2013 angenommen.

Contents

Acknowledgement

I would like to thank Prof. Dr.-Ing. Thomas Eibert for giving me the opportunities to study in the Lehrstuhl für Hochfrequenztechnik, Technische Universität München, Munich, Germany. His motivation and advice inspired me in both study and life. I also must say thanks to the International Graduate School of Science and Engineering (IGSSE) of TUM for sponsoring me through my study and every conference. The help from the collaborative Nanjing University of Science and Technology, Department of Communication Engineering, Nanjing, especially Prof. Wenquan Che and the other colleagues Wenjie, Yumei and so on are unforgettable. Without them my international exchange can no be so successful. I am specially grateful to Dr.-Ing. Carsten Schmidt and Prof. Dr.-Ing. Uwe Siart for their valuable supports. Moreover I would like to dedicate this work to my family. My parents in China always give me the courage to complete this work. My husband Libo Huang stands beside me and plays all kinds of roles like adviser, reviewer and critic. His help is the solid foundation in the successful completion of my studies. Finally I would like to thank my upcoming baby for his cooperation during the thesis writing. Although being exhausted and encountering a big change of life, I still deeply appreciate the happiness he brings.

Abbreviations and Symbols

ABC	absorbing boundary condition
$ABCD$-matrix	transmission matrix with respect to voltage and current
$\boldsymbol{B}$	magnetic flux density
C	capacitor
CRLH	composite right-/left-handed
BI-RME	boundary integral-resonant mode expansion method
$\boldsymbol{D}$	electric displacement vector
$\boldsymbol{E}$	electric field
EC	evolutionary computation
EM	eigenmode
ES	evolution strategy
EV	eigenvalue
FDFD	finite difference frequency domain
FDTD	finite difference time domain
FEBI	finite element boundary integral
FEM	finite element method
FSIW	folded substrate integrated waveguide
GO	geometrical optics
GP	genetic programming
GTD	geometrical theory of diffraction
$\boldsymbol{H}$	magnetic field vector
HMSIW	half mode substrate integrated waveguide
k''	attenuation constant
k'	phase constant
ε_0	$8.858 \cdot 10^{-12}$ F/m, permittivity of free space
ε_r	relative permittivity
k	wavenumber
$\boldsymbol{k}$	wavevector
L	inductor
LH	left hand
LHMs	left-handed materials
LTCC	low temperature co-fired ceramic
MFS	method of fundamental solutions
MCMC	Markov chain Monte Carlo
MoL	method of lines

MoM	method of moments
MTM	metamaterial
MP	matrix-pencil
MW	magnetic wall
λ	wavelength
λ_g	guided wavelength
λ_0	wavelength in free space
LCS	learning classifier system
μ_0	$4\pi \cdot 10^{-7}$ Vs/(Am), permeability of free space
μ_r	relative permeability
∇	Nabla operator, gradient
$\nabla\cdot$	divergence operator
$\nabla\times$	curl operator
PBC	periodic boundary condition
PCB	printed circuit board
PEC	perfect electric conductor
PMC	perfect magnetic conductor
PML	perfectly matched layer
PO	physical optics
PTD	physical theory of diffraction
RH	right hand
RO	random optimization
RSIW	ridged substrate integrated waveguide
SA	simulated annealing
$\boldsymbol{S}$-matrix	scattering matrix
SIW	substrate integrated waveguide
SMA	scattering matrix approach
SRR	split-ring resonator
STUN	stochastic tunneling
$\tan\delta$	loss factor
TEM	transverse electromagnetic wave
TL	transmission line
TrL	the numerical thru-line calibration method
TW	thin-wire
$\triangle = \nabla^2$	Laplace operator
v_p	phase velocity
v_g	group velocity
ω_{0m}	magnetic resonant frequency
ω_{pe}	electric plasma frequency
ω_{pm}	magnetic plasma frequency
ω_{se}	series resonant frequency
ω_{sh}	shunt resonant frequency

1 Abstract

With increasing operating frequencies, new microwave structures with the advantages of low loss and high quality factor for microwave, millimeter wave or even terahertz frequencies have come into research focus. One promising structure is the substrate integrated waveguide (SIW) which constructs the traditional hollow waveguide in a planar printed circuit board (PCB) with the characteristics of high density integration ability, low cost, low losses and high quality factor. One of the other research tendencies is to create a new kind of materials with negative permittivity and permeability simultaneously which are called metamaterials. These two new technologies both employ periodic configurations which normally have fine details, large size, open geometry and induce big difficulties in modeling the electromagnetic fields inside and outside the structures. Principally any electromagnetic field problem in source free region can be treated as an eigenproblem without excitation. The eigenproblem in a periodic structure normally requires more discretization due to the complicated configuration which leads to a considerable number of unknowns. Therefore, the eigenproblem in a periodic structure is usually complicated and even nonlinear. The existing modeling method for metamaterials based on the composite right-/left-handed transmission line theory restrains its application to certain types of waves, normally TEM modes, by purely describing the circuit with voltage and current. Some other numerical methods based on the classical eigenvalue solvers with the aid of the method of moments or FDTD may face the problem of bad convergence especially for the large size of the numerical systems which are induced by periodic structures.

This work proposes a novel driven eigenproblem computation method to solve the eigenproblem in periodic structures. Comparing with the purely mathematical eigenproblem solvers, the driven method is to solve the periodic eigenproblem by solving the corresponding excitation problem in the domain of the eigenvalue. For large numerical systems, solving the corresponding driven problems is normally less demanding than solving directly the eigenproblems. On the other hand according to Floquet's theorem the wave propagation in a periodic structure can be solved inside one unit cell with the defined periodic boundary conditions. The analogy between the eigenproblem and the resonator makes it possible to analogize the eigenproblem of the unit cell of the periodic structure to the one of a resonator whose eigenvalues are the resonance frequencies. The same as the resonator in electrical circuits, an internal or external excitation can be applied to the unit cell and a norm of the solution like the electric field dependent on the varying eigenvalue is observed. The driven method is employed for the dispersion and attenuation analysis of periodic waveguiding configurations.

Different types of excitations to the equivalent resonator are available, one is by using ports and the other is by distributed current densities. The port excitations can be appropriately coupled to the field of the equivalent resonator which analogizes the unit cell. Circuit theory can be used to regularize the field and calculate the energy transmission and the losses in the equivalent resonator. On the other hand distributed current densities, for example impressed volume current densities with different distributions or polarizations have the advantage of the specific mode selection as well as the all-mode excitation. Corresponding to the different types of excitations, the driven method is implemented in two solvers, respectively. One is the commercial numerical solver CST Microwave Studio (CST MWS) and the other is the hybrid finite element-boundary integral-solver (FEBI). The implementation in CST Microwave Studio with limited boundary flexibility works well in small attenuation scenarios where the perturbation technique is employed for the loss analysis of the propagating wave. On the contrary the implementation in FEBI with the doubly periodic setting is more robust for the one- or two-dimensional artificial material compositions like metamaterials and suitable for both small and large attenuation scenarios. FEBI works with an edge-based periodic boundary condition (PBC) based on FEM interior to the boundary. Exterior to the boundary a surface integral equation formulation with a Floquet mode based periodic Green's function is applied to fully account for the radiation and scattering of open structures. Lossy materials can be directly considered by supporting the complex wavevector within the periodic boundary conditions and the Green's functions.

In the driven resonator model, the resonance is always accompanied with an extremum of some electromagnetic observables, e.g. the electrical field. This makes the search of the eigenvalue, which is the resonance frequency in the resonator model, equivalent to a maximization process. Since the wavevector is complex in the lossy system, the maximization will be on the complex plane of the wavevector which actually leads to a multi-dimensional maximization. With the start vector estimation based on the previous solutions, the driven method requires the repeated iterations of solutions of excitation problems with slightly varying parameters. Some optimization techniques are employed to achieve fast convergence in one or more dimensional searching. After providing the theoretical background, a series of application examples are presented. First, the dispersion behavior of a classical rectangular hollow waveguide is analyzed by the driven method and compared with the analytical results stated in the literature to verify the driven method. Then one SIW with uniform cross section in wave propagation direction and small radiation loss is modeled in a unit cell with the driven method and the dispersion and attenuation curves match to the results from a longer model with the same unit cell configurations in CST MWS. Next a composite right-/left-handed (CRLH) waveguide, which is implemented by the SIW technology, is also modeled by the driven method with port excitations. Comparing with other modeling methods like the scattering matrix approach or the matrix pencil technique, the driven method can generate accurate results in the dispersion analysis. The examples of a grounded dielectric corrugated leaky wave antenna (LWA) and a metamaterial based on the so-called mushroom structure exhibit the versatility of the driven method in analysis of 1- and 2- dimensional periodic structures and multi-mode operations.

2 Introduction

2.1 Background

Microwave devices and components are playing a more and more important role in modern communication, remote sensing, automotive industry and bioelectromagnetic applications. But the increasingly sophisticated designs, the complex structures and the higher operating frequency range on the other hand make the modeling of the electromagnetic field inside and outside the components a big challenge. Basically all the electromagnetic problems can be represented in Maxwell's equations of the differential or integral forms with the corresponding boundary conditions to find the solution. Unfortunately, Maxwell's equations can be solved analytically only for a very few idealized geometries. However, thanks to the development of the computer technology, the accurate and complete analysis of complex microwave structures can be achieved by solving Maxwell's equations numerically. Maxwell's equations can be considered as eigenproblems, whose eigenvalues and eigenvectors sufficiently characterize the system under analysis. There are a variety of numerical methods for solving the eigenproblem of electromagnetics in either the time domain or the frequency domain. Time-domain methods model the transient behavior of the field and solve simultaneously many frequencies. Frequency-domain methods solve one frequency at a time. The solutions in the two domains can be transformed to each other by the Fourier transforms.

The three fundamental numerical methods which are the finite differences, the finite elements, and the moment methods have a long history and are well developed. The most widely used methods are the finite-difference time-domain (FDTD) method [Yee, 1966], the finite element method (FEM) [Cesari & Abel, 1972], the method of moments (MoM) solution of integral equation formulations [Harrington, 1968], the high-frequency methods like the geometrical optics (GO) [Schuster, 1904], [Greivenkamp, 2004], the physical optics (PO) [Akhmanov & Nikitin, 1997], [Asvestas, 1980], the geometrical theory of diffraction (GTD) [Keller, 1962], the physical theory of diffraction (PTD) [Ufimtsev, 2007], as well as hybrid methods which combine the different methods together, e.g. the hybrid finite-element boundary-integral method (FEBI) [Eibert et al., 1999] and so on. However, almost all of the numerical methods follow certain steps to model the problems. They all begin with discretizing the continuous unknown quantities like fields or currents in spatial or temporal domains into a computer-handleable set of finite quantities. Normally the finer the discretization is, the more accurate the result can be, but at the same time the more memory of the computer and the heavier computation load are needed. The electromagnetic quantities can be approximated by a set of expansion functions which transform the eigenproblems into a linear algebraic equation system. These algebraic equations are solved to determine the unknown coefficients of the expansion functions and finally the electromagnetic fields or currents can be interpreted. The different methods employ variant strategies to solve the unknown coefficients, for example the inversion of large matrices, implicit and explicit iteration schemes, evolutionary algorithms, random walks and the combinations of them. Although the numerical solvers have been developed for a long time, they are still facing difficulties in solving the eigenproblems for large numerical system, e.g. unsatisfied convergence for periodic structures. Many electromagnetic field problems can even evoke nonlinear eigenproblems which are even more challenging to solve. Therefore, many eigenproblem computations are restricted to small problem size like the dispersion analysis of waveguides where only one- or two-dimensional problems are needed to be solved.

2.2 Motivation

In recent researches, periodic structures attract more and more interest. In 1968, a substance with the character of "simultaneously negative permittivity ε and permeability μ", so called the left-handed (LH) effect, was firstly theoretically speculated in [Veselago, 1968]. The substance was named metamaterial whose name itself stands for artificially structured materials while none of them has been found in nature until now. In 2000, the first experimental demonstrator of a metamaterial with negative ε and μ in a certain frequency range was proposed in [Smith et al., 2000]. Small inhomogeneous components like thin-wires and split-ring resonators, whose average sizes are much smaller than the guided wavelength, create an effective macroscopic homogeneous behavior. However, the lossy and narrow band characteristics make this kind of designed composition not a good solution for realistic applications. After that an engineering approach of designing metamaterials by using the well-known lumped-element equivalent circuit model was developed. The composite right/left-handed transmission line (CRLH TL) method realized the left-handed effect in a certain frequency range together with the natural right-handed lumped or distributed circuit elements [Caloz & Itoh, 2002], [Oliner, 2003], [IYER & Eleftheriades, 2002]. The LH effect makes metamaterials a good choice for antennas, frequency selective surfaces, absorber materials, superlens, and cloaking devices and many other applications. The majority of up-to-date conceived CRLH TL configurations are based on microstrip line designs and sometimes on substrate integrated waveguides (SIWs), especially at millimeter and terahertz frequencies. SIW is a hybrid technology which emulates a dielectric filled hollow waveguide in a planar structure, e.g. a printed circuit board (PCB), by replacing the vertical side walls of the waveguide with lateral rows of vias [Bozzi et al., 2009]. The quasi closed configuration gives SIWs a better power handling capacity compared to microstrip lines. Also the planar configuration makes SIWs easily compatible to other integrated circuits. However, in the high frequency range the radiation losses due to the periodic lateral openings in SIWs can not be omitted. Both metamaterials and SIWs employ periodic configurations. Consequently the large scale, the fine details and the unclosed geometry of the metamaterials and SIWs make their modeling complicated complex eigenproblems. The existing circuit-based modeling method like CRLH TL for metamaterials describes the structures under analysis with voltages and currents restrained to some certain waves, e.g. the TEM mode, and is not sufficient for modeling of arbitrary waveguiding structures with sometimes inhomogeneous material filling and multi-mode operation. On the other hand, periodic structures like metamaterials and the SIWs with two- or even three-dimensional periodic configurations will evoke eigenproblems with a considerably large number of unknowns. This places big challenges for the classical numerical eigenproblem-based methods. The classical eigenproblem solvers which try to solve directly the eigenproblem from a mathematical point of view, can always find difficult convergence and bad accuracy especially in large and often open eigenproblem systems as found for periodic structures.

2.3 Focus of this Work

The popularity of periodic structures and their modeling difficulties motivate us to find an efficient way to solve the eigenproblems of periodic structures. This work investigates a novel driven eigenproblem computation method to solve the eigenproblem of periodic microwave structures. Compared to the purely mathematical eigenproblem solvers, the driven method solves the periodic eigenproblem by solving the corresponding excitation problem in the domain of the eigenvalue with less computation effort than directly solving the source-free eigenproblem. The analogy between the eigenproblem and the resonator opens up an opportunity to transfer the eigenproblem into a resonator where the eigenvalues are the resonance frequencies. According to the Floquet's theorem the periodic structure can be analyzed in one unit cell with periodic boundary conditions which greatly reduces the problem domain and computation efforts. Similar as for a resonator in electrical circuits, an internal or external excitation can be applied to the equivalent resonator which analogizes to the eigenproblem under consideration and a norm of the solution dependent on the varying eigenvalues is observed to find out the resonance frequencies.

Different types of excitations are available for the equivalent resonator. External excitations like port excitations can be designed to well couple to the field of the equivalent resonator which can be transformed to an equivalent circuit. Microwave network theory as e.g. in form of the scattering matrix can then be used to analyze the field problem. The internal excitations like the distributed volume current densities inside the solution domain with different distributions or polarizations can stimulate one certain mode as well as all the relevant modes. Different excitation methods can be implemented in different solvers. The port excitation is implemented in CST Microwave Studio [CST, 2011] within the frequency domain solver. However, the limited periodic boundary condition flexibility restricts this implementation to small-attenuation scenarios where the perturbation method is employed to analyze the power loss in the structures. On the contrary, the distributed current density excitation which is implemented with the hybrid finite-element boundary-integral solver (FEBI) [Eibert et al., 1999] can model the doubly periodic configurations and take the attenuation directly into account by supporting the complex wavevector in the boundary conditions. Therefore, the implementation in FEBI is more robust for one- or two-dimensional artificial material compositions like metamaterials and can work for both small and large attenuation scenarios. The driven method works robustly in the dispersion and attenuation analysis of periodic structures and can provide physical insight into the structure as well.

Searching the eigenvalues for the unit cell of periodic structures can be analogized to search the resonance frequencies in resonators. In resonators, one efficient way to find resonance frequencies is to stimulate the structure and make it resonance. In periodic structures by providing an excitation to the unit cell which is analogized to a resonator and monitoring the stimulated resonance can simplify the eigenvalue searching procedure to a maximization procedure, because the resonance is always accompanied with an extremum of the electromagnetic field observables, e.g. the electric field. The driven method starts with a vector estimation based on the previous solutions and repeats the iterations of solutions of excitation problems for slightly varying parameters. There are two possibilities to search the eigenvalues, which in the periodic structure are the pairs of (resonance frequency ω, wavevector $\boldsymbol{k}$). One is to fix the wavevector $\boldsymbol{k}$ and sweep the frequency ω till an extremum of the field observables is found. The other is to make ω constant and vary $\boldsymbol{k}$ to locate the extremum. When the structure is lossy or doubly periodic, $\boldsymbol{k}$ will be complex and a vector quantity. This will make the maximization a multi-dimensional searching procedure. Many optimization techniques are employed to achieve fast convergence in one or more dimensional searching. The implemented Brent's method provides the iteration of maximization in the driven method a parabolic convergence without calculating the divergence. The Powell's method is employed to perform the multi-dimension maximum searching efficiently. For the multi-mode operated one- or two-dimensional periodic structures, the global optimization has been introduced to search all the local maxima which are corresponding to the different modes in the operation frequency range.

2.4 Organization

In this work, after the introduction of periodic structures, like metamaterials and SIWs, a brief review of the periodic problem formulation will be given. According to the Floquet's theorem, the periodic structure can be modeled as one appropriately discretized unit cell with periodic boundary conditions. In chapter 4 the fundamentals of the numerical methods which are employed to analyze periodic structures, like the mode expansion method, and the scattering matrix method will be introduced. For open structures, which are the main focus of this work, absorbing layers will be introduced to enclose the analysis region for the mode expansion method to avoid the integral formulation for the radiation of open structures. Also the characteristics of the different methods will be compared. This work concentrates on the dispersion analysis of periodic structures. Therefore, the fundamentals of the modes and mode dispersion are introduced.

In chapter 5, the analogy between the eigenproblem and the resonator is discussed. This analogy opens up a possibility to convert the eigenproblem in the periodic structure to an excitation problem in the resonator model where the resonance frequencies are the eigenvalues. In the resonator, the resonance frequencies can be easily found by applying an excitation and monitoring the electromagnetic field observables which will reach an extremum at the resonance frequency. This procedure can not only provide insight into the modeling structure, but also analyze the dispersion and attenuation behavior of the periodic structures. Different excitation methods, e.g. port excitations and distributed current densities excitation are introduced. In section 5.1 the driven eigenproblem computation is realized with the commercial numerical solver CST Microwave Studio where the port excitations are employed. However, the limited boundary condition flexibility restrains its application to small attenuation scenarios where the perturbation method is employed to calculate the power loss for the guiding wave. Consequently the approach is unable to calculate the attenuation inside the stop band. Therefore, in section 5.2 the driven eigenproblem approach with distributed current densities excitation is implemented within the periodic hybrid finite-element boundary-integral (FEBI) method with the infinite periodic multilayer Green's function. With the distributed current densities excitation, one certain mode as well as all the relevant modes can be stimulated. The implementation in FEBI can directly support complex wavevectors within the periodic boundary conditions and the Green's function. Therefore, complex phase shifts on the periodic boundaries are possible which means the leaky and evanescent modes can be described and the attenuation inside the stop band can also be computed.

The eigenvalue, pairs of (frequency, wavevector) can fully characterize the properties of a microwave system, like waveguide, resonator and so on. In the resonator the eigenvalue is the resonance frequency where an extremum of the electromagnetic field inside the resonator will always take place. For a periodic structure, finding the resonance frequency in the equivalent resonator model which analogizes to the unit cell of the periodic structure can be transformed to a maximization problem of the electromagnetic field at a specified position inside the resonator over the complex wavevector and the frequency. Chapter 6 describes in detail the analogy between the eigenvalue searching and the maximization. Some acceleration methods, e.g. the Brent's and the Powell's method are introduced to accelerate the maximization in one- and multi-dimension. In order to find out all the extrema which stand for all the resonance modes, a global optimization need to be employed. The frequently used methods of global optimization are introduced.

In some frequency range, more than one resonance mode can be stimulated. Chapter 7 describes how to excite all modes or one specific mode by defining the current density excitations and how to distinguish different modes through comparing the electromagnetic field distribution. In chapter 8 several application examples of the driven method are given. A classical rectangular waveguide is analyzed by the driven method and compared to the analytical results stated in literature to verify the driven method. Then one SIW structure with uniform cross section in wave propagation direction is modeled in a unit cell with the driven method to demonstrate the performance of the driven method in the small attenuation scenario. The dispersion and attenuation behaviors obtained by the driven method match to the results from a longer model with the same unit cell configuration. An interdigital CRLH waveguide which is implemented by the SIW technology is also modeled in the unit cell with the driven method for the small attenuation scenario. Compared to other modeling methods like the scattering matrix approach, the driven method can generate more accurate results in dispersion and attenuation analysis. A grounded dielectric corrugated leaky wave antenna (LWA) with different width and in one-dimensional periodic configuration and a metamaterial based on the mushroom structure in two-dimensional periodic configuration are analyzed to demonstrate the versatility of the driven method with FEBI implementation. The acceleration methods are implemented to speed up the convergence of the maximization.

3 Metamaterials and SIWs

In recent researches, periodic structures like substrate integrated waveguides and metamaterials attract more and more attention with the properties of high-density integration possibility or negative refractive index. However, the large scale, the fine details and the often unclosed geometry of periodic structures make their modeling a complicated complex eigenproblem.

3.1 Metamaterials

3.1.1 Fundamentals of Metamaterials

Microwave metamaterials (MTMs) refer to a class of artificial materials that have simultaneously negative permittivity (ε) and permeability (μ) and sometimes they are named left-handed materials (LHMs). The theory of MTMs was firstly proposed by Victor Veselago in 1968 [Veselago, 1968]. The permittivity (ε) and permeability (μ) characterize the electric and magnetic properties of materials interacting with electromagnetic fields. The permittivity is the ability of the material to store electrical energy when an electric field is applied. It is defined as the ratio of the electric displacement vector of the medium $\boldsymbol{D}$ and the electric field $\boldsymbol{E}$, $\boldsymbol{D} = \varepsilon \boldsymbol{E}$. In the scientific work the relative permittivity ε_r, which is the ratio of the permittivity of the material to that of free space ($\varepsilon_0 = 8.858 \cdot 10^{-12}$ F/m), is commonly used. The permeability of a material indicates the relation between magnetic flux density vector $\boldsymbol{B}$ and the magnetic field vector $\boldsymbol{H}$, $\boldsymbol{B} = \mu \boldsymbol{H}$. Similar to ε_r, $\mu_r = \mu/\mu_0$, where $\mu_0 = 4\pi \cdot 10^{-7}$ Vs/(Am). Figure 3.1 categorizes the materials by ε and μ. Metamaterials were predicted to be characterized with

- necessary frequency dispersion of ε and μ,
- reversal of the Doppler effect,
- reversal of the Vavilov-Cerenkov radiation,
- reversal of the boundary conditions relating the normal components of the electric and magnetic fields at the interface between the conventional/right-handed (RH) medium and a LH medium,
- reversal of Snell's law,
- subsequent negative refraction at the interface between a RH medium and a LH medium,
- Plasmonic expressions of ε and μ in resonant-type LH media [Veselago, 1968].

However, this kind of materials with simultaneously negative ε and μ has not been found in nature until now.

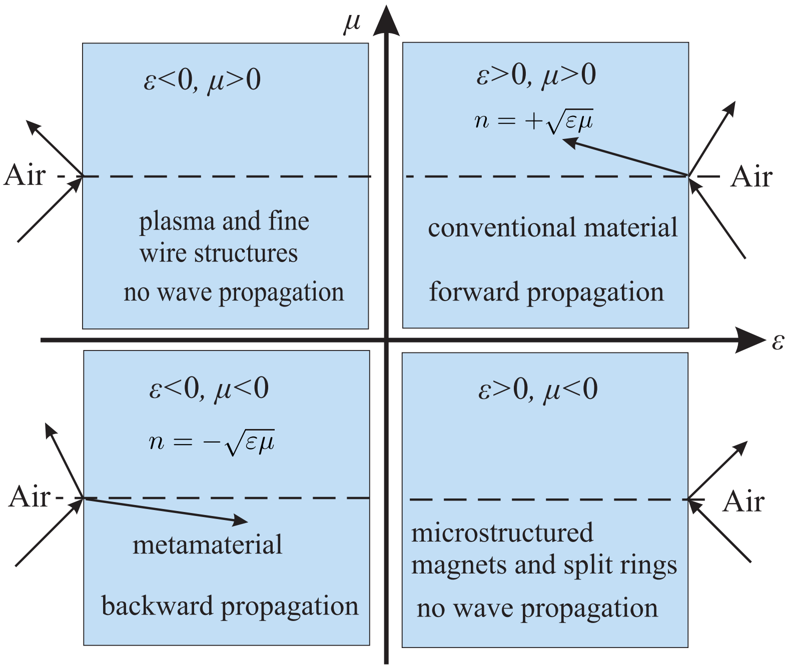

Figure 3.1: The diagram classifies materials in terms of their permittivity ε and permeability μ. The behavior of a wave incident on the air-material interface for each of the possible four cases is shown. The top right quadrant is a conventional dielectric material with positive ε and μ, which shows the refraction with the refraction angle smaller than the incident angle. The metamaterials in the bottom left quadrant with simultaneously negative ε and μ refract to the same side of the normal indicating reverse Snell's law. Plasmas with negative ε and positive μ and microstructured magnetic materials in the bottom right quadrant with positive ε and negative μ reflect the incident wave.

3.1.2 Modeling and Realization of Metamaterials

In 2000, the first demonstration of metamaterials was realized experimentally by Smith et al. [Smith et al., 2000]. The material was a combination of a thin-wire (TW) with negative-ε and positive-μ and a split-ring resonator (SRR) structure with positive-ε and negative-μ to have simultaneously negative ε and μ at certain frequencies. The average cell size p of the combination was much smaller than the guided wavelength λ_g ($p \ll \lambda_g$) which led to a quasi-homogeneous structure. Fig. 3.2 demonstrates the geometry of the first effectively homogeneous MTM.

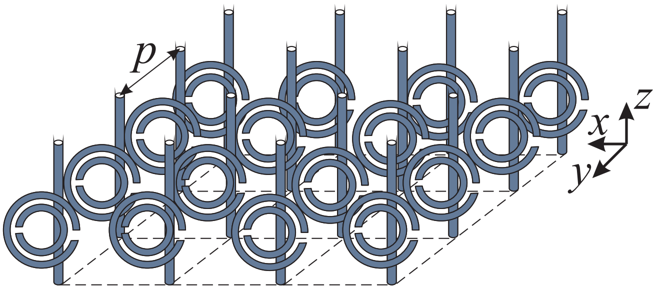

Figure 3.2: The first experimental demonstration of negative-ε/negativ-μ MTM, composed of split-ring resonators with thin wires placed uniformly between them.

Volumetric Metamaterials

The TW-SRR configuration is one of the synthesis methods of metamaterials, which is called a volumetric metamaterial or a bulk metamaterial. The SRR depicted in Fig. 3.2 can generate equivalent magnetic dipole moments when the excitation magnetic field $\boldsymbol{H}$ is perpendicular to the plane of the ring ($\boldsymbol{H} \parallel y$). Therefore, SRRs exhibit a plasmonic-type permeability frequency function of the form [Pendry et al., 1999]

$$\mu_r(\omega) = 1 - \frac{F\omega^2(\omega^2 - \omega_{0m}^2)}{(\omega^2 - \omega_{0m}^2)^2 + (\omega\zeta)^2} + j\frac{F\omega^2\zeta}{(\omega^2 - \omega_{0m}^2)^2 + (\omega\zeta)^2}, \tag{3.1.1}$$

where $F = \pi(a/p)^2$ and a is the inner radius of the small ring. $\omega_{0m} = c\sqrt{\frac{3p}{\pi\ln(2wa^3/\delta)}}$ is a magnetic resonance frequency with w as the width of the rings and δ is the radial spacing between the rings. Also $\zeta = 2pR'/(a\mu_0)$ is the damping factor due to metal losses with R' the metal resistance per unit length. In general, there can be a frequency range where $\mathbf{Re}(\mu_r) < 0$. For the lossless case where $\zeta = 0$,

$$\mu_r < 0, \quad \text{for} \quad \omega_{0m} < \omega < \frac{\omega_{0m}}{\sqrt{1-F}} = \omega_{pm}, \tag{3.1.2}$$

where ω_{pm} is called the magnetic plasma frequency. On the other hand, the TW in Fig. 3.2 can induce a current along it and it generates an equivalent electric dipole moment when the excitation electric field $\boldsymbol{E}$ is parallel to the axis of the wire ($\boldsymbol{E} \parallel z$). The resulting permittivity exhibits a plasmonic-type frequency function according to [Pendry et al., 1996, Pendry et al., 1998]

$$\varepsilon_r(\omega) = 1 - \frac{\omega_{pe}^2}{\omega^2 + \zeta^2} + j\frac{\zeta\omega_{pe}^2}{\omega(\omega^2 + \zeta^2)}, \tag{3.1.3}$$

where $\omega_{pe} = \sqrt{2\pi c^2/[p^2\ln(p/a)]}$ is the electric plasma frequency with c the light speed and a the radius of the wire. $\zeta = \varepsilon_0(p\omega_{pe}/a)^2/(\pi\sigma)$ is the damping factor due to the metal losses with σ the conductivity of the metal. Therefore,

$$\mathbf{Re}(\varepsilon_r) < 0, \quad \text{for} \quad \omega^2 < \omega_{pe}^2 - \zeta^2, \tag{3.1.4}$$

and for $\zeta = 0$,

$$\varepsilon_r < 0, \quad \omega < \omega_{pe}. \tag{3.1.5}$$

Combining TWs and SRRs with overlapping frequency ranges of negative permittivity and permeability into a composite TW-SRR as shown in Fig. 3.2, the structure can generate a substance in a frequency range with simultaneously negative permittivity and permeability. This kind of combination normally assembles randomly or periodically the basic elements with much smaller sizes compared to the operating wavelength to form a quasi-homogeneous metamaterial. But the volumetric MTMs have some intrinsic drawbacks. Due to the resonance characteristics of some elements, e.g. SRR, the volumetric MTMs are usually lossy and narrow-band and seem of little practical interest for the engineering applications.

Planar Metamaterials

An alternative architecture, called the planar MTM using the transmission line (TL) approach was almost simultaneously introduced by Eleftheriades et al. [IYER & Eleftheriades, 2002, Grbic & Eleftheriades, 2002], Oliner [Oliner, 2003] and Caloz et al. [Caloz & Itoh, 2002, Sanada et al., 2004]. These kinds of MTMs are based on conventional right-handed (RH) series-L and shunt-C TLs, shown in Fig. 3.3.

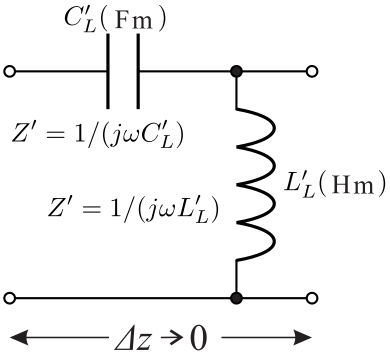

Figure 3.3: Incremental equivalent circuit model for hypothetical uniform LH TL.

In lossy systems the wavenumber k is complex and consists of the propagation constant k' and the attenuation constant k''. In lossless case the propagation constant k', the phase velocity v_p and the group velocity v_g of the TL can be expressed as

$$k = k' - jk'', \tag{3.1.6a}$$

$$k = k' = \sqrt{Z'Y'} = \frac{1}{j\omega\sqrt{L_L'C_L'}} = -j\frac{1}{\omega\sqrt{L_L'C_L'}}, \tag{3.1.6b}$$

$$k' = -\frac{1}{\omega\sqrt{L_L'C_L'}} < 0, \tag{3.1.6c}$$

$$v_p = \frac{\omega}{k'} = -\omega^2\sqrt{L_L'C_L'} < 0, \tag{3.1.6d}$$

$$v_g = (\frac{\partial k'}{\partial \omega})^{-1} = \omega^2\sqrt{L_L'C_L'} > 0. \tag{3.1.6e}$$

It is obvious that the phase velocity v_p associated with the direction of the phase propagation constant k' is negative and antiparallel to the group velocity v_g which indicates the power flow direction in the TL. This property makes the TL in Fig. 3.3 a LH material. The planar geometry of this realization architecture brings the advantages of the compatibility with microwave integrated circuits, the easy control of the behavior by L and C, low loss and broad bandwidth.

However, a purely LH structure does not exist, since the wave propagating in the circuit will induce a series inductance L_R and a shunt capacitor C_R to the series C_L and the shunt L_L, respectively. Therefore, a more accurate model for the MTM design came out. A number of circuits using LH TL are based on the composite right-/left-handed (CRLH) TL model introduced by Caloz and Itoh [Caloz & Itoh, 2003]. The CRLH MTMs, whose essential model is shown in Fig. 3.4, take the parasitic inductor L_R and capacitor C_R into account.

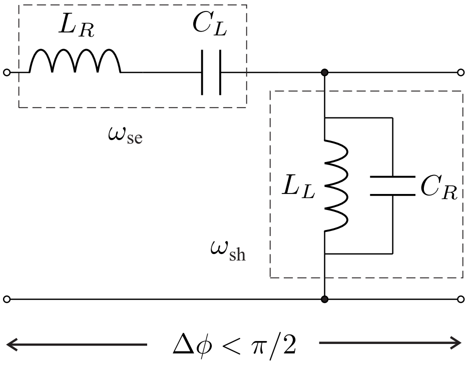

Figure 3.4: Equivalent circuit model for the composite right/left-handed (CRLH) MTMs.

At low frequencies, L_R and C_R tend to be short and open respectively, therefore the equivalent circuit will reduce to the series-C_L and shunt-L_L with *highpass* characteristics. The circuit shows the antiparallel phase and group velocities which indicates LH, as shown in Eq. (3.1.6a) to (3.1.6e), where k is the complex wavenumber, k' the propagation constant, v_p the phase velocity and v_g the group velocity. On the other hand, when the frequency goes high, short C_L and open L_L leave a series-L_R and shunt-C_R circuit with parallel phase and group velocities, which means RH and *lowpass* characteristics. When the series resonance frequency ω_{se} is not equal to the shunt resonance frequency ω_{sh}, there will be a bandgap between the LH and the RH range. However, the bandgap will disappear if these two resonance frequencies are made equal. An infinite-wavelength ($\lambda_g = 2\pi/|k'|$) propagation can be achieved at the transition frequency $\omega_{\mathrm{sh}} = \omega_{\mathrm{se}} = \omega_0$. Fig. 3.5 depicts the dispersion diagram for the balanced and the unbalanced CRLH TL according to the equivalent circuit depicted in Fig. 3.4, where $L_R = L_L$ and $C_R = C_L$ for the balanced case. Many devices have been developed based on the CRLH TL showing some advantages like bandwidth enhancement, dual-band operation, arbitrary coupling level as well as negative and zeroth-order resonance.

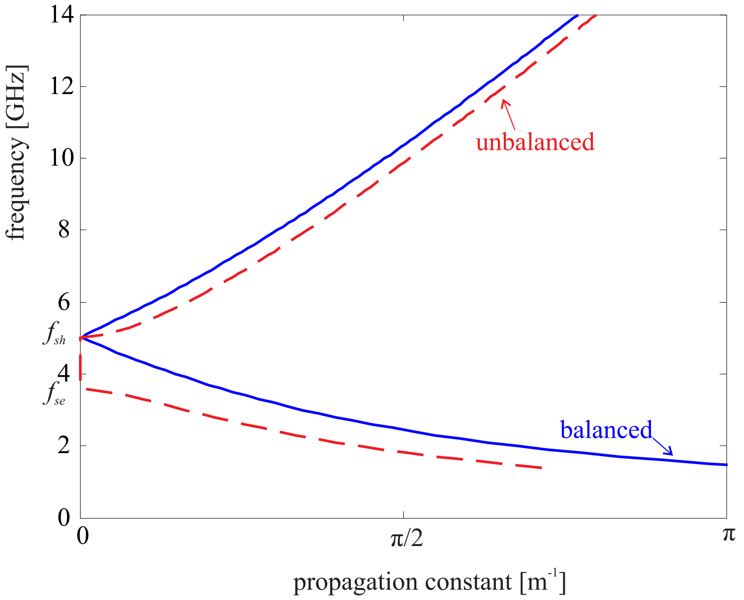

Figure 3.5: Balanced and unbalanced CRLH MTMs.

1D and 2D Planar Metamaterials

The TL theory is wildly used to realize one-dimensional (1D) MTMs, which are effectively homogeneous structures and can be essentially modeled by 1D transmission lines. In this kind of MTMs, the wave propagates in one dimension which can be any direction in the material. The TL theory can be extended to two-dimensional structures, often named metasurfaces, where a discrete TL unit cell is defined to form a network [Caloz & Itoh, 2006, Sievenpiper et al., 1999]. Fig. 3.6 presents some examples for 1D and 2D MTMs respectively.

Due to the multi-dimensional wave propagation in 2D MTMs, e.g. in x- and y-direction

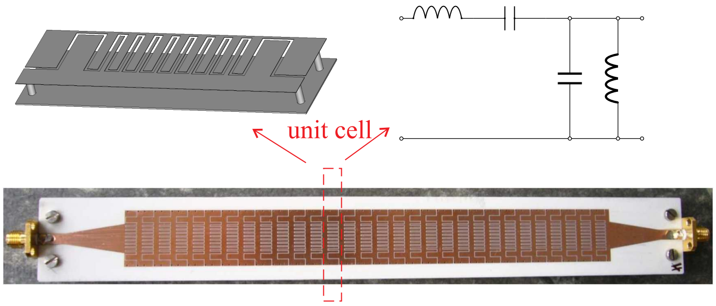

(a) 1D MTM in interdigital configuration and its equivalent circuit [Weitsch & Eibert, 2010].

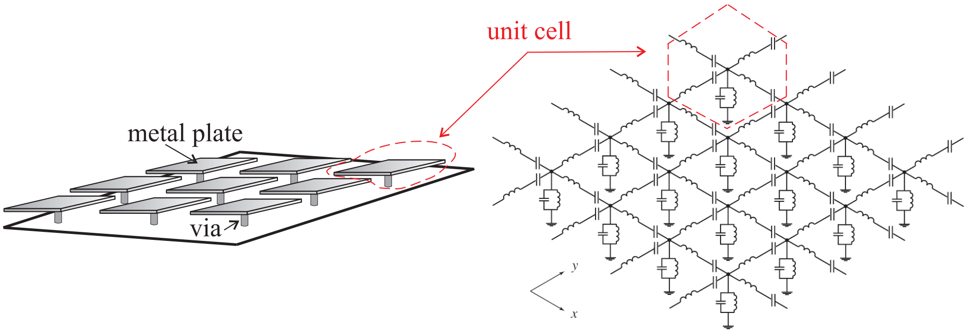

(b) 2D MTM in mushroom structure and its equivalent circuit [Sievenpiper et al. 1999].

Figure 3.6: Examples of 1D and 2D MTMs. (a) is a 1D MTM in interdigital configuration for leaky wave antenna and its equivalent circuit [Weitsch & Eibert, 2010]. (b) is a 2D MTM in mushroom structure and its equivalent circuit [Sievenpiper et al., 1999].

as shown in Fig. 3.6(b), the dispersion relation is a 2D function $\omega_n(k_x, k_y)$, where n labels the number of the mode. In [Caloz & Itoh, 2006] the *Brillouin zone* and *irreducible Brillouin zone* are introduced to demonstrate the dispersion curve for 2D MTMs, whose details can be found in section 4.5.

3.2 Substrate Integrated Waveguide (SIW)

Microstrip is one of the most widely used planar technologies in microwave engineering because its easy fabrication and ability to integrate with other passive and active microwave devices. On a microstrip line the fundamental wave propagates as "quasi-TEM" which means most of the field concentrates between the strip conductor and the ground plane whereas some fraction of the field exists in the air region above the substrate. In high frequency applications like millimeter-wave range, microstrip lines will suffer from high losses due to the thin configuration and the manufacturing tight tolerances. On the contrary, high frequency hollow waveguides which have better power capacity are quite difficult to fabricate and are not compatible with planar structures. Therefore, the substrate integrated waveguide (SIW) which realizes a dielectric-filled waveguide in a planar geometry emerged to solve this dilemma. SIW is fabricated by using two periodic rows of metallic vias or slots connecting the top and the bottom metal planes of a printed circuit board (PCB) with a dielectric substrate in between as shown in Fig. 3.7. The geometry of SIW is suitable for mass production, low-cost fabrication and high density integration. SIW is one of the promising solutions for millimeter-wave applications which is now already applied in wireless networks, automotive radars and imaging sensors with a frequency range of 60 – 94 GHz [Bozzi et al., 2009].

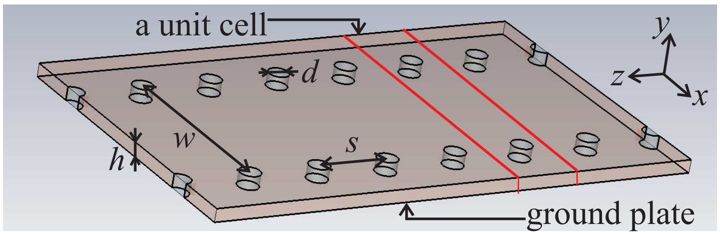

Figure 3.7: The structure of a substrate integrated waveguide by using the metallic via-hole arrays.

3.2.1 Characteristics of SIWs

SIWs show similar characteristics as traditional rectangular waveguides. An SIW with a width of w has the same propagation constant as a rectangular waveguide with a width of w_{equ}. Here w is the center-to-center distance between parallel sets of vias in the SIW and w_{equ} is the width of the broad wall of the equivalent rectangular waveguide . In the circuit design, people can calculate the equivalent width w_{equ} as [Cassivi et al., 2002]

$$w_{\mathrm{equ}} = w - \frac{d^2}{0.95s}, \tag{3.2.1}$$

where s is the distance between the adjacent vias, and d the diameter of the via, as shown in Fig. 3.7. The cutoff frequency f_c for the TE_{10} mode of the SIW can be expressed as

$$f_c = \frac{c}{2\sqrt{\varepsilon_r}}(w - \frac{d^2}{0.95s}). \tag{3.2.2}$$

This approximation can reach ±5% accuracy in f_c when $s < \lambda_0\sqrt{\varepsilon_r}/2$ and $s < 4d$ where λ_0 is the free-space wavelength and ε_r is the relative dielectric constant of the substrate of the SIW.

3.2.2 Different Types of SIWs

Besides the geometry depicted in Fig. 3.7, there are several different types of SIW. Some of them can reduce the size without changing the field distribution. Some of them can increase the bandwidth by reducing the cutoff frequency of the fundamental mode.

- Half-mode SIW (HMSIW)
  The half-mode SIW depicted in Fig. 3.8 was first proposed in 2005 by W. Hong and K. Wu [Hong et al., 2006]. The HMSIW cuts half of the SIW along the symmetric plane in the transmission direction which can be equalized to a magnetic wall (MW) and the half field distribution keeps unchanged in the HMSIW compared to the SIW. Therefore the size of SIW can be reduced to half.

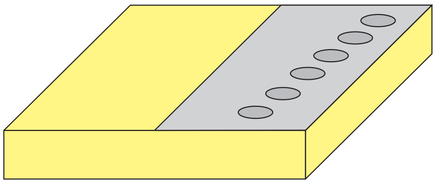

(a) The geometrical configuration of HMSIW

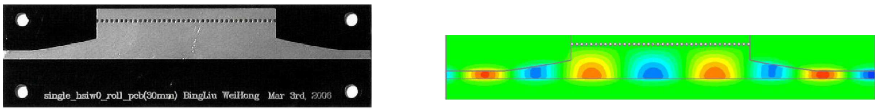

(b) One example of HMSIW with microstrip line transition [Hong et al., 2006]

(c) Domain field distribution in HMSIW [Hong et al., 2006]

Figure 3.8: The structure of a half-mode SIW and the field distribution [Hong et al., 2006]. (a) The geometrical configuration of a HMSIW. (b) One demonstration of HMSIW with transition to microstrip line [Hong et al., 2006]. (c) Domain field distribution in HMSIW [Hong et al., 2006].

- Folded SIW (FSIW)
  The folded SIW shown in Fig. 3.9 realizes the folded rectangular waveguide which is transversely folded to form a compact structure but maintains the same propagation characteristics of the conventional rectangular waveguides [Chen et al., 1988]. [Grigoropoulos et al., 2005] proposed a type of FSIW by using double-layer substrate which can reduce the waveguide width up to $(9\varepsilon_r)^{-1/2}$ and overcome the difficulties of manufacturing the internal vias forming the central T-septum by laminates and low temperature co-fired ceramic (LTCC) [Grigoropoulos & Young, 2004].

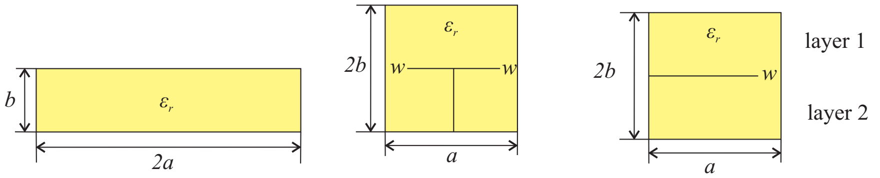

(a) rectangular waveguide (b) equivalent folded waveguide (c) cross section of folded SIW in (e)

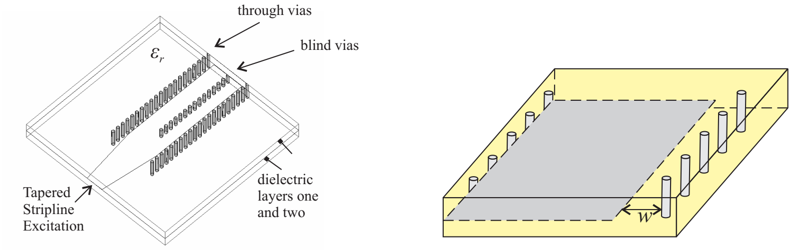

(d) folded SIW with T-septum in [Grigoropoulos & Young, 2004] (e) folded SIW in [Grigoropoulos et al., 2005]

Figure 3.9: The structure of FSIW. (a) The cross section of a conventional rectangular waveguide. (b) The cross section of an equivalent folded waveguide. (c) The cross section of an FSIW [Grigoropoulos et al., 2005]. (d) One example of FSIW with T-septum [Grigoropoulos & Young, 2004]. (e) One example of FSIW without T-septum [Grigoropoulos et al., 2005].

- Ridged SIW (RSIW)
  The ridged SIW shown in Fig. 3.10 evolves from a ridged rectangular waveguide [Hopfer, 1955]. It can reduce the cutoff frequency of the fundamental mode like TE_{10} mode so that the bandwidth is increased [Bao et al., 2012]. The RSIW is wildly used in WLAN antenna [Luan & Tan, 2011] and ultra-wideband [Luan & Tan, 2012] applications.

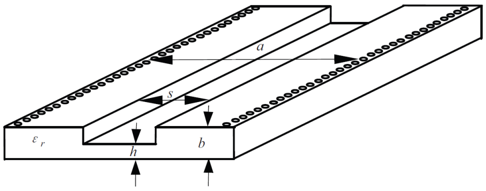

Figure 3.10: The structure of RSIW [Bao et al., 2012].

3.2.3 Existing Modeling Methods for SIWs

Similar to rectangular waveguides, SIWs have a high quality factor and high power-handling capability compared to other planar structures like microstrip lines. But the periodic bilateral gaps between the vias make SIWs subject to inherent leakage losses, which makes their dispersion and attenuation modeling a complicated complex eigenproblem. In former researches, the model and design of SIWs are often based on full-wave analysis tools. The numerical methods like the Finite-Difference Time Domain method (FDTD), the Boundary Integral-Resonant Mode Expansion method (BI-RME), the Finite-Difference Frequency Domain method (FDFD), or the Method of Moments (MoM)-based analysis schemes like Transverse Resonance Method have all been employed to the solve the eigenproblem of SIWs. Each method has its own advantages and disadvantages.

- **The Finite Difference Frequency Domain Method (FDFD)**
  The conventional FDFD usually relates the roots of the eigenproblem to the frequencies of a given value of the propagation constant. This makes the method not a good choice for the periodic structure which usually has complex propagation constants. In [Xu et al., 2003] the conventional FDFD is combined with Floquet's theorem and perfectly matched layer (PML) absorbing boundary condition (ABC) to transfer the difficult complex root-extracting problem of a transcend equation into a generalized matrix eigenvalue problem. The Floquet's theorem for the periodic structure restricts the computational layer to a single period. On the other hand, the use of a PML ABC can eliminate the longitudinal field components and yield an eigenproblem with its eigenvalue as the corresponding propagation constant. In the loss analysis, [Xu et al., 2003] equals the structure under analysis to the resonant cavity so that the transmission distance-related attenuation constant is translated into a time-dependent damping factor.

- **The Boundary Integral-Resonant Mode Expansion Method (BI-RME)**
  The BI-RME method provides the admittance matrix of the structure in the form of a pole expansion in the frequency domain, relating the modal currents and voltages at the terminal waveguide sections. It allows to derive directly the equivalent circuit layout and find the value of its components and avoids any initial guess or fitting procedure. One characteristic limitation of BI-RME is that the method can only be applied to completely shielded structures. Therefore, in structures like SIWs which are not closed, fictitious metal walls need to be added outside the structures in order to make them close. When the radiation leakage is negligible the fictitious metal walls will not effect the propagation characteristics of SIWs [Bozzi et al., 2006].

- **The Finite Difference Time Domain Method (FDTD)**
  The FDTD method transfers the modeling of a periodic guided-wave structure to the modeling of an equivalent resonant cavity. The equivalent resonant cavity is formed by terminating a single unit cell with the periodic boundary condition in the propagation direction. The eigenfrequency extracted by the FDTD method

for resonators yields the desired solution in terms of frequency and quality factor. The attenuation constant can then be obtained from the extracted quality factor [Xu et al., 2007].

- **The Domain Decomposition Method**
  The domain decomposition method combines the "domain decomposition FDTD" and the numerical thru-line (TL) calibration technique to develop an accurate and more efficient parameter extraction of microwave circuits and structures. Using the numerical TL calibration method, the structure under analysis can be effectively divided into two separate parts: error boxes and a circuit box. The error box represents the potential error terms related to the port/transition discontinuities, while the circuit box characterizes the realistic or designed circuit properties. Instead of using the short-/open-circuit calibrations which are difficult to realize, the usage of the numerical thru-line (TL) calibration procedure can greatly remove the potential errors and the parasitic terms which are brought from the excitation model, the numerical dispersion and the inherent effects of simulated structures. Especially in FDTD method, the TL calibration technology can move the position of parameter extraction into virtual normal waveguides to overcome the challenge of the separation between the source and reflection excitation in time domain [Xu et al., 2006].

- **The Transverse Resonance Method**
  The transverse resonance method makes use of the concept of the surface impedance to model the rows of the conducting cylinders and the proposed model is then solved by combining the method of moments and the transverse resonance procedure. In this method the rows of cylinders in SIWs are represented as the surface impedance, which can be calculated from the reflection coefficient. The equivalent width of the SIW can be written as a function of the surface impedance. The complex propagation constant can also be expressed as a function of the surface impedance, the equivalent width of the SIW and the frequency. Therefore, the problem of finding the propagation constant is equivalent to a problem of finding the reflection coefficient at a desired cutoff frequency. The reflection coefficient can be solved with the method of moments (MoM) technique, by discretizing the current on the cylinder surface into N current filaments along the axis of the cylinder. By using the Green's function for a current filament in a TEM waveguide, a moment solution for the electromagnetic scattering by a single inductive post in a rectangular waveguide can be calculated. After calculating the current at N points on the surface of the cylinder, the reflection coefficient in the plane of the cylinder can be found [Deslandes & Wu, 2006].

3.2.4 Limitations of Existing Methods

- The methods based on the classical eigenvalue solvers, like BI-RME, or FDFD, MoM, have difficulties to calculate accurately the attenuation constant due to the leakage of the SIW. Even through the calibration techniques, the methods are still slow for the design purpose, as they require full-wave simulations for two guiding structures of different lengths.

- The MoM-based method and the Floquet-Bloch theorem require the summation of the electric fields generated by the currents on the cylinders. These fields are represented by a set of Hankel functions, which usually lead to a very slow convergence during the summation. The convergence becomes even slower when the semi-unbounded waveguide, like SIW, presenting high leaky-wave losses, leads to an ineffective calculation of the propagation constant, whose accuracy can also be severely lowered.

4 Modeling of Periodic Configurations

4.1 Eigenproblem Formulation for Electromagnetic Fields

Maxwell's equations are a set of fundamental equations that govern all macroscopic electromagnetic phenomena. The analysis of electromagnetic fields is actually a problem solving a set of Maxwell's equations subject to given boundary conditions [Jin, 2002]. Maxwell's equations can be considered as eigenproblems, whose eigenvalues and eigensolutions sufficiently characterize the electromagnetic systems under analysis.

4.1.1 Maxwell's Equations

Maxwell's Equations are a set of fundamental differential equations indicating the behavior of electromagnetic fields which were originally expressed by Maxwell in some 20 equations in 1865 [Maxwell, 1873] and later refined by Heaviside to the four equation forms [Heaviside, 1888]:

$$\nabla \times \boldsymbol{E} = -\mu \frac{\partial \boldsymbol{H}}{\partial t}, \tag{4.1.1}$$

$$\nabla \times \boldsymbol{H} = \varepsilon \frac{\partial \boldsymbol{E}}{\partial t} + \boldsymbol{J}, \tag{4.1.2}$$

$$\nabla \cdot \varepsilon \boldsymbol{E} = \rho, \tag{4.1.3}$$

$$\nabla \cdot \mu \boldsymbol{H} = 0, \tag{4.1.4}$$

and

$$\nabla \cdot \boldsymbol{J} = -\frac{\partial \rho}{\partial t}, \tag{4.1.5}$$

where

$$\begin{aligned} \boldsymbol{E} &= \text{electric field} \quad (\text{V/m}), \\ \boldsymbol{H} &= \text{magnetic field} \quad (\text{A/m}), \\ \rho &= \text{free electric charge density} \quad (\text{C/m}^3), \\ \boldsymbol{J} &= \text{free current density} \quad (\text{A/m}^2), \\ \varepsilon &= \text{permittivity of the medium} \quad (\text{F/m}), \\ \mu &= \text{permeability of the medium} \quad (\text{H/m}). \end{aligned} \tag{4.1.6}$$

When the field is time harmonic, the spatial and time varying fields $\boldsymbol{E}$ and $\boldsymbol{H}$ can be expressed in the form

$$\boldsymbol{E}(\boldsymbol{r},t)=\boldsymbol{E}(\boldsymbol{r})e^{j\omega t} \quad \text{and} \quad \boldsymbol{H}(\boldsymbol{r},t)=\boldsymbol{H}(\boldsymbol{r})e^{j\omega t}, \tag{4.1.7}$$

which transfer the Maxwell's equations (4.1.1) to (4.1.3) as

$$\nabla\times\boldsymbol{E}=-j\omega\mu\boldsymbol{H}, \tag{4.1.8}$$
$$\nabla\times\boldsymbol{H}=j\omega\varepsilon\boldsymbol{E}+\boldsymbol{J}, \tag{4.1.9}$$
$$\nabla\cdot\varepsilon\boldsymbol{J}=-j\omega\rho. \tag{4.1.10}$$

Eq. (4.1.8) to (4.1.10) can form a set of first-order partial differential equations. With appropriate initial conditions which define the field quantities impressed in a given volume at an initial time, the boundary conditions which define at any instant of time the field quantities impressed upon the surface enclosing the given volume, and also the Sommerfeld radiation condition [Jin, 2002, Bérenger, 1994, Sommerfeld, 1949]

$$\lim_{r\to\infty} r[\nabla\times\begin{pmatrix}\boldsymbol{E}\\ \boldsymbol{H}\end{pmatrix}+jk_0\hat{r}\times\begin{pmatrix}\boldsymbol{E}\\ \boldsymbol{H}\end{pmatrix}]=0, \tag{4.1.11}$$

some unique solution to the set of partial differential equation formed by Maxwell's equations can be obtained.

In Eq. (4.1.11) $r=|\boldsymbol{r}|$ and $\hat{r}=\boldsymbol{r}/r$ stand for the magnitude and the direction of the position vector $\boldsymbol{r}$ respectively. k_0 is the free space wavenumber. The Sommerfeld radiation condition enforces the solution corresponding to the fields radiating from the sources to infinity. Unphysical solutions, like corresponding to sinking in sources or energy coming from infinity, are omitted.

4.1.2 Helmholtz' Equations

For the time-harmonic field, Maxwell's equations can be rewritten for both electric and magnetic fields:

$$\nabla\times(\frac{1}{\mu}\nabla\times\boldsymbol{E})+\omega^2\varepsilon\boldsymbol{E}=-j\omega\boldsymbol{J}, \tag{4.1.12}$$
$$\nabla\times(\frac{1}{\varepsilon}\times\boldsymbol{H})+\omega^2\mu\boldsymbol{H}=\nabla\times(\frac{1}{\varepsilon}\boldsymbol{J}). \tag{4.1.13}$$

These equations are called inhomogeneous vector wave equations. For homogeneous material and source-free systems, the left side of Eq. (4.1.12) and (4.1.13) can be rewritten as the Helmholtz equations

$$\nabla^2\boldsymbol{E}+k^2\boldsymbol{E}=0, \tag{4.1.14}$$
$$\nabla^2\boldsymbol{H}+k^2\boldsymbol{H}=0, \tag{4.1.15}$$

where $k=\omega\sqrt{\varepsilon\mu}$ is the wavenumber of the medium with the dimension of 1/m.

4.1.3 Floquet's Theorem

A periodic problem is the problem of wave propagation in a periodic structure, which may be characterized by periodic boundary conditions or a periodically varied dielectric constant [Ishimaru, 1991]. According to Floquet's theorem, in an infinite periodic structure which is periodic in the direction of y-axis, the fields at a point y differ from the fields one period of p away by a constant attenuation and a phase shift according to

$$u(y+mp) = C^m u(y). \tag{4.1.16}$$

Here $u(y)$ and $u(y+mp)$ are the wave at the point y and $y+mp$, respectively. m is an integer number. The constant C is in general a complex quantity, which can be expressed as

$$C = e^{-jkp}, \qquad\qquad k = k' - jk'', \tag{4.1.17}$$

and k represents the wavenumber, where k' is the propagation constant and k'' is the attenuation constant. Floquet's theorem gives the possibility to represent the entire periodic structure as one unit cell with periodic boundary considered according to

$$\left\{ \begin{array}{c} \boldsymbol{E}(y) \\ \boldsymbol{H}(y) \end{array} \right\} = \left\{ \begin{array}{c} \boldsymbol{E}_p(y) \\ \boldsymbol{H}_p(y) \end{array} \right\} e^{-jkp}, \qquad \left\{ \begin{array}{c} \boldsymbol{E}_p(y) \\ \boldsymbol{H}_p(y) \end{array} \right\} = \left\{ \begin{array}{c} \boldsymbol{E}(y+p) \\ \boldsymbol{H}(y+p) \end{array} \right\}. \tag{4.1.18}$$

When the structure is periodic in two or even three dimension, e.g. metasurfaces, the scalar wavenumber k is replaced by a vector quantity $\boldsymbol{k}$, called wavevector, which defines the non-periodic functional dependence in space,

$$\left\{ \begin{array}{c} \boldsymbol{E}(\boldsymbol{r}) \\ \boldsymbol{H}(\boldsymbol{r}) \end{array} \right\} = \left\{ \begin{array}{c} \boldsymbol{E}_p(\boldsymbol{r}) \\ \boldsymbol{H}_p(\boldsymbol{r}) \end{array} \right\} e^{-j\boldsymbol{k}\cdot\boldsymbol{r}}, \tag{4.1.19}$$

where $\boldsymbol{r}$ contains the spatial periodic information with $\boldsymbol{r} = mp_x\hat{x} + np_y\hat{y} + kp_z\hat{z}$. p_x, p_y, and p_z represent the length of one unit cell in x-, y- and z-axis, respectively. $\boldsymbol{k}$ can be written for 3D periodic configurations as

$$\boldsymbol{k} = k_x\hat{x} + k_y\hat{y} + k_z\hat{z}. \tag{4.1.20}$$

4.1.4 Eigenmodes and Eigenvalues

Eq. (4.1.12) and (4.1.13) can be considered as an operator equation according to

$$L(\omega, \boldsymbol{k})\phi = f, \tag{4.1.21}$$

where f is the excitation or forcing function, and ϕ is the unknown quantity which can be the electric or magnetic field. $L\cdot$ represents some form of Maxwell's equations with appropriate boundary conditions and material relations and $\boldsymbol{k}$ indicates the wavevector. This kind of field problem is called boundary-value problem. In electromagnetics, field problems are usually associated with source-free scenarios like wave propagation in waveguides or the resonances in cavities, which means f vanishes and Eq. (4.1.14) and (4.1.15) are represented as

$$L(\omega, \boldsymbol{k})\phi = 0. \tag{4.1.22}$$

Eq. (4.1.22) is called eigenvalue problem where both governing differential equations and boundary conditions are homogenous. Instead of finding ϕ for a non-zero f, the eigenvalue pair $(\omega, \boldsymbol{k})$ is solved in an eigenvalue problem. Consequently, the corresponding ϕ is the eigensolution. Eigenmodes (EMs) and eigenvalues (EVs) can uniquely determine the characteristics of a system, like a waveguide, a resonator, or a periodic structure. In numerical solvers based on finite element (FE), finite difference (FD), or moments methods, the operator equation is typically discretized and leads to a linear homogeneous equation system

$$[A_{mn}(\omega, \boldsymbol{k})]\{\phi_n\} = 0. \tag{4.1.23}$$

A_{mn} are the matrix entries as a function of $(\omega, \boldsymbol{k})$ and ϕ_n are the unknown expansion coefficients of the field solution. The eigenvalues here are pairs of $(\omega, \boldsymbol{k})$, which make the system singular and indicate one or more propagating modes. A collection of pairs of $(\omega, \boldsymbol{k})$ covering a range of frequencies can form the dispersion behavior of the system under analysis. However, for large numerical systems, the solution of the eigenproblems is often much more demanding than the solution of the corresponding driven problems and the convergence behavior is often not satisfying. Especially periodic configurations, like metamaterials, may often lead to eigenproblems with a considerable number of unknowns. In periodic configurations the boundary conditions can be periodic in one, two or three dimensions which can also be combined with other boundary conditions like perfect electric conductor (PEC), perfect magnetic conductor (PMC) or absorbing boundary condition (ABC).

4.2 Modal Series Expansion Method

One frequently used numerical method for periodic structures is a modal series expansion. Modal series expansion expresses the eigensolution of the inhomogeneous periodic structure under analysis in a series expansion with the eigensolution of the homogeneous background waveguide as the basis functions to reduce the number of unknowns. As we know, a waveguide is typically operated in the fundamental mode and only a finite number of modes are relevant in the frequency range of interest. Moreover, the orthonormality and completeness of the modes make it possible to obtain the eigensolution accurately with the expansion of just a few modes, e.g. the propagating and some evanescent modes. For many background waveguides like rectangular waveguides, and cylindrical waveguides, the eigensolutions can be obtained analytically. For complicated background structures, the eigensolutions can be computed numerically by solving eigenproblems, e.g. with CST MWS [CST, 2011]. A periodic configuration according to Floquet's theorem, can be modeled in one unit cell with periodic boundaries. Positioning the periodic boundaries in the undistorted regions of the background waveguide, identical to the cross section of the waveguide and perpendicular to the wave propagation direction as depicted in Fig. 4.1, e.g. the y-direction, makes it possible to formulate the fields depending on x, z on the input periodic boundary according to

$$\boldsymbol{E}_{port,in}(x,z) = \sum_{m=1}^{M} [a_m \boldsymbol{e}_{m,port}(x,z) + b_m \boldsymbol{e}_{m,port}(x,z)], \tag{4.2.1}$$

$$\boldsymbol{H}_{port,in}(x,z) = \sum_{m=1}^{M} [a_m \boldsymbol{h}_{m,port}(x,z) - b_m \boldsymbol{h}_{m,port}(x,z)], \tag{4.2.2}$$

where the eigensolutions $\boldsymbol{e}_{m,port}$ and $\boldsymbol{h}_{m,port}$ for the electric and the magnetic fields of the background waveguide, respectively, work as basis functions. The wave coefficients a_m indicate the inward waves while b_m refer to the outward waves. For the magnetic field, the term with the outward wave coefficient $\boldsymbol{h}_{m,port}$ is to subtract in order to maintain an orientation in the right-hand sense. In the port planes, which are identical to the background waveguide cross section, the feeding modes with a number of M can be applied to excite the structure. Every mode can excite the unit cell and couple to all other modes. Inserting the modal expansion, Eq. (4.2.1) and (4.2.2) into Floquet's theorem expressed as Eq. (4.1.18), the field solution at the output port can be expressed as

$$\boldsymbol{E}_{port,out}(x,z) = \boldsymbol{E}_{port,in}(x,z) e^{-jkp}, \tag{4.2.3}$$

$$\boldsymbol{H}_{port,out}(x,z) = \boldsymbol{H}_{port,in}(x,z) e^{-jkp}, \tag{4.2.4}$$

and

$$\boldsymbol{E}_{port,out}(x,z) = \sum_{m=1}^{M} [b'_m \boldsymbol{e}_{m,port}(x,z) + a'_m \boldsymbol{e}_{m,port}(x,z)], \tag{4.2.5}$$

$$\boldsymbol{H}_{port,out}(x,z) = \sum_{m=1}^{M} [b'_m \boldsymbol{h}_{m,port}(x,z) - a'_m \boldsymbol{h}_{m,port}(x,z)], \tag{4.2.6}$$

where L is the length of the periodic unit cell, and the complex wave number $k = k' - jk''$, k' is the propagation constant and k'' the attenuation constant. The outgoing primed modes b'_m are related to the incident modes a_m and the ingoing primed modes a'_m to the outgoing modes b_m according to

$$a_m = b'_m e^{jkp}, \tag{4.2.7}$$

$$b_m = a'_m e^{jkp}. \tag{4.2.8}$$

Transfer Matrix Representation and Scattering Matrix Approach

If we consider the k-th unit cell of one periodic configuration shown in Fig. 4.2, the relationship between the amplitude of the modes at the input port and the ones at the

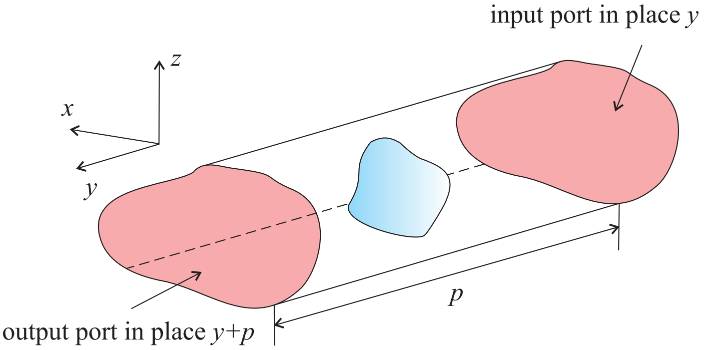

Figure 4.1: Unit cell of an inhomogeneous periodic structure modeled in the background waveguide with periodic boundaries.

output port can be expressed as

$$\begin{pmatrix} b_1 \\ \vdots \\ b_M \\ a_1 \\ \vdots \\ a_M \end{pmatrix} = \begin{pmatrix} T_{11}^{11} & \cdots & T_{11}^{1M} & T_{12}^{11} & \cdots & T_{12}^{1M} \\ \vdots & \ddots & \vdots & \vdots & \ddots & \vdots \\ T_{11}^{M1} & \cdots & T_{11}^{MM} & T_{12}^{M1} & \cdots & T_{12}^{MM} \\ T_{21}^{11} & \cdots & T_{21}^{1M} & T_{22}^{11} & \cdots & T_{22}^{1M} \\ \vdots & \ddots & \vdots & \vdots & \ddots & \vdots \\ T_{21}^{M1} & \cdots & T_{21}^{MM} & T_{22}^{M1} & \cdots & T_{22}^{MM} \end{pmatrix} \begin{pmatrix} a'_1 \\ \vdots \\ a'_M \\ b'_1 \\ \vdots \\ b'_M \end{pmatrix}. \tag{4.2.9}$$

On the left side of the Eq. (4.2.9), there are the complex wave amplitudes of the modes in the input port plane, while the ones in the output port plane are grouped in the vector $\boldsymbol{v} = (a'_1, \cdots, a'_M, \cdots, b'_1, \cdots, b'_M)$. The transfer matrix $\boldsymbol{T}$ connects the incident and the reflected waves at the input port to the ones at the output port. If M modes are observed at each port, the $\boldsymbol{T}$-matrix has a dimension of $2M \times 2M$. The superscript of the $\boldsymbol{T}$-parameters T_{ij}^{nm} indicates the coupling contribution from mode m at the output port to the mode n at the input port. The subscript indicates the coupling type. In a periodic configuration the outward wave b' at the output port of the k-th unit cell is the inward wave a at the input port of the $(k+1)$-th unit cell which makes the $\boldsymbol{T}$-matrix a perfect modeling method for periodic configurations. The complete behavior $\boldsymbol{T}_{\text{total}}$ of the total periodic configuration consisting of K unit cells can be expressed as a multiplication of $\boldsymbol{T}_k$ as

$$\boldsymbol{T}_{\text{total}} = \prod_{k=1}^{K} \boldsymbol{T}_k, \tag{4.2.10}$$

where the order of the multiplication must not be changed.

Take Eq. (4.2.7) and (4.2.8) into Eq. (4.2.9) then the equation can be rewritten as

$$e^{jkp}\boldsymbol{v} = \boldsymbol{T}_k\boldsymbol{v} \quad \text{or} \quad (\boldsymbol{T}_k - e^{jkp}\boldsymbol{I})\boldsymbol{v} = 0, \tag{4.2.11}$$

where $\boldsymbol{v} = (a'_1, \cdots, a'_M, \cdots, b'_1, \cdots, b'_M)$, and $\boldsymbol{I}$ is the identity matrix. Eq. (4.2.11) is in the form of an eigenproblem, where e^{jkp} is the eigenvalue. With the determined eigenvalue, the propagation and the attenuation constant can be obtained as

$$k' = -\angle(e^{-jkp})/p, \tag{4.2.12}$$

$$k'' = \ln(|e^{-jkp}|)/p, \tag{4.2.13}$$

depending on frequency giving directly the dispersion and attenuation behavior of the periodic configuration.

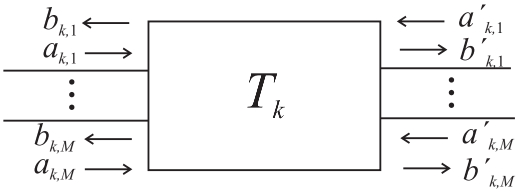

Figure 4.2: The T-matrix connects the modes on the input port to the ones in the outport of the k-th unit cell.

However, the $\boldsymbol{T}$-matrix is not directly accessible. Instead the scattering matrix which defines the relation of incident and reflected waves at one port or from one port to the other, can be directly obtained through some numerical full wave solvers like CST [CST, 2011] based on

$$S_{ij} = \frac{b_i}{a_j}|_{a_k=0 \text{ for } k\neq j}. \tag{4.2.14}$$

In Eq. (4.2.14), S_{ij} is found by driving port j by the incident wave a_j and measuring the reflected wave b_i at port i where all the other ports are terminated with a matched load. Therefore, S_{ii} is the reflection coefficient of port i when the incident waves at other ports are set zero and S_{ij} is the transmission coefficient from port j to port i.

In some scenarios, more than one mode will be considered at each port. If in a N-port network, as shown in Fig. 4.2, where $N = 2$, M modes are activated in each port, the S-matrix can be written as

$$\begin{pmatrix} b_1 \\ \vdots \\ b_M \\ b'_1 \\ \vdots \\ b'_M \end{pmatrix} = \begin{pmatrix} \boldsymbol{S}_{11} & \boldsymbol{S}_{12} \\ \boldsymbol{S}_{21} & \boldsymbol{S}_{22} \end{pmatrix} \begin{pmatrix} a_1 \\ \vdots \\ a_M \\ a'_1 \\ \vdots \\ a'_M \end{pmatrix}, \tag{4.2.15}$$

$$\text{where } \boldsymbol{S}_{ij} = \begin{pmatrix} S_{ij}^{11} & \cdots & S_{ij}^{1M} \\ \vdots & \ddots & \vdots \\ S_{ij}^{M1} & \cdots & S_{ij}^{MM} \end{pmatrix}, \quad i, j = 1, 2. \tag{4.2.16}$$

Here the superscripts of the matrix elements indicate the modes and the subscripts indicate the ports. S_{ii}^{nn} is the reflection coefficient of mode n at port i, and S_{ij}^{nm} indicates the transmission coefficient of mode m at the port j to mode n at the port i, when the other inward modes are all set zero, as $a_k = 0,\ k \neq m$. The S-parameters present the cross-coupling between the different modes which can be solved from the field in a single unit cell of the periodic configuration. The procedure is known as scattering matrix approach (SMA) [Schuhmann et al., 2005]. With the transformation formulas [Collin, 1991]

$$\boldsymbol{T}_{11} = \boldsymbol{S}_{12} - \boldsymbol{S}_{11}\boldsymbol{S}_{22} \setminus \boldsymbol{S}_{21}, \tag{4.2.17}$$

$$\boldsymbol{T}_{12} = \boldsymbol{S}_{11} \setminus \boldsymbol{S}_{21}, \tag{4.2.18}$$

$$\boldsymbol{T}_{21} = -\boldsymbol{S}_{22} \setminus \boldsymbol{S}_{21}, \tag{4.2.19}$$

$$\boldsymbol{T}_{22} = 1 \setminus \boldsymbol{S}_{21}, \tag{4.2.20}$$

the S-matrix can be converted into the T-matrix. The $\setminus$ is operated by multiplying with the inverse matrix. Therefore, the benefits of the S-matrix and of the T-matrix can be combined together. With the full wave simulation, the S-matrix of the unit cell can be found, which then is converted into a T-matrix and cascaded to get the complete behavior of the periodic configuration. This procedure is quite reliable and efficient when the configuration can be described with a limited number of port modes. However, when the field distributions are complicated or the configuration is open, the procedure might meet problems.

4.3 Modal Expansion for Open Structures

For a closed waveguide configuration operating normally in the fundamental mode where only a limited number of modes is sufficient to describe the inside electromagnetic fields, the SMA technique can efficiently yield accurate results. However, in an open waveguide configuration, like a leaky-wave antenna, where the series expansion of the fields is to be replaced by an integral of a continuous spectrum of modes due to the open configuration, the SMA technique might meet a challenge. The Green's functions of the background structure can be involved in the formulation of the SMA to solve the problem of radiation. But the analytical spectral integral formulations of the Green's function are limited to some canonical background configurations and the discretized integral equations for periodic configurations will lead to large numbers of unknowns [Michalski, 1985, Felsen & Marcuvitz, 1994]. Several papers [Derudder et al., 1998, Derudder et al., 2001, Weitsch & Eibert, 2011] presented an alternative solution to this problem which encloses the open waveguide problem by a PEC shield with some artificial absorbing medium, like perfectly matched layer (PML), with very low reflectivity in front of it. Therefore, the integral can be avoided while the problem is closed. Moreover, the representation in a series expansion is exact.

The traditional PML which was first introduced by Bérenger [Bérenger, 1994] is numerically complicated and formulated with uniaxial anisotropic material characteristics and complex thickness. As outlined in [Derudder et al., 2001], the electromagnetic characteristic of PML as shown in Fig. 4.3, which has the length of d_{PML}, can be expressed as

$$\bar{\varepsilon} = \varepsilon_0 \bar{M}, \tag{4.3.1}$$

$$\bar{\mu} = \mu_0 \bar{M}, \tag{4.3.2}$$

with

$$\bar{M} = (\alpha(z)\hat{x} + \alpha(z)\hat{y} + 1/\alpha(z)\hat{z}), \tag{4.3.3}$$

and

$$\alpha = 1 + (\kappa_0 - 1)f(z) - j\frac{\sigma_0}{\omega\varepsilon_0}f(z). \tag{4.3.4}$$

κ_0, σ_0, and $f(z)$ describe the type of PML. The length of the PML d_{PML} can be rewritten as an isotropic layer with a complex thickness

$$\tilde{d}_{\mathrm{PML}} = \int\limits_0^{d_{\mathrm{PML}}} \alpha(z')dz', \tag{4.3.5}$$

where $z = 0$ corresponds to the bottom of the PML [Teixeira & Chew, 1996]. However the numerical handling of this kind of PML is not easy.

Therefore, in [Weitsch & Eibert, 2011] a set of simple isotropic lossy absorbing layers was proposed to replace the PML to avoid the numerical difficulties of PML. The set of absorbing layers consists of 6 layers with the electric and magnetic losses gradually and simultaneously increasing. The layers are designed to reduce the reflection for the impinging wave on the layers which makes the impedance of the layers

$$Z_{F0} = \sqrt{\frac{\mu_0}{\varepsilon_0}}\sqrt{\frac{(\mu_r' - j\mu_r'')}{(\varepsilon_r' - j\varepsilon_r'')}} \tag{4.3.6}$$

identical to the value of the free space impedance. In Eq. (4.3.6), $\mu_r' = 1$ and $\varepsilon_r' = 1$ for all layers whereas μ_r'' and ε_r'' stand for the electric and magnetic losses, respectively, and stay constant over frequency. The thickness of the layers increases gradually towards to top. Tab. 4.1 gives one configuration for the absorbing layers. The absorber is placed far away enough from the waveguide structures so that the interference on the radiation field distribution between the waveguide and the absorber can be neglected. Meanwhile the radiation wave can be well absorbed by the absorbing layer. Therefore, the SMA technique mentioned in section 4.2 can be employed with only a discrete set of modes needed in the formulation and the scattering matrix can be efficiently computed.

	$\tan\delta_{\frac{\varepsilon}{\mu}}$	thickness [mm]
Layer 1	0.01	6
Layer 2	0.02	6
Layer 3	0.07	6
Layer 4	0.15	9
Layer 5	0.30	12
Layer 6	0.8	10

Table 4.1: Configuration of the set of absorbing layers depicted in Fig. 4.4.

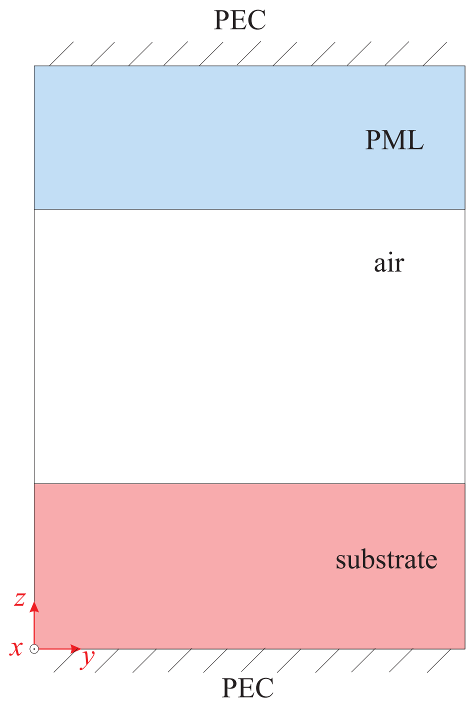

Figure 4.3: The closed equivalence for an open waveguide structure with PML placed in front of a PEC enclosure.

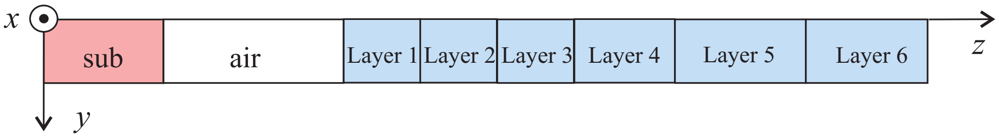

Figure 4.4: The configuration of absorbing layers.

4.4 Eigenproblem Solution with External Excitations

Another method to simplify the eigenvalue searching procedure is called the method of fundamental solutions (MFS), which is a boundary method for the solution of certain elliptic boundary value problems [Karageorchis, 2001]. The method approximates the solution of the problem with a linear combination of the fundamental solutions corresponding to the sources (singularities) which are placed at some fixed places outside the domain of the problem. The unknown coefficients of the fundamental solutions have to satisfy the boundary conditions. This method can be applied when the fundamental solutions for the governing equations are available. When the propagation of electromagnetic waves is in study, the governing equations are the well-know Maxwell's equations, which can for certain configurations be simplified to the Helmholtz equation

$$\nabla^2\phi(P) + k^2\phi(P) = 0, \quad P \in \Omega, \tag{4.4.1}$$

with

$$\phi(P) = 0, \quad P \in \partial\Omega, \tag{4.4.2}$$

$$\text{or}$$

$$\frac{\partial\phi(P)}{\partial n} = 0, \quad P \in \partial\Omega, \tag{4.4.3}$$

where Ω is a bounded domain with boundary $\partial\Omega$, P is the observation point on the boundary of the domain Ω, ϕ represents the electromagnetic wave, k is the cutoff wavenumber. Eq. (4.4.2) and (4.4.3) represent the Dirichlet boundary condition and Neumann boundary condition, respectively. In the MFS for certain elliptic boundary value problem, the solution ϕ can be approximated by a linear combination of functions in the form of

$$\phi_n(\boldsymbol{c}, \boldsymbol{Q}; P, k) = \sum_{n=1}^{N} c_n f_1(P, Q_n), \quad P \in \bar{\Omega}, \tag{4.4.4}$$

where c_n are the unknown coefficients, $\bar{\Omega}$ is a bounded domain containing the domain Ω. $\boldsymbol{Q}$ contains the coordinates of the excitations Q_n which lie outside Ω, inside $\bar{\Omega}$. The function

$$f_1(P, Q_n, k) = -\frac{j}{4} H_0^{(2)}(kr(P, Q_n)) \tag{4.4.5}$$

is a fundamental solution of the Helmholtz equation for 2D elliptic boundary value problems. Here $r(P, Q_n)$ represents the distance between the observation points P and the excitations Q_n, $H_0^{(2)}$ is the Hankel function of the second kind of order zero [Abramowitz & Stegun, 1984]. The excitations can be placed on the boundary $\partial\bar{\Omega}$ of the domain $\bar{\Omega}$ containing Ω while the observation points $\{P_m\}_{m=1}^{M}$ are located on the boundary $\partial\Omega$. According to the boundary conditions in Eq. (4.4.2), the coefficients c are determined so that

$$\phi_n(\boldsymbol{c}, \boldsymbol{Q}; P_m, k) = 0, \quad m = 1, 2, \ldots, N. \tag{4.4.6}$$

This leads to a set of complex algebraic equations for the coefficients c in the form of

$$G(k)c = 0, \tag{4.4.7}$$

where the coefficients of the matrix G can be expressed as

$$G_{m,n}(k) = -\frac{j}{4} H_0^{(2)}(kr(P_m, Q_n)), \quad m, n = 1, 2, \ldots, N. \tag{4.4.8}$$

In order to obtain a nontrivial solution the determinant of $G(k)$ must vanish which occurs for certain values of k. Consequently these values of k are the eigenvalues of the problem (4.4.1). This procedure is usually much easier to implement than the boundary integral equation formulation and can reach faster convergence with fewer degrees of freedom required but maintaining comparable accuracy. Additionally the method is robust for different kinds of boundary conditions. However, the former researches [Kitagawa, 1988, Kitagawa, 1991] indicated that the location of the external excitation would strongly influent the convergence of the method, especially for the boundaries which are not smooth with many edges and corners.

4.5 Dispersion and Modes

The dispersion behavior is one of the focuses in periodic structure analysis. Dispersion can be categorized in different classes, like mode dispersion and material dispersion. In this work, only the mode dispersion is studied.

Definition of Modes

The electromagnetic fields satisfy Helmholtz equations. For example, a TE or TM wave propagates with a propagation constant β in a waveguide whose cross section is uniform along the y-axis as shown in Fig. 4.5, the electromagnetic fields can be represented as $\phi(x, z)e^{-j\beta y}$ and satisfy Helmholtz equation

$$(\nabla_t^2 + k_c^2)\phi(x, z) = 0, \tag{4.5.1}$$

where ∇_t is the Nabla operator in the transverse plane, here the $x - z$ plane. $k_c = \sqrt{k_x^2 + k_z^2}$ is called cutoff wave number which is a constant quantity and depends only on the geometry of the guide. Once k_c is obtained, the propagation constant $\beta = k_y$ is given by

$$\beta = k_y = \sqrt{k^2 - k_c^2}, \tag{4.5.2}$$

with $k = \omega\sqrt{\mu\varepsilon}$ the wavenumber of the material filling the transmission line or waveguide region. The electromagnetic fields also need to satisfy some boundary conditions, for example Dirichlet's boundary condition

$$\phi(x, z) = 0, \text{ on the boundary,} \tag{4.5.3}$$

or Neumann's boundary condition

$$\frac{\partial \phi}{\partial n} = 0, \text{ on the boundary.} \tag{4.5.4}$$

The problem of solving the electromagnetic wave propagation in a uniform waveguide with a perfectly conducting wall is reduced to the problem of finding eigenfunctions and eigenvalues for the two dimensional boundary problems [Ishimaru, 1991]. Here the function $\phi(x, z)$ satisfying Eq. (4.5.1) is called the eigenfunction and constant k_c is the eigenvalue. There can be a set of doubly infinite number of eigenfunctions

$$\begin{aligned} \phi_{mn},\ m &= 0, 1, 2, ..., \infty, \\ n &= 0, 1, 2, ..., \infty, \end{aligned} \tag{4.5.5}$$

and the corresponding eigenvalue k_{mn} according to different boundary conditions. These eigenfunctions are considered as modes. For example the TEM mode is the transverse electromagnetic mode with no longitudinal field components, and TE is the transverse electric mode while TM is the transverse magnetic mode. Fig. 4.6 illustrates some examples of different modes in a rectangular waveguide [Pozar, 2004].

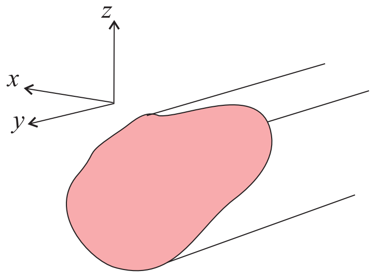

Figure 4.5: A waveguide structure with a uniform cross-section along the y-axis.

Orthogonality of Different Modes

The eigenfunctions ϕ_{mn} are orthogonal to each other, which can be proved as following. If ϕ_{mn} and $\phi_{m'n'}$ are considered to be two eigenfunctions, they must satisfy Helmholtz equation (4.5.1)

$$(\nabla_t^2 + k_{mn}^2)\phi_{mn} = 0, \tag{4.5.6}$$

$$(\nabla_t^2 + k_{m'n'}^2)\phi_{m'n'} = 0. \tag{4.5.7}$$

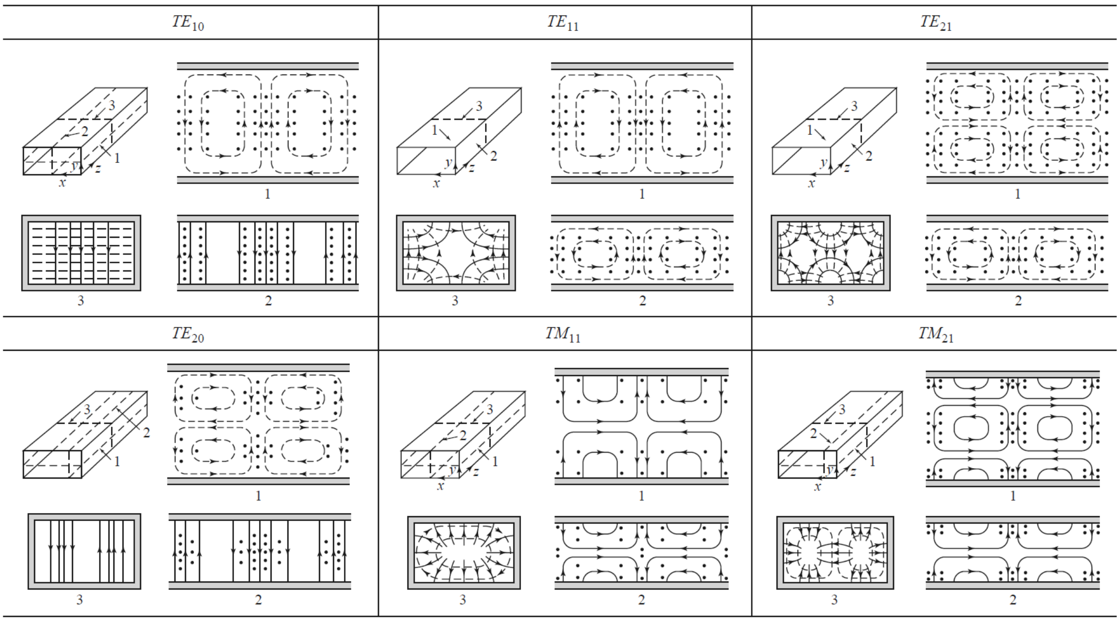

Figure 4.6: Field distributions for the lower-order modes of a rectangular waveguide [Pozar, 2004].

Multiply Eq. (4.5.6) with $\phi_{m'n'}$ and Eq. (4.5.7) with ϕ_{mn} and subtract one from the other to get

$$\phi_{m'n'}\nabla^2\phi_{mn} - \phi_{mn}\nabla^2\phi_{m'n'} = (k^2_{m'n'} - k^2_{mn})\phi_{mn}\phi_{m'n'}. \tag{4.5.8}$$

Integrating both sides of Eq. (4.5.8) with Green's second identity we can get

$$\int_l \left(\phi_{m'n'}\frac{\partial\phi_{mn}}{\partial n} - \phi_{mn}\frac{\partial\phi_{m'n'}}{\partial n}\right) dl = (k^2_{m'n'} - k^2_{mn})\int_s \phi_{m'n'}\phi_{mn} ds, \tag{4.5.9}$$

where s is the area of the cross section and l is the contour of it, $\partial/\partial n$ is the normal derivative with n outward from s. Since ϕ_{mn} and $\phi_{m'n'}$ satisfy either Dirichlet's or Neumann's boundary condition as shown in Eq. (4.5.3) and (4.5.4), the left side of Eq. (4.5.9) will vanish, resulting in

$$(k^2_{m'n'} - k^2_{mn})\int_s \phi_{m'n'}\phi_{mn} ds = 0. \tag{4.5.10}$$

Therefore, when $m \neq m'$ and $n \neq n'$, $k_{mn} \neq k_{m'n'}$, and Eq. (4.5.9) must be zero. The eigenfunctions ϕ_{mn} satisfy the orthogonality condition

$$\int_s \phi_{mn}\phi_{m'n'} ds = N_{mn}\delta_{mm'}\delta_{nn'}, \tag{4.5.11}$$

with

$$\delta_{mm'} = \begin{cases} 1 & \text{for} \quad m = m' \\ 0 & \text{for} \quad m \neq m' \end{cases} , \tag{4.5.12}$$

and N_{mn} is the normalizing factor

$$N_{mn} = \int_s \phi_{mn}^2 ds. \tag{4.5.13}$$

The other properties of eigenfunctions can be found in appendix 10.1.

Hybrid and Degenerate Modes

Transverse modes like TEM, TE and TM are not the only cases in reality. In most cases, hybrid modes which have nonzero electric and magnetic fields in the direction of propagation exist. The hybrid modes are named in HE_{nm} or EH_{nm} depending on whether TE or TM modes are dominant [Ishimaru, 1991].

When the modes propagate at the same frequency and share the same longitudinal propagation constant, the modes are called degenerate modes. One common example is in the rectangular waveguide, TE_{mn} is degenerate with $\mathrm{TM}_{m'n'}$ when $m = m'$ and $n = n'$. Fig. 4.7 depicts the electromagnetic field distribution of TE_{11} and TM_{11} in a rectangular waveguide which has both the cutoff frequency of $f_c = 16.145$ GHz and the propagation constant of $\beta = 48.02$ per meter. However, from the field distribution in the cross section of the waveguide the different modes can be clearly distinguished.

Mode and Material Dispersions

Dispersion analysis is one of the key research topics in periodic structure studies. If a wave propagates on a transmission line along the direction of y-axis, the phase velocity can be defined as the ratio of the frequency to the propagation constant

$$v_p = \omega / k_y. \tag{4.5.14}$$

When k_y is not a linear function of frequency, the phase velocity will be different for different frequencies ω, which means a waveform consisting of different frequency components will be distorted. This kind of variation of phase velocity with frequency is called *dispersion*. As can be seen from Eq. (4.5.14), when $k_y = k$ as for the TEM wave, the dispersion is only due to the dielectric material filling in the waveguide or transmission line. Therefore, it is named as *material dispersion*. The material dispersion is caused by the variation of the refractive index with frequency and can be described as Sellmeier's equation [Ishimaru, 1991] in dielectric materials.

However, for TE, TM or hybrid modes with $k_c \neq 0$, the dispersion also depends on the mode structure. If the refraction index of the material is assumed constant over

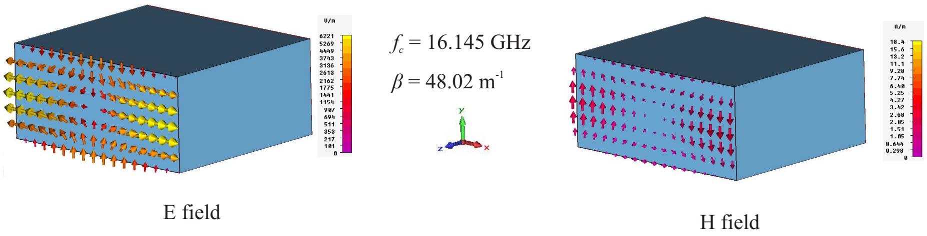

(a) TE_{11}

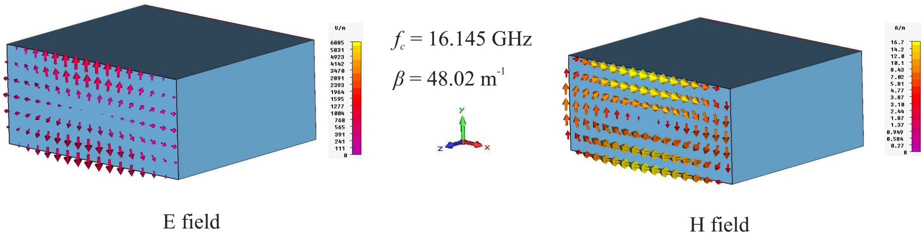

(b) TM_{11}

Figure 4.7: Degenerate modes TE_{11} and TM_{11} in a rectangular waveguide, which have both the cutoff frequency of 16.145 GHz and propagation constant 48.02 per meter but different electromagnetic field distributions.

frequency, this dispersion, which depends on the mode and therefore the geometry configuration of the transmission line, can be called *mode dispersion*. In this work the refraction index of the material is considered constant over the frequency. Therefore, only the mode dispersion is analyzed. Fig. 4.8 depicts the mode dispersion curves for different modes in a cylindrical waveguide with a radius of 5 mm and filled with the dielectric material with $\varepsilon_r = 2.25$.

Dispersion for 2D Metamaterials

As mentioned in section 3.1.2, in 2D MTMs waves propagates in multi-directions, which makes the dispersion relation $\omega_n(k_x, k_y)$ a 2D function. [Caloz & Itoh, 2006] introduced *Brillouin Zone* to depict the dispersion curve as following. For the 2D MTM in Fig. 3.6 with the unit cell depicted in Fig. 4.9 a square or rectangular lattice network interconnection is assumed.

Fig. 4.10 depicts the spatial and spectral lattice for the 2D structure. The spatial lattice is represented by the generic vector

$$\boldsymbol{R}_{uv} = u\boldsymbol{a}_1 + v\boldsymbol{a}_2, \quad (u, v \in Z), \tag{4.5.15}$$

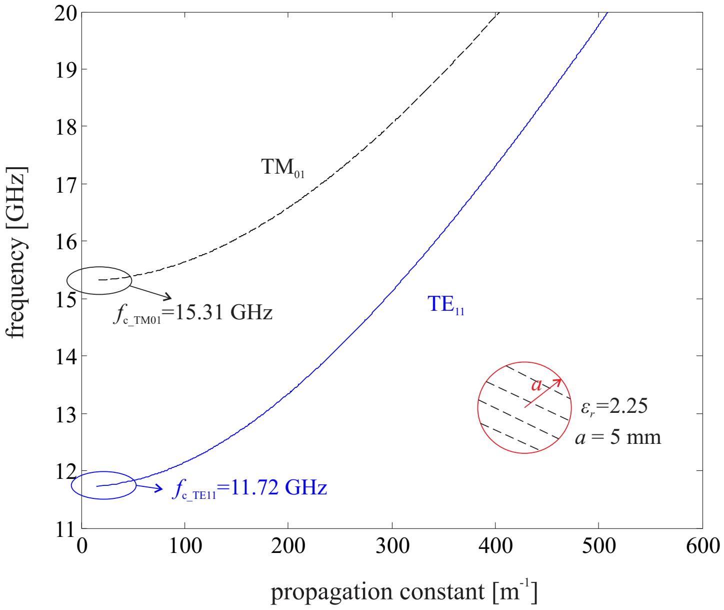

Figure 4.8: Mode dispersion of a cylindrical waveguide with a radius of 5 mm and filled with dielectric material with $\varepsilon_r = 2.25$. Two modes exist in 10-16 GHz, one is TE$_{11}$ with cutoff frequency of 11.72 GHz and the other is TM$_{01}$ with cutoff frequency of 15.31 GHz.

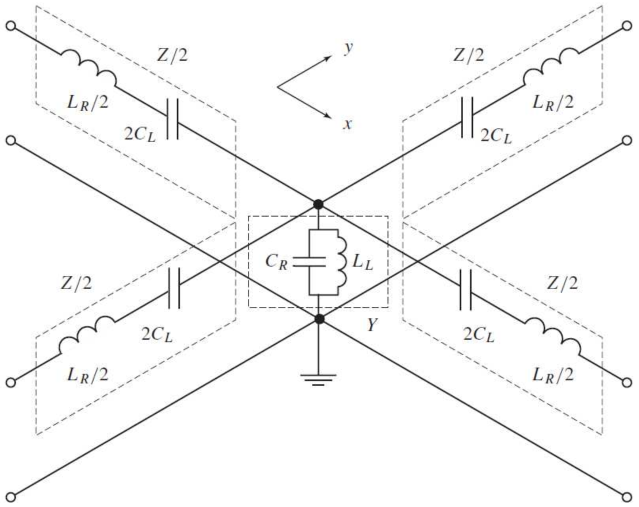

Figure 4.9: The unit cell of the CRLH 2D network in Fig. 3.6 [Caloz & Itoh, 2006].

where

$$\boldsymbol{a}_1 = p_x\hat{x} \quad \text{and} \quad \boldsymbol{a}_2 = p_y\hat{y}. \tag{4.5.16}$$

The spectral lattice is represented by the generic vector

$$\boldsymbol{G}_{hk} = h\boldsymbol{b}_1 + k\boldsymbol{b}_2, \quad (h, k \in Z), \tag{4.5.17}$$

where

$$\boldsymbol{b}_1 = k_x\hat{x} = (\frac{2\pi}{p_x})\hat{x} \quad \text{and} \quad \boldsymbol{b}_2 = k_y\hat{y} = (\frac{2\pi}{p_y})\hat{y}. \tag{4.5.18}$$

One spectral period centered at the origin of Floquet function $\xi(x, y) = \psi(x, y)e^{j(k_x x + k_y y)}$ is defined as *Brillouin zone* (BZ) of the periodic lattice. Brillouin zone is the square surface $[-\pi/p_x < k_x < +\pi/p_x, -\pi/p_y < k_y < +\pi/p_y]$, which can be reduced to the triangular surface shown in Fig. 4.10 (b) without losing the information when the lattice is symmetric with respect to the x- and y-axis. The triangular surface is called *irreducible Brillouin zone.* For the computation of the dispersion diagram, the irreducible zone can be further reduced to the segment $\Gamma - X - M - \Gamma$

$$\Gamma : \beta = 0, \tag{4.5.19}$$

$$X : \beta = \frac{\pi}{p_x}\hat{x} \quad (Y : \beta = \frac{\pi}{p_y}\hat{y}), \tag{4.5.20}$$

$$M : \beta = \pi(\frac{1}{p_x}\hat{x} + \frac{1}{p_y}\hat{y}), \tag{4.5.21}$$

while the segment includes the most important symmetry points Γ, X (also Y when the lattice is anisotropic) and M, where the maximum diffractions take place in Bragg regime [Kittel, 1964]. Therefore, the wavenumbers k_x and k_y along the BZ can be derived according to the matrix system as [Caloz & Itoh, 2006]

$$\Gamma - X(0 < k_x p_x < \pi, k_y p_y = 0) : k_x = \frac{1}{p_x}\cos^{-1}(1 - \frac{\chi}{2}), \tag{4.5.22}$$

$$X - M(k_x p_x = \pi, 0 < k_y p_y < \pi) : k_y = \frac{1}{p_y}\cos^{-1}(3 - \frac{\chi}{2}), \tag{4.5.23}$$

$$M - \Gamma(0 < k_u p_u < \pi, u = x, y) : k_u = \frac{1}{p_u}\cos^{-1}(1 - \frac{\chi}{4}), \tag{4.5.24}$$

where χ is defined as

$$\chi = (\frac{\omega}{\omega_R})^2 + (\frac{\omega_L}{\omega})^2 - \kappa\omega_L^2, \tag{4.5.25}$$

$$\omega_R = \frac{1}{\sqrt{L_R C_R}} \text{ (rad/s)}, \tag{4.5.26}$$

$$\omega_L = \frac{1}{\sqrt{L_L C_L}} \text{ (rad/s)}, \tag{4.5.27}$$

$$\kappa = L_R C_L + L_L C_R \text{ (s/rad)}^2. \tag{4.5.28}$$

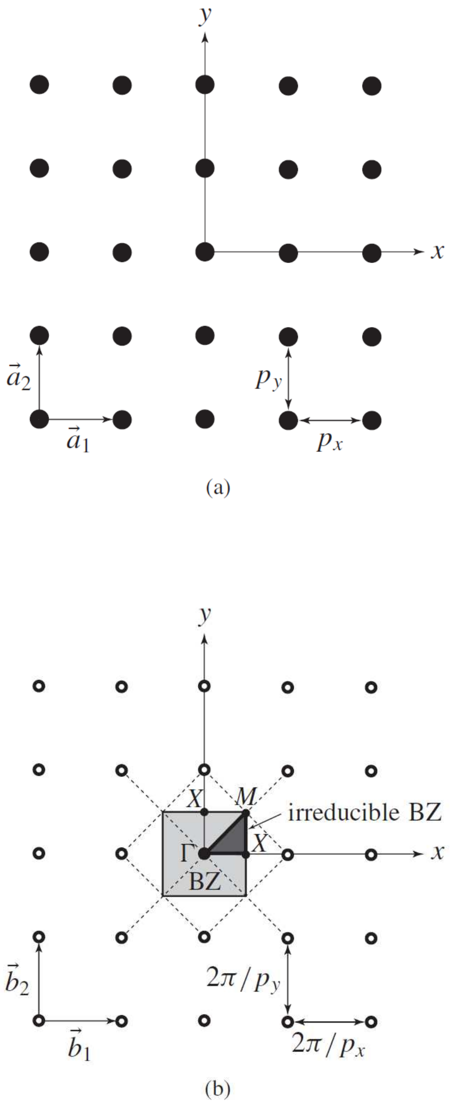

Figure 4.10: Square lattices for a 2D structure. (a) Spatial lattice. (b) Spectral lattice [Caloz & Itoh, 2006].

L_R, C_R, L_L and C_L are the elements that compose the equivalent circuit of the unit cell of the 2D MTM shown in Fig. 4.9. The details of the matrix system of MTMs can be found in appendix 10.2. Fig. 4.11 depicts the balanced dispersion relation of the CRLH network TL of Fig. 3.6(b) in the conventional $\Gamma - X - M - \Gamma$ diagram and the 2D curve $f_n(k_x, k_y)$ [Caloz & Itoh, 2006]. However, this kind of Brillouin zone depiction for the dispersion diagram is under the assumption that the attenuation of the structure can be omitted. When the attenuation is taken into account, the wavenumbers k_x and k_y are both turned into complex quantities $k_x' - jk_x''$ and $k_y' - jk_y''$, which will lead to a complex phase shift $\varphi = k_u \hat{u}, u = x, y$.

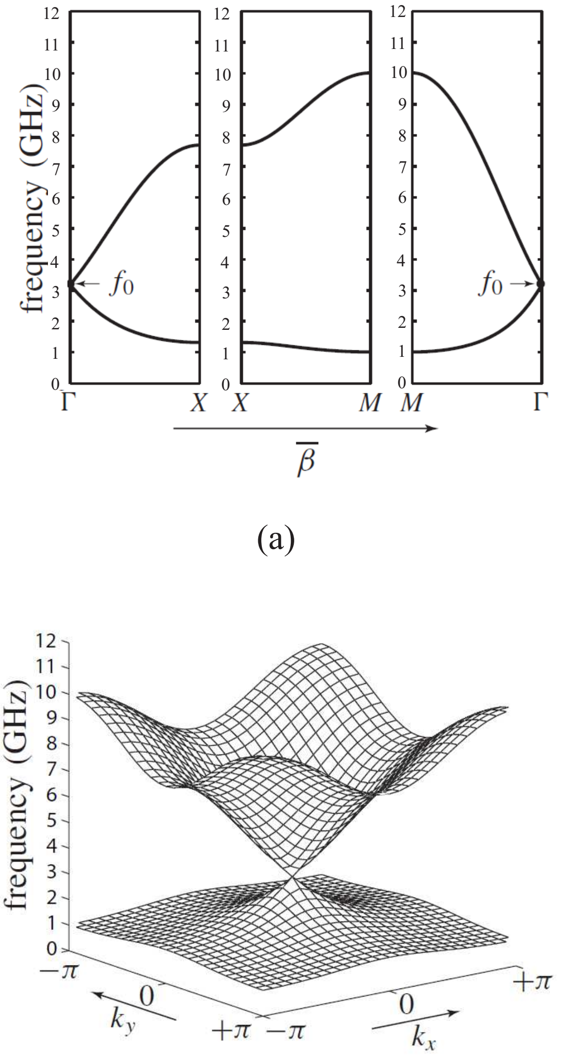

(a)

(b)

Figure 4.11: Dispersion diagram for a 2D balanced CRLH network TL with the parameters of Fig. 3.6(b). (a) Conventional representation along the irreducible BZ. (b) 3D representation of the function $f_n(k_x, k_y)$ $(n = 1, 2)$ over the BZ [Caloz & Itoh, 2006].

5 Driven Eigenproblem Computation

In the previous chapter, many full-wave modeling techniques based on classical numerical methods for periodic configurations like SIWs and metamaterials have been introduced. However, most of them always lead to very slow convergence and often low accuracy due to the large size, the fine details and the often open geometry of periodic configurations which involve complicated complex eigenproblems. Compared to the purely mathematical approaches of the common eigenproblem solvers, here the driven eigenproblem solution is proposed to treat the eigenproblem from a physical point of view by converting it into an excitation problem and simplifying the eigenvalue determination by analogizing the periodic structure to a resonator model [Eibert et al., 2012, Weitsch et al., 2011]. According to Floquet's theorem, a periodic structure can be modeled as one appropriately discretized unit cell with periodic boundary conditions. Considering the unit cell as a resonator, the eigenvalue of it, the resonance frequency, can be efficiently obtained by monitoring the electromagnetic field which usually will reach an extremum at the resonance frequency, when an excitation is provided. This converts the eigenvalue searching procedure for a particular structure to a maximization of the electric field or other observables over the complex plane of the wavevector $\boldsymbol{k}$ for each frequency. The driven eigenproblem computation can be easily implemented in commercial numerical solvers like CST MWS [CST, 2011]. However, the limited boundary flexibility in CST restrains the application to small attenuation scenarios where the perturbation method is employed for guided wave attenuation analysis. Consequently, the approach with CST implementation is unable to analyze the attenuation inside the stop band [Chen et al., 2011]. Therefore, the driven eigenproblem is implemented within the periodic hybrid finite element boundary integral (FEBI) method with the infinite periodic multilayer Green's function [Chen et al., 2011, Eibert et al., 2011]. The implementation within FEBI can directly consider the attenuation by a complex phase shift on the periodic boundary condition which makes it possible to describe the leaky and evanescent modes and compute the attenuation inside the stop band. In this chapter, the fundamentals of the driven eigenproblem computation is introduced. Then the implementation in CST for small attenuation scenarios and the implementation in FEBI are described, respectively.

5.1 Fundamentals of Driven Eigenproblem Computation

5.1.1 Analogy between Eigenproblem and Resonator

As mentioned in chapter 4, the electromagnetic field problem formulation can be considered as an eigenproblem without excitation

$$L(\omega, \boldsymbol{k})\boldsymbol{x} = 0, \tag{5.1.1}$$

where L represents some form of Maxwell's equations with appropriate boundary conditions and material relations. ω and $\boldsymbol{k}$ indicate the frequency and the wavevector, respectively, and $\boldsymbol{x}$ is the vector solution of the operator equation. In numerical solutions, like finite element (FE), finite difference (FD), method of moments, or other hybrid methods, the operator equation is typically discretized and leads to a linear equation system

$$[\boldsymbol{A}_{mn}(\omega, \boldsymbol{k})]\{x_n\} = 0, \tag{5.1.2}$$

$\boldsymbol{A}_{mn}$ are the matrix entries as a function of $(\omega, \boldsymbol{k})$ and x_n are the unknown expansion coefficients of the field solution. The eigenvalues are the pairs of $(\omega, \boldsymbol{k})$, each of which can lead to one or more eigensolutions x indicating one or more propagating modes.

In electric circuits, as shown in Fig. 5.1, a resonator consisting of a capacitor C and an inductor L with a loss conductance G_l in shunt connectin or with a loss resistor R_l in series connection, respectively, can also be expressed in the form of eigenproblems

$$Y(\omega_{\text{res}})U = [j(\omega C - \frac{1}{\omega L}) + G_l]U = 0, \tag{5.1.3}$$

$$Z(\omega_{\text{res}})I = [j(\omega L - \frac{1}{\omega C}) + R_l]I = 0. \tag{5.1.4}$$

For the resonator, the eigenvalue is the resonance frequency ω_{res}, which will be a complex quantity for lossy systems and become real if G_l and R_l vanish. For electric circuits, it is convenient to analyze the resonance behavior by applying an excitation to the resonator and observing the reaction to the excitation, which is normally conducted by measurements.

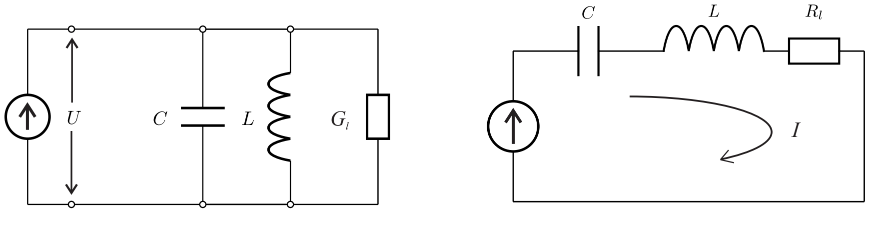

(a) shunt resonator (b) series resonator

Figure 5.1: Basic circuits for shunt and series resonators.

Here the analogy between eigenproblem and resonator can be utilized for the solution of the eigenproblem where the eigenproblem can be considered as a kind of a resonator subject to specific boundary conditions. The eigenvalue searching procedure is then transformed into an excitation problem in the eigenvalue domain. Although the treatment of eigenproblems as excitation problems has been introduced for a long time, in the former researches, e.g. [Davidson, 2005, Baum et al., 1991, Bondeson et al., 2005], the eigenproblems were excited all in the time domain and the eigenvalues were extracted from the time domain observations. The time domain excitation is restricted by the limited observation time and unable to focus the entire excitation energy into an isolated eigenfrequency. In contrast, the driven method in this work directly works in the domain of the eigenvalue and can focus the entire excitation energy into one isolated eigenmode. With complex propagation constants, the individual eigenvalues with narrow resonance singularities can be easily analyzed.

5.1.2 Resonator and Excitation Setup

In periodic configurations, according to Floquet's theorem, the structure can be modeled in one appropriately discretized unit cell with periodic boundary conditions. Fig. 5.2 illustrates the equivalent circuit of the eigenproblem for the structure under analysis which is analogized to a virtual resonator. To find out the eigenvalue for the resonator, one efficient way is to stimulate the resonator by an excitation and monitor the resonance behavior. It is possible to provide the excitation through a port, which is available in many commercial EM solvers like CST MWS. Additionally the port resistors can be used to regularize the singular resonance behavior without causing a modification of the resonance frequency of the original problem. One of the two ports can be used as an input port for the excitation, while the other port works as the output port for the monitor. Besides the port voltage across the port resistor, the other observable of the field solution like the electric field inside the solution domain or some integral measure of it can be monitored. For the port excitation the S-parameters can be directly obtained to locate the resonance frequency. However, this kind of port excitation might introduce reactive coupling elements due to the coupling of the ports to the field problem and therefore influence the resonance curve. The other observables such as the fields in the solution domain can be better indicators of the resonance. Another method to excite the resonator is to impress current densities somewhere in the solution domain which can be particularly designed to select a desired eigenmode, where in principle all relevant eigenmodes can be excited. With some start estimations based on the previous solutions, the iterations of the solutions of the excitation problem will be repeated for slightly changed parameters to find pairs of $(\omega, \boldsymbol{k})$ as eigenvalues. For example one possibility is to fix the wavenumber and sweep the frequency, or the other way around. So that pairs of $(\omega, \boldsymbol{k})$ as eigenvalues over a frequency range can be found to form the dispersion curve and the attenuation curve.

5.2 Port Excitation and the Perturbation Method in Small Attenuation Scenarios

For periodic structures, a guided wave can be modeled in one appropriately discretized unit cell with periodic boundary conditions and some pre-defined phase shift $\Delta\varphi$ in the direction of the wave propagation (e.g. $y-$direction in Fig. 5.3). Set up two ports to the unit cell with one port as the input port and the other as the output port. Through

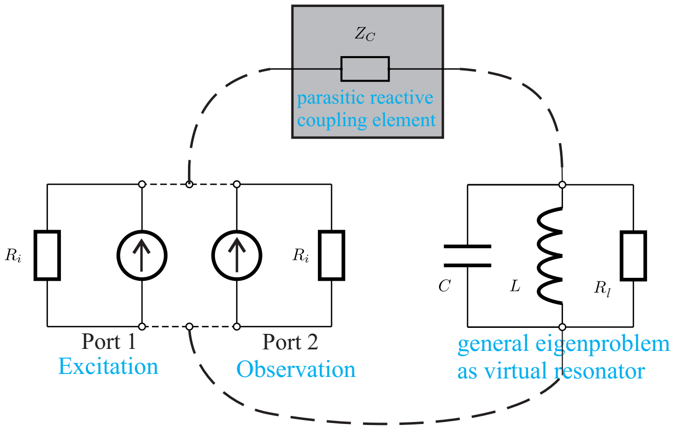

(a) Equivalent circuit of eigenproblem with port excitation

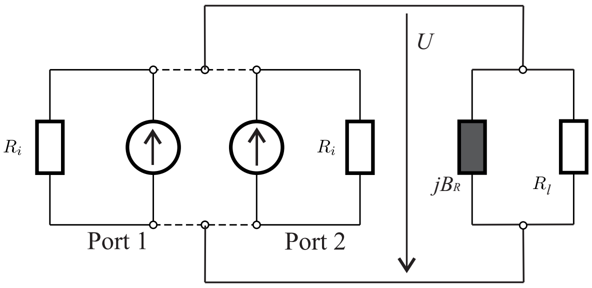

(b) Equivalent circuit at resonance

Figure 5.2: Equivalent circuit of the general eigenproblem with port excitation. Dependent on the port configuration, a parasitic reactive coupling element can be introduced. (b) shows the port voltage applies always on the shunt loss resistor of the virtual resonator, which can be used in loss calculation.

the input port the excitation can be provided to stimulate the unit cell. Meanwhile the resonance behavior can be monitored through the output port, e.g. monitoring the S-parameters over the port. With one fixed phase difference $\Delta\varphi$ the resonance frequency can be found by sweeping the excitation frequency ω which can lead to some propagation constant k'

$$k' = \frac{\Delta\varphi}{p} = \frac{\omega_{\mathrm{res}}}{c_r}. \tag{5.2.1}$$

Here, p is the length of the unit cell, c_r is the wave propagation velocity in the material. $\Delta\varphi$ is the phase difference between the periodic boundary condition in wave propagation direction. S-parameters can be easily used to locate the resonance frequency while the reflection and transmission coefficients will reach extrema at the resonance frequency.

However, the reactive elements introduced by the coupling between the ports and the resonator will possibly cause a shift of the resonance frequency. As we known, the resonance frequency ω_{res} is corresponding to the frequency where the transmitted power in the unit cell is maximal. Therefore, besides the S-parameter over the port, the other observables like the electric field inside the unit cell or some integral measure of it can be monitored to reduce the influence of the port coupling.

The losses in electromagnetic structures consist of dielectric losses, conductive losses and radiation losses when the structures are not closed, e.g. SIWs with periodic bilateral gaps. In small attenuation scenarios, the perturbation method can be employed to analyze the losses [Kong, 2009]. If a unit cell of the SIW shown in Fig. 5.3 is considered and the $y-$direction is the wave propagation direction, assuming

$$P(y) = P(0)e^{-2k''y}, \tag{5.2.2}$$

where $P(y)$ is the power flowing along the $y-$direction, $P(0)$ is the power at the position $y = 0$, and k'' is the attenuation constant which is correspondingly obtained as

$$k'' = -\frac{1}{2}\frac{dP(y)}{dy}\frac{1}{P(y)} = -\frac{1}{2}\frac{\Delta P(y)}{\Delta y}\frac{1}{P(y)}. \tag{5.2.3}$$

$P(y)$ can be calculated as the integral of the time average energy at the cross section in propagation direction at the position y. Δy is the length of the unit cell. $\Delta P(y)$ is here the power lost within one unit cell, which can be defined as the power dissipated in the loss resistor R_l of the equivalent resonator circuit as depicted in Fig. 5.2. It can be computed with

$$\Delta P = \frac{1}{2}\frac{U^2}{R_l}, \tag{5.2.4}$$

by the input voltage and the loss resistance at the resonance frequency, which are all easily monitored at the input port.

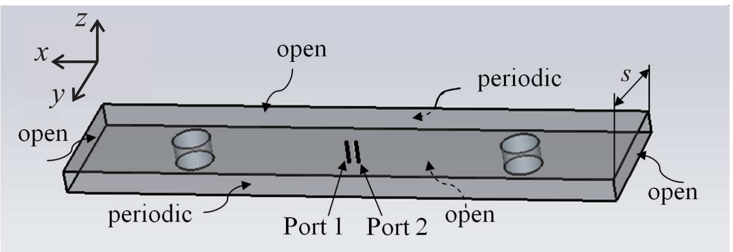

Figure 5.3: The unit cell of a SIW as depicted in Fig. 3.7 with the port excitation in CST MWS.

This kind of port excitation can be conveniently realized in any EM solver, e.g. the frequency domain solver in CST MWS. However, most of them have certain drawbacks like the limited boundary flexibility, which allows only real phase shift on the periodic boundary leading to the inability of the description for leaky and evanescent modes. Therefore, the application will be restrained to small attenuation scenarios. Additionally due to the intrinsic characteristics of the perturbation method, which can only analyze the transmitted power, it is impossible to calculate the loss inside the stop band.

5.3 Current Excitation and Implementation in FEBI

The other possible excitation method such as impressed current densities somewhere inside the solution domain has some advantages over the port excitations. Without the influence of port coupling, the current density excitation can work with an arbitrary observable like the electric field within the solution domain or some integral measure of it. Additionally this excitation can be particularly designed to select a desired eigenmode, where in principle all the relevant eigenmodes can be excited [Eibert et al., 2012]. The current densities excitation can be implemented within the periodic hybrid finite-element boundary-integral (FEBI) method with the infinite periodic multilayer Green's function. The implementation in FEBI can directly consider the attenuation by a complex phase shift on the periodic boundary condition and Green's function. Therefore, the leaky and evanescent modes can be described and the attenuation inside the stop band can be computed.

5.3.1 Fundamentals of FEBI

Solving the governing Maxwell's partial differential equations can help to investigate the electromagnetic behavior of a system. However, Maxwell's equations can not be solved analytically except for some idealized geometries. Therefore, a number of numerical methods has been developed to solve Maxwell's equations for complex structures. The finite element methods and the integral equation methods, which seek the numerical solutions for Maxwell's equations, are widely used.

Finite Element Methods

The finite element method (FEM) is a numerical technique for obtaining approximate solutions for the boundary-value problems, which was first proposed in the 1940s and has been developed and applied extensively to different mathematical and engineering problems [Jin, 2002]. FEM replaces the unknown function on an entire continuous domain by some simple interpolation functions with unknown coefficients on a number of subdomains. Therefore, a finite element analysis will first discretize or subdivide the domain of the problem, and then select the interpolation functions to form a system of equations and find out the solution of the system of equations. FEM permits general geometrical discretization elements, e.g. lines in 1D, triangles or rectangles in 2D, and tetrahedral or bricks in 3D. In electromagnetic problems, FEM solves Maxwell's equations in the direct manner by using either the variational analysis or the weighted residuals where an electric field formulation can be expressed as

$$F_v(\boldsymbol{E}) = \frac{1}{2}\iiint\limits_V \left[\frac{1}{\mu_r}(\nabla \times \boldsymbol{E}) \cdot (\nabla \times \boldsymbol{E}) - k_0^2 \varepsilon_r \boldsymbol{E} \cdot \boldsymbol{E}\right] dv$$

$$+ \frac{1}{2}\iint\limits_S [\boldsymbol{E} \cdot (\hat{n} \times \nabla \times \boldsymbol{E})]\, ds + \iiint\limits_V \boldsymbol{E} \cdot \left[jk_0 Z_0 \boldsymbol{J}_s + \nabla \times \frac{\boldsymbol{M}_s}{\mu_r}\right] dv \tag{5.3.1}$$

and

$$F_w(\boldsymbol{E}) = \iiint\limits_V \left[\frac{1}{\mu_r}(\nabla \times \boldsymbol{E}) \cdot (\nabla \times \boldsymbol{W}) - k_0^2 \varepsilon_r \boldsymbol{E} \cdot \boldsymbol{W}\right] dv$$

$$+ \iint\limits_S [\boldsymbol{W} \cdot (\hat{n} \times \nabla \times \boldsymbol{E})]\, ds + \iiint\limits_V \boldsymbol{W} \cdot \left[jk_0 Z_0 \boldsymbol{J}_s + \nabla \times \frac{\boldsymbol{M}_s}{\mu_r}\right] dv, \tag{5.3.2}$$

where V is the volume containing the sources, S represents the boundary surface of the volume, J_s and M_s are the equivalent current sources, and $\boldsymbol{W}$ is a weighting function. FEM does not include the radiation condition. Therefore, a mathematical boundary condition or a fictitious absorbing material layer imposed outside the solution domain is required.

Method of Moments Solution of Integral Equation Formulation

The integral equation formulations relate the scattering or radiating field of conducting or homogeneous dielectric materials to the unknown equivalent currents which can be represented by Huygens' equivalent surface currents. For inhomogeneous dielectric bodies volumetric currents can be used, however, with expensive computational effort. The Huygens' equivalent currents $\boldsymbol{J}_s$ and $\boldsymbol{M}_s$ are the tangential components of the magnetic and electric fields, respectively, on a surface S enclosing the scatterer or radiator whose scattered fields $\boldsymbol{E}^{sca}$ and $\boldsymbol{H}^{sca}$ external to the surface S can be considered generated by the equivalent currents and computed using the radiation integrals [Davidson, 2005, Lu & Chew, 1995]

$$\boldsymbol{E}^{sca}(\boldsymbol{r}) = -\oiint\limits_S [\boldsymbol{M}_s(\boldsymbol{r}') \cdot \nabla \times \bar{\boldsymbol{G}}(\boldsymbol{r}, \boldsymbol{r}') + jk_0 Z_0 \boldsymbol{J}_s(\boldsymbol{r}') \cdot \bar{\boldsymbol{G}}(\boldsymbol{r}, \boldsymbol{r}')] ds', \tag{5.3.3}$$

$$\boldsymbol{H}^{sca}(\boldsymbol{r}) = \oiint\limits_S [\boldsymbol{J}_s(\boldsymbol{r}') \cdot \nabla \times \bar{\boldsymbol{G}}(\boldsymbol{r}, \boldsymbol{r}') + j\frac{k_0}{Z_0} \boldsymbol{M}_s(\boldsymbol{r}') \cdot \bar{\boldsymbol{G}}(\boldsymbol{r}, \boldsymbol{r}')] ds', \tag{5.3.4}$$

where

$$\bar{\boldsymbol{G}}(\boldsymbol{r}, \boldsymbol{r}') = (\bar{\boldsymbol{I}} + \frac{\nabla\nabla}{k_0^2}) \frac{e^{-jk_0|\boldsymbol{r}-\boldsymbol{r}'|}}{4\pi|\boldsymbol{r}-\boldsymbol{r}'|}, \tag{5.3.5}$$

$\bar{\boldsymbol{G}}(\boldsymbol{r}, \boldsymbol{r}')$ is the free space dyadic Green's function, $\boldsymbol{r}$ is a field point and $\boldsymbol{r}'$ represents a source point. Z_0 is the free space intrinsic impedance and k_0 is the free space wavenumber.

With the boundary conditions

$$\hat{n} \times (\boldsymbol{E}^{inc} + \boldsymbol{E}^{sca}) = 0, \tag{5.3.6}$$

$$\hat{n} \times (\boldsymbol{E}^{inc} + \boldsymbol{E}^{sca}) = \boldsymbol{J}_s, \tag{5.3.7}$$

Eq. (5.3.3) and (5.3.4) lead to the integral equation formulations. Here $\hat{n}$ is the unit vector normal to the surface and outward directed. When Eq. (5.3.6) is considered, the electric field integral equation (EFIE) is obtained while Eq. (5.3.7) leads to a magnetic field integral equation (MFIE). Linearly combining EFIE and MFIE to get the combined field integral equation (CFIE) can reduce the spurious solutions which might be caused by the singular frequencies (nonphysical interior resonances) when EFIE and MFIE are used independently on a closed surface S. The surface integral equation formulations can make efficient analysis of the conducting and homogeneous dielectric bodies where only the boundary of the scatterer and radiator need to be discretized, but not for inhomogeneous penetrable materials where fictitious volumetric currents are required.

Hybrid Finite-Element Boundary-Integral Method

The hybrid finite-element boundary-integral (FEBI) method combines the advantages of FEM and BI together. FEBI introduces an arbitrary boundary enclosing the structure under analysis. Interior to this boundary FEM is employed, whereas surface integral equation formulations are applied to solve the field in the region exterior to the boundary. The fields interior and exterior can be coupled by the field continuity conditions at the boundary. This hybridization can overcome the disadvantage of domain truncation by the mathematical boundary condition or a fictitious absorbing material layer in FEM which does not include the radiation condition [Davidson, 2005], as well as the expensive computation effort in the surface integral equation formulation for the inhomogeneous penetrable materials where the fictitious equivalent volumetric currents are required.

5.3.2 Implementation of the Driven Method in FEBI

Consider a 2D infinite periodic configuration as illustrated in Fig. 5.4. The geometry or the material distribution is periodic along the x- and y-axis with lattice vector $\boldsymbol{\rho}_a$ and $\boldsymbol{\rho}_b$, respectively. In direction of the z-axis the configuration is divided into several layers. The possibly inhomogeneous parts are included in one layer, which can be represented in a unit cell and discretized with a tetrahedral mesh. Above and below the possibly inhomogeneous layer, there might be some homogeneous layers, which can also be represented with the lattice vectors $\boldsymbol{\rho}_a$ and $\boldsymbol{\rho}_b$. According to Floquet's theorem, the fields in the structure can be expressed as

$$\boldsymbol{E}(\boldsymbol{r} + m\boldsymbol{\rho}_a + n\boldsymbol{\rho}_b) = \boldsymbol{E}(\boldsymbol{r})e^{-j\boldsymbol{k}_{t00}\cdot(m\boldsymbol{\rho}_a + n\boldsymbol{\rho}_b)}, \tag{5.3.8}$$

$$\boldsymbol{H}(\boldsymbol{r} + m\boldsymbol{\rho}_a + n\boldsymbol{\rho}_b) = \boldsymbol{H}(\boldsymbol{r})e^{-j\boldsymbol{k}_{t00}\cdot(m\boldsymbol{\rho}_a + n\boldsymbol{\rho}_b)}, \tag{5.3.9}$$

with

$$\boldsymbol{k}_{t00} = k_{x00}\hat{x} + k_{y00}\hat{y}. \tag{5.3.10}$$

Here, $\boldsymbol{k}_{t00}$ is the wavevector parallel to the xy-plane and corresponding to the $(00)^{th}$ Floquet mode. The fields are solved by FEBI [Eibert et al., 1999] which solves the tetrahedral mesh cell using FE with some periodic boundary conditions (PBCs) where the complex $\boldsymbol{k}_{t00}$ can be considered directly for the lossy structures. On the other hand, on the planar top and bottom surfaces of the FE unit cell mesh and the homogeneous layers above and below it, BI is employed to solve the radiation and scattering of the structure with the appropriate spectral domain 2D periodic Green's functions [Eibert et al., 2003]. Details about the periodic Green's function can be found in appendix 10.3. For the free space above and below the unit cell, the spectral representation of the scalar half-space Green's function of Helmholtz equation

$$G(\boldsymbol{r}, \boldsymbol{r}') = \sum_{m=-\infty}^{+\infty} \sum_{n=-\infty}^{+\infty} \frac{e^{-j\boldsymbol{k}_{tmn}\cdot(\boldsymbol{\rho}-\boldsymbol{\rho}')}}{2Ajk_{zmn}} e^{-jk_{zmn}|z-z'|}, \tag{5.3.11}$$

can be used. $\boldsymbol{\rho}$ is the projection of the field point $\boldsymbol{r}$ on the xy-plane with $\boldsymbol{r} = \boldsymbol{\rho} + z\hat{z}$. $A = |\boldsymbol{\rho}_a \times \boldsymbol{\rho}_b|$ is the cross-section area of the unit cell's top or bottom boundary surface.

$$k_{zmn} = \pm\sqrt{k_0^2 - \boldsymbol{k}_{tmn} \cdot \boldsymbol{k}_{tmn}}, \tag{5.3.12}$$

$$\boldsymbol{k}_{tmn} = \boldsymbol{k}_{t00} + \frac{2\pi}{A}[n(\hat{z} \times \boldsymbol{\rho}_a) + m(\boldsymbol{\rho}_b \times \hat{z})], \tag{5.3.13}$$

are the wavevector of the $(mn)^{th}$ Floquet mode along the z-axis and in xy-plane, respectively. With the complex $\boldsymbol{k}_{t00}$ and the free space wavenumber $k_0 = \omega\sqrt{\mu_0\varepsilon_0}$, the BI representation will induce a nonlinear eigenproblem.

As mentioned in section 5.1, the nonlinear eigenproblem of periodic configurations can be solved by solving the corresponding excitation problem in the domain of the eigenvalue. This can be done by analogizing the unit cell of the periodic structure into a resonator and find the resonance frequency as the eigenvalue by stimulating the resonator with an excitation. In FEBI, other than the port excitations, the current densities excitation which has more mode excitation and observable selection flexibility is selected. Compared to the port excitation, impressed current densities excitation can stimulate one mode more efficiently than the other, so called mode selection. On the other hand, with appropriately arranged electric and magnetic current sources with different polarizations or distributions inside the solution domain, all the relevant modes can be excited, since electric and magnetic fields of one mode are never exactly zero at identical locations [Eibert et al., 2012]. Additionally, for the loss analysis, instead of monitoring the voltage across the port resistors, other observables like the electrical field or the integral measure of it can be monitored to find the resonance frequency. With some start estimations based on the previous solutions, the iterations of the solutions of the excitation problem will be repeated for slightly changed parameters. One possibility is to fix the wavevector $\boldsymbol{k}$ and sweep the frequency ω till the resonance frequency is found. The other way is to make the frequency constant and vary the wavevector which can be considered as a complex quantity so that the propagation modes with stronger attenuations, e.g. evanescent modes or leaky modes, can be monitored.

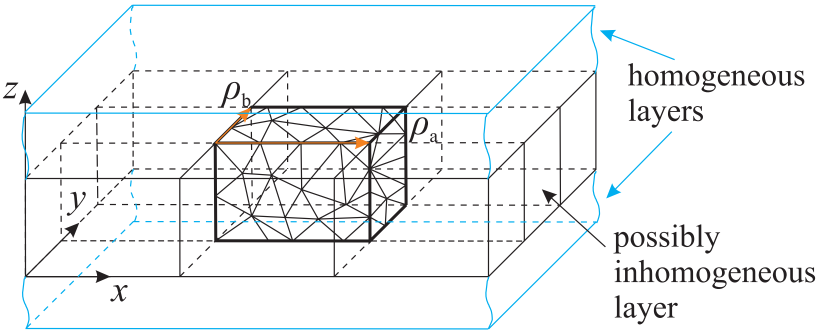

Figure 5.4: 2D infinite periodic configuration.

5.4 Complex Waves

One important topic in the driven method is how to choose the correct sign for the wavenumbers in Eq. (5.3.12). In the open waveguiding configuration, the boundaries are extended to infinity in some direction making discrete modes, which exist in closed waveguiding structures, fall together and merge into a continuous spectrum of modes. Additionally a discrete set of modes can exist for the surface waves. Here the class of geometrical configuration depicted in Fig. 5.5 is considered, which consists of a semi-infinite free-space region bounded by a plane interface which can be either a reactive surface, an ideal conductor, a lossy sheet, or a transition air-media interface. The boundary condition, which is assumed to be independent in x- and y-direction, can be expressed as an impedance function $Z_i(k_z)$ for every single mode i in the transverse z-direction. k_z denotes the transverse wavenumber and a characteristic of the corresponding modes. One line source of either electric or magnetic type is placed at $y = 0$ and parallel to the x-axis. Therefore, the longitudinal representation of modes traveling in $z-$direction at and above the interface $z \geq 0$ can be expressed as

$$G(y,z) = \frac{1}{2} \int\limits_{-\infty}^{\infty} f(k_y) e^{-jk_y y} e^{-jk_z z} dk_y, \tag{5.4.1}$$

which is with a time dependence $e^{j\omega t}$ and consists of a continuous spectrum with the purely real eigenvalues ranging from negative to positive infinity. $f(k_z)$ is a amplitude function depending on the impedance function $Z_i(k_z)$ of the interface as well as the location of the line source. The electric or magnetic line current source will excite TM or TE modes, respectively. $G(y,z)$ is proportional to the x-component of each mode and represents the field expansion as a Fourier transform with respect to k_y when the integration is performed along the real axis in the complex k_y-plane according to [Sommerfeld, 1949]. k_y and k_z are the wavenumbers along y- and z-axis, which satisfy the relation

$$k_y = \pm\sqrt{k_0^2 - k_z^2} \tag{5.4.2}$$

where $k_0 = \omega\sqrt{\mu_0\varepsilon_0}$ is the wavenumber of free space. A two-sheet Riemann surface can be used to interpret the square root function shown in Eq. (5.4.2) where one sheet presents one value or branch and the second sheet is for the other value. The two sheets are linked by arbitrary branch cuts connecting branch points, in Eq. (5.4.2) one pair of which is $k_z = \pm k_0$ and another one is assumed at ∞. Therefore, the Riemann surface is separated by the branch cuts extended from the branch points $\pm k_0$ to infinity and categorized as proper and improper sheets according to physically reasonable and unreasonable field solution, respectively. Additionally the original Sommerfeld integration path along the real k_y-axis is deformed by the branch cuts in the complex k_y-plane. According to the Sommerfeld radiation condition, the proper solution of the problem must vanish at infinity which makes the considered configuration in Fig. 5.5 as

$$\mathrm{Im}(k_z) < 0, \quad \text{where } k_z = k_z' - jk_z'' \tag{5.4.3}$$

to make sure the wave decays with $z \to \infty$. Consequently only the lower half of the k_z-plane satisfies the requirement. Choose the branch cut so that the proper plane which is here the lower half of the k_z-plane is plotted on the top sheet of the two-sheeted Riemann k_y-plane [Tamir & Oliner, 1963] depicted in Fig. 5.6. The upper half of the k_z-plane which is plotted on the bottom sheet of the Riemann plane is improper. The branch cuts for $\mathrm{Im}(k_z) = 0$ and the assumption of infinitesimal losses for the free space wavenumber

$$0 < |\mathrm{Im}(k_0)^2| < |k_0^2|, \tag{5.4.4}$$

can ensure the integration of Eq. (5.4.1) to be along the entire real k_y-axis which is also known as Sommerfeld integration path. Comparing to other branch cuts, this kind of branch cut can make the transverse integral representation obtained by a contour deformation a spectral one [Collin, 1991].

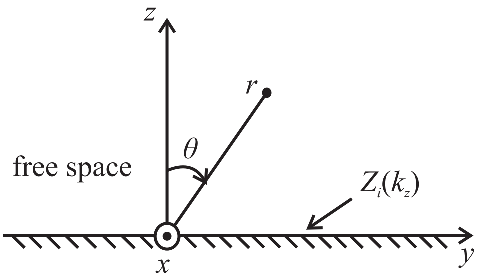

Figure 5.5: Configuration of the plane interface.

If Eq. (5.4.1) is considered in the complex k_z-plane, the transverse representation of the field can be obtained. The former Sommerfeld integration path P is deformed and transformed to a semicircle at infinity for the positive y, as path P' shown in Fig. 5.6. For the negative y, the semicircle will be in the upper half of the top Riemann sheet. Infinity does not contribute to the integral. Therefore, according to Cauchy's theorem

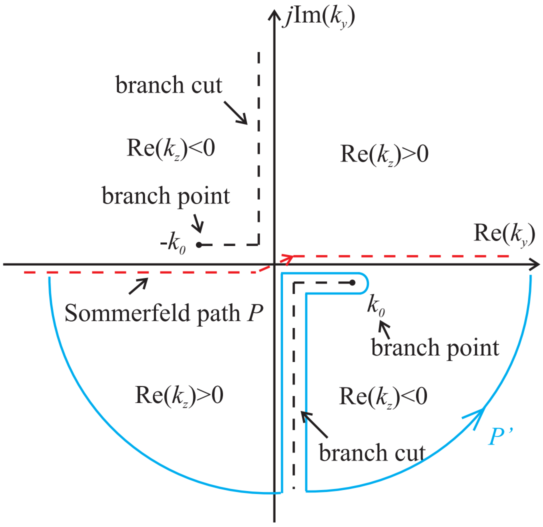

Figure 5.6: The proper Riemann sheet of k_y-plane, where $\mathrm{Im}(k_z) < 0$.

for complex integration Eq. (5.4.1) can be rewritten as

$$G(y,z) = \frac{1}{2\pi}\left[\int_{-\infty}^{\infty} (f(k_y)e^{-jk_y y}e^{-jk_z z}\frac{dk_y}{dk_z})dk_z + 2\pi j \sum \text{residues}\right], \tag{5.4.5}$$

where the integration is performed along the entire real k_z-axis which is the path around the branch cuts. The residues caused by the possible pole singularity can be proper and correspondent to the complex waves which are also called surface waves when the residues locate in the top Riemann sheet of the k_y-plane whereas the improper waves locate in the lower Riemann sheet of the k_y-plane will never be captured by the path P'. Compared to the longitudinal representation in Eq. (5.4.1) which can only generate a continuous spectrum corresponding to the radiation waves which are not bounded to the interface, the transverse representation in Eq. (5.4.5) can yield additionally a discrete spectrum representing the discrete waves associated with a waveguide. Tab. 5.1 summaries some relations between proper/improper waves and the wavenumbers k_y and k_z when $k_y' > 0$ [Ishimaru, 1991].

Complex Floquet Modes with Attenuations

As shown in Fig. 5.7, real Floquet modes are interpreted as discrete samples along the Sommerfeld integration path for non-periodic configurations. If complex Floquet modes with attenuations in the power flow direction are considered, $\mathrm{Im}(k_y)$ becomes negative and deforms the discrete samples as depicted in Fig. 5.7. All complex modes remain on the top Riemann sheet, which are proper, except the modes which are located between the origin and the branch point k. These modes cross the branch cut through a deformation of the Sommerfeld integration path and move to the lower improper Riemann sheet.

Case	k'_y	k''_y	k'_z	k''_z	Wave
	$+$	0	$+$	0	fast wave (waveguide modes)
proper wave	$+$	$-$	$+$	$+$	backward leaky wave
	$+$	0	0	$+$	trapped surface wave
	$+$	$+$	$-$	$+$	Zenneck wave
	$+$	0	$-$	0	plane-wave incidence
improper wave	$+$	$-$	$-$	$-$	
	$+$	0	0	$-$	untrapped surface wave
	$+$	$+$	$+$	$-$	forward leaky wave

Table 5.1: Proper and improper waves in geometry configuration shown in Fig. 5.5 associated with wavenumber $k_y = k'_y - jk''_y$ and $k_z = k'_z - jk''_z$.

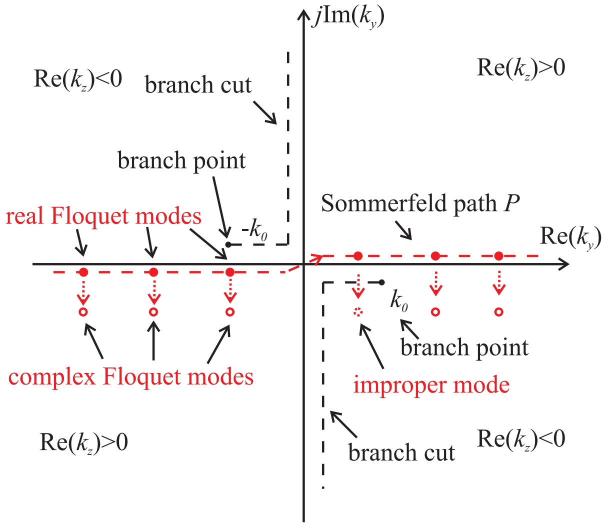

Figure 5.7: The real and complex Floquet modes in the complex transverse wavenumber plane of k_y, where $\mathrm{Im}(k_z) < 0$ and $k_x = 0$, for the waveguide structure as depicted in Fig. 5.5.

Fast and Slow Waves In Leaky-wave Antenna

If the interface in Fig. 5.5 is considered as surface of a leaky-wave antenna, Eq. (5.4.2) can be rewritten as

$$k_z = \pm\sqrt{k^2 - k_y^2}, \tag{5.4.6}$$

when the laterally constant field distribution in x-direction, $k_x = 0$ is assumed. A scalar plane wave can be represented as

$$\psi(y,z) = \psi_0 e^{-jk_y y} e^{-jk_z z}. \tag{5.4.7}$$

Therefore, the propagation of the field can be divided into two cases

$$\begin{cases} k_z \in \mathbf{Re} & \text{if } |k_y| < k_0, \\ k_z \in j\mathbf{Im} & \text{if } |k_y| > k_0. \end{cases} \tag{5.4.8}$$

An imaginary k_z will make the corresponding exponent in Eq. (5.4.7) real which means no wave radiation in positive z-direction. Fig. 5.8 demonstrates the relation. The light line where $|k_y| = k_0$ separates the radiation and purely guided waves.

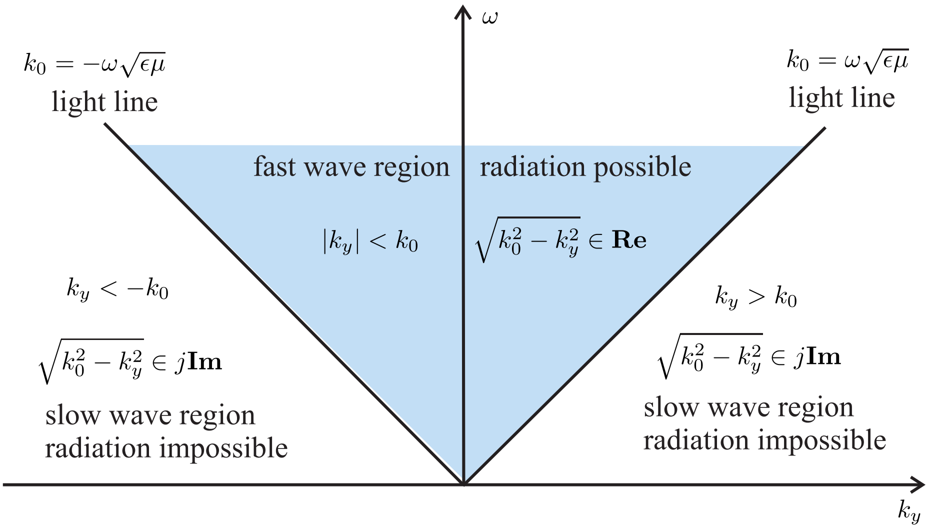

Figure 5.8: The fast and slow wave regions separated by the light line, indicating radiating waves and purely guided waves.

6 Eigenvalue Searching Acceleration in Driven Eigenproblem Computation

6.1 Equivalence Between Eigenvalue Searching and Maximization

In the driven resonator model, the resonance frequency, which is the eigenvalue of a resonator, can be easily located by monitoring the electromagnetic fields, like the electric field or another observable, which will reach an extremum at the resonance frequency. From Eq. (5.3.8) to (5.3.10), the electromagnetic field in a certain point inside the solution domain can be considered as a function of wavevector $\boldsymbol{k}_{k00}$. Therefore, the eigenvalue searching procedure of pairs of $(\omega_{\text{res}},\boldsymbol{k}_{t00})$ is converted to a maximization of the electromagnetic field as the function of $\boldsymbol{k}_{t00}$ for each frequency. When the structure under analysis is lossy and the leaky and evanescent modes are taken into account, $\boldsymbol{k}_{t00}$, k_{x00} and k_{y00} are defined complex, which makes the maximum searching procedure of the electromagnetic field as a multi-dimensional maximization over a complex plane of $\boldsymbol{k}_{t00}$ for one frequency. Fig. 6.1 shows one example of a periodic structure. The magnitude of the electric field at some observation point within the unit cell of the structure under analysis at 11.4 GHz over the complex plane of wavenumber k_{y00} is depicted, where every maximum indicates one eigenmode. In this chapter, various searching algorithms are introduced to accelerate the maximum searching procedure.

6.2 Brent's Method in One Direction Searching

For the maximization in one direction, there are many searching methods to choose, like linear bracket method, golden section search, parabolic interpolation, Newton's method with derivatives. For simplicity and good convergence, the Brent's method [Brent, 2002] combining the inverse parabolic interpolation and the golden section search is employed here. The inverse parabolic interpolation forms the parabola fitted through three points as depicted in Fig. 6.2. The abscissa x for the maximum of a parabola through three points $f(a)$, $f(b)$, and $f(c)$ can be expressed as

$$x = b - \frac{1}{2}\frac{(b-a)^2[f(b)-f(c)]-(b-c)^2[f(b)-f(a)]}{(b-a)[f(b)-f(c)]-(b-c)[f(b)-f(a)]}, \tag{6.2.1}$$

with which $f(x)$ can be calculated and compared to $f(a)$, $f(b)$, $f(c)$. The point among a, b, c, and x with the smallest f value is thrown away and a next parabola can be formed through the remaining three points until the maximum of the function f does

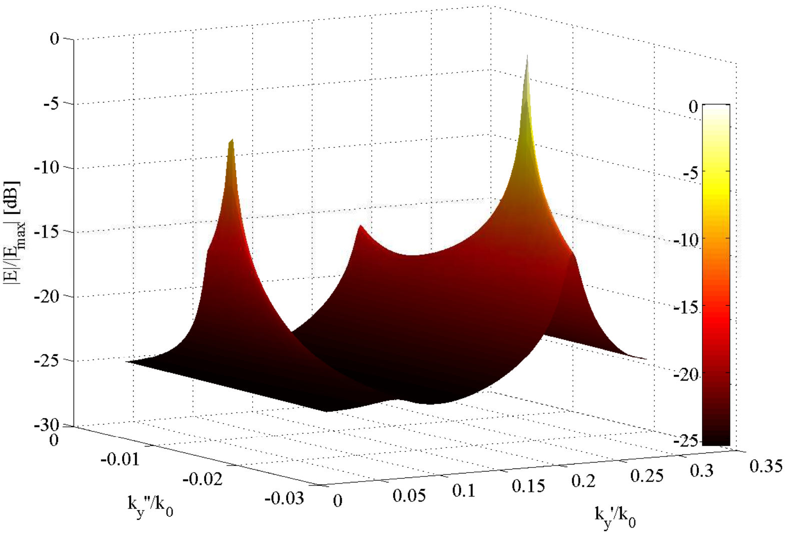

Figure 6.1: Magnitude of electric field at some observation point within the unit cell of a periodic structure at 11.4 GHz over the complex plane of wavenumber $k_{y00} = k'_y - jk''_y$ when attenuation is considered.

not change any more. The golden section search is to divide the searching range into two sections with the ratio of $r/(1-r)$, where $r = 0.61803$ and to locate the maximum in one of the two sections to narrow down the searching range, as shown in Fig. 6.3. The Brent's method switches between the inverse parabolic interpolation and the golden section search to make sure every step converges and prevent the iterations to bounce around in some nonconvergent limit cycle [Brent, 2002].

6.3 Powell's Quadratically Convergent Method in Multi-direction Searching

As already mentioned before, the eigenvalue determination of the resonator model can be considered as a multi-dimensional maximization of the chosen observable over the complex plane of $\boldsymbol{k}_{t00}$, where $\boldsymbol{k}_{t00} = k_{x00}\hat{x} + k_{y00}\hat{y}$, $k_{x00} = k'_x - jk''_x$ and $k_{y00} = k'_y - jk''_y$. To realize the multi-dimensional search efficiently, a set of N mutually conjugate directions u_i is set up firstly and then from one initial point P_0 we search along u_i for the maximum P_i and use it as the initial point for the next search along direction u_{i+1}. Repeat this step until the function stops increasing. Every time after all the N directions have been searched, $(2P_N - P_0)$ is evaluated as an extrapolated point and its observable value is compared to the observable values of P_0 and P_N and it is decided, whether a new average direction needs to be chosen. This can help the algorithm to take advantage

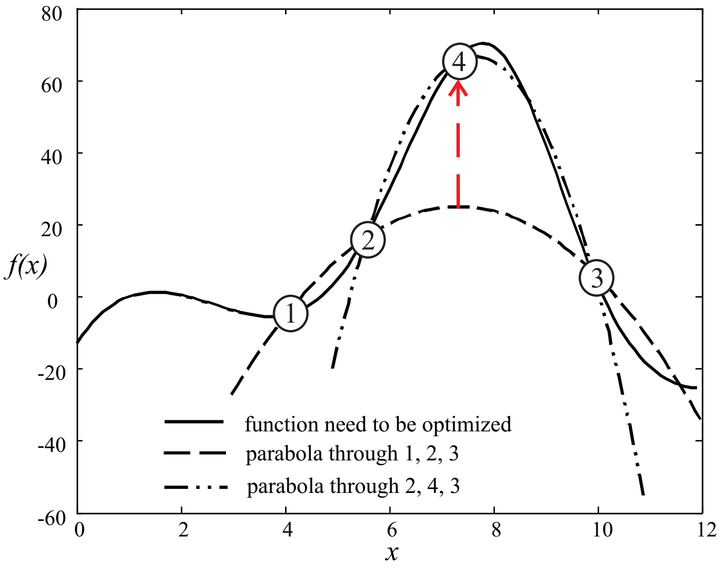

Figure 6.2: Inverse parabolic interpolation.

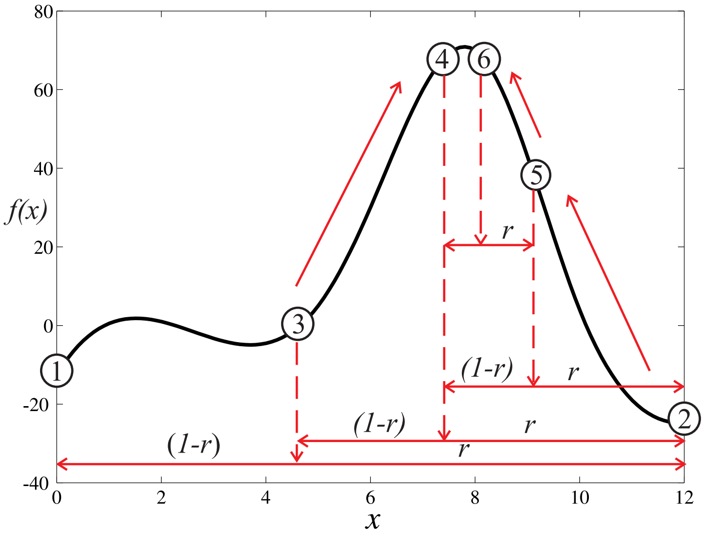

Figure 6.3: Golden section search.

of the direction with the largest increase as well as to keep the directions conjugate [Brent, 2002]. This acceleration method works well for local maximization where only one maximum happens according to the only one mode in a certain frequency range. However, sometimes there are more than one mode existing simultaneously in the same frequency range. Therefore, all the maxima must be located.

6.4 Global Optimization for Multi-mode Scenario

When there are more than one mode propagating in the operating frequency range, consequently there will be more than one maximum in the complex plane of wavenumber as shown in Fig. 6.1. In order to obtain the mode dispersion behavior of all the propagating modes, it requires to locate all the maxima which actually leads to a global optimization over the complex plane of the wavenumber.

Global Optimization: Problem and Classification of Algorithms

Many problems in engineering and science can be formulated as global optimization problems. The goal of the global optimization is to find the best possible elements x^* from a set $\mathbb{X}$ according to a set of criteria $F = f_1, f_2, \ldots, f_n$ [Weise, 2008]. These criteria are expressed as mathematical functions, the so-called objective functions. The objective functions in many practical applications are not convex which leads to multiple local and global extremal points in the region of interest. The determination of these local extrema can be one step in a procedure to find the global extrema. However, finding all these multiple extrema is a challenging computational problem. Unlike the local extrema, there is no practical and general criteria to determine whether a global extremum is found which makes the problem even worse. Therefore, the existing methods like deterministic and stochastic methods are basically searching the region of interest systematically due to the lack of the local criteria for the ascertaining global extrema. However, it is not computationally feasible to search exhaustively over a fine mesh unless the dimension of the parameter space is small. How to search it efficiently is the main challenge of these algorithms.

According to the method of operation, generally the optimization algorithms can be divided into two categories: deterministic and probabilistic algorithms. The deterministic algorithms are usually used in the problem where a clear relation between the characteristics of the possible solutions and their utility exists. The search space can be efficiently explored for example by divide and conquer scheme (D&C). When the relation between a solution candidate and its utilities in the given problem is not so obvious or too complicated, or the dimensionality of the search space is very high, the probabilistic algorithms are better choices. This class of algorithms trades the guaranteed correctness of the solution to a shorter runtime where the solution can not be guaranteed as a global optimum. Both algorithms use heuristics which are the functions helping to decide which one of a set of possible solutions to be examined next. The deterministic algorithms normally employ heuristics to define the processing order of the solution candidates. While the probabilistic algorithms tend to consider the selected elements by the heuristic of the search space in further computations. Most global optimization algorithms can be divided into two separate phases. One is the global phase where the exhaustive exploration of the search space is conducted. The other is the local phase, which exists in each iteration of the global phase and employs a local optimization procedure to identify a locally optimal point.

- Deterministic Algorithms
  An algorithm is deterministic if it can be simulated by a deterministic finite automaton, that is, a 5-tuple $(\sum, Q, q_0, F, \delta)$ where $\sum$ is the input alphabet, Q the set of states, $q_0 \in Q$ the start state, $F \subseteq Q$ the set of finial states, and $\delta : Q \times \sum \to Q$ is the transition function [Liberti, 2008]. The transition function produce the next state with the current state of the automaton and a word from the input alphabet. The well-defined function δ embodies the principle of determinism which can produce a unique next state to any pair of (current state, input word). When the next state is a subset of Q, which leads to more than one possible next states to any pair (current state, input word), the automaton is a nondeterministic finite automaton. However, any nondeterministic finite automaton can be simulated by a deterministic finite automaton. Computers are theoretically deterministic finite automata while they are instructed to perform certain steps. Therefore, the algorithms can run on the deterministic computers based on transition relations rather than functions. Both, the global phase and the local phase can be deterministic. The most famous and wildly used deterministic algorithms are

  - Branch-and-Select methods [Tuy, 1998]
    Branch-and-Select methods include branch-and-bound and branch-and-cut techniques. The branch-and-bound can be divided into two stages, one is splitting the problem space into subspaces and the other is calculating lower and/or upper bounds for the objective function value of the subspaces. The function value of the bounds are compared and the subspaces can be decided whether to be discarded or not. The brand-and-cut technique is a combination of the brand-and-bound techniques and the cutting plane method but its applications are restricted to integer linear problems. When the obtained possible solution contains a non-integer value for a variable which is supposed to be integer, the cutting plane method is employed to find further linear constraints that are satisfied by all feasible integer points.

  - Outer approximation method [Duran & Grossmann, 1986]
    The outer approximation method alternately solves a primal problem which is a nonlinear program with all the integer variables fixed in value and a relaxed master problem which is a mixed-integer linear program constructed by linearizing the objective function and the constraints around a solution point of the primal problem. At each iteration, the updated best primal solution provides a lower bound in the maximization case and the relaxed master problem gives an upper bound for the optimal solution. Then the next integer value can be determined. When the upper bound converges to the lower bound, the global optimum is obtained.

  - Methods based on algebraic geometry [Basu et al., 2006]
    Algebraic geometry is a combination of linear algebra, where the systems of linear equations with several variables are studied, and algebra where the

  polynomial equations with one variable are studied. The algebraic geometry helps to describe the geometric structure of the set of solutions for polynomial equation systems with several variables when the solutions can not be explicitly written down. This concept can be applied to find the global optimum of a system when the objective function can be expressed polynomially. Many applications can be found [Kavasseri, 2007], [Jibetean & de Klerk, 2006].

- Stochastic algorithms
  The stochastic algorithms deal with situations with a random element in the choice of the next step of computation. The deterministic automata e.g. computers need to simulate the random choices with pseudo-random number sequences or similar computational devices or employ a random external input for the true random data requirement. The stochastic algorithms work usually in global phase. Several Monte-Carlo-based algorithms exist:
  - Simulated annealing (SA) [Kirkpatrick et al., 1983], [Černý, 1985]
    The simulated annealing method is often used to locate a good approximation to the global optimum of a given function in a large search space. The method is inspired by the physical process of annealing in metallurgy which uses heating and cooling of a material to increase the size of its crystals to reduce their defects. Similar to the atoms' movement of escaping from the initial state and wandering randomly through states of higher energy when heating, SA replaces the current solution by a random solution. The new solution can be found by reducing a global parameter T and comparing the difference between the corresponding function values, similar as atoms tend to lower internal energy states when it is cooling.
  - Random optimization (RO) [Matyas, 1965], [Baba, 1981]
    Random optimization iteratively moves the solution to a better position in the search space which is sampled using for example a normal distribution around the current position. It does not employ the gradient of the problem to be optimized. Therefore, it can work with functions which are not continuous or differentiable.
  - Evolutionary Computation (EC)
    Evolutionary computation is a subfield of artificial intelligence that involves combinatorial optimization problems. It includes different algorithms e.g. evolutionary algorithms (EA) which are generic population-based metaheuristic optimization algorithms, a learning classifier system (LCS) which is with close link to reinforcement learning and genetic algorithms, evolutionary programming, evolution strategy (ES), or genetic programming (GP). EC uses iterative progress e.g. growth or development in a population which is then selected in a guided random search using parallel processing to achieve the desired end.
  - Methods based on Monte Carlo Sampling [Metropolis & Ulam, 1949]
    The Monte Carlo methods basically rely on repeated random sampling to compute their results. They are wildly used in simulating systems with many

coupled degrees of freedom, e.g. fluids, disordered materials, strongly coupled solids, and cellular structures or modeling the phenomena with significant uncertainty in inputs, e.g. the calculation of risk in business. The methods based on Monte Carlo sampling always follow some certain steps. First a domain of possible inputs must be defined. Then the inputs are generated randomly from a probability distribution over the domain and a deterministic computation is performed on the inputs. Finally the results are aggregated [Kalos & Whitlock, 2008].

- Parallel tempering [Swendsen & Wang, 1986], [Earl & Deem, 2005]
  The parallel tempering tries to improve the dynamic properties of the Monte Carlo method, also named as replica exchange Markov chain Monte Carlo (MCMC) sampling. A Monte Carlo simulation performs a single stochastic process to evaluate the energy of the system and decides whether to accept or reject the updates based on the temperature T. However, when the system is highly correlated the system can suffer from critical slowing down of convergence due to the high rejection of updates. The parallel tempering is to make the configurations at high temperatures, where the updates are comparatively more probable, also available to the simulations at low temperatures and vice versa. Therefore, the method can sample both low and high energy configurations and become very robust. The thermodynamical properties which are generally difficult to compute in the canonical ensemble can be computed precisely.
- Stochastic tunneling (STUN) [Hamacher, 2006], [Hamacher & Wenzel, 1999]
  The stochastic tunneling is also based on the Monte Carlo method. It is designed to avoid the slow dynamics of ill-shaped energy functions which might be encountered by Monte Carlo method when hopping randomly from the current solution vector to another one. Instead of sampling the objective function, the stochastic tunneling samples a transformed function that lacks the slow dynamics, whose standard form can be defined by the expectation of the difference between the optimal function value found so far and the next function value.

Combined Trajectory Methods for Global Optimization

In this work, the relation between the solution $(\omega, \boldsymbol{k})$ and the objective function e.g. the electromagnetic field is complicated but clear. Therefore the deterministic algorithms can be employed to find the multiple extrema over the complex plane of wavevector. The methods of finding the local extrema stated in chapter 6.2 and 6.3 can efficiently locate one stationary point in the region. However the difficulty lays on how can the searching scheme escape from one found stationary point and find the possible direction for the next one. [Yang & Beck, 1998] introduced a combination of two generalized trajectory methods for computation of multiple local extrema of an objective function. One trajectory method is a homotopy one which can find a stationary point of the objective function with global convergence. Then the second method, named a relaxation scheme, can systematically connect other stationary points in a region from a starting stationary point by a network of trajectories.

- Homotopy schemes
  The homotopy schemes are also named embedding, invariant embedding, and parameter continuation. The main idea of the homotopy schemes is to transform the target problem which is difficult to solve into a simpler problem by embedding the target problem and the simple one into a more general problem with a transition function called a homotopy. The transformation can be described by a homotopy parameter which can be changed continuously in order to evolve the simple solution into the target solution [Garcia & Gould, 1980], [Keller, 1987]. Different from local iterative methods, the homotopy schemes have the characteristics of global convergence, which means they do not require good initial guesses in order to converge. This feature makes the homotopy schemes good choices for highly nonlinear problems where good initial guesses are difficult to estimate. If $f(x)$ is considered as the objective function which needs to be solved, the stationary points of $f(x)$ satisfy the stationary condition

  $$\nabla f(x) = 0. \tag{6.4.1}$$

  Therefore, the problem of finding all the stationary points of $f(x)$ is actually the problem of finding all the roots of the set of equations in (6.4.1). The homotopy schemes try to embed (6.4.1) in a new set of equations

  $$g(x, \lambda) = 0, \quad \lambda \in R. \tag{6.4.2}$$

  Here $g(x, \lambda) \in R^n$ and all the roots of (6.4.1) also satisfy (6.4.2) for some particular value of λ. There are two main canonical homotopy schemes, Newton and fixed-point. In fixed-point homotopy, Eq. (6.4.2) is defined as

  $$g_F(x, \lambda) = (1-\lambda)M_f(x - x_0) + \lambda \nabla f(x) = 0, \tag{6.4.3}$$

  where x_0 is a fixed arbitrary point in the search region and M_F is a nonsingular $n \times n$ matrix. The homotopy trajectory is traced by varying λ from 0 to 1. When $\lambda = 0$, Eq. (6.4.3) is turned into the simple problem with only one solution $x = x_0$. When $\lambda = 1$, Eq. (6.4.3) is the original problem. In Newton homotopy, the derivative of the objective is required and Eq. 6.4.2 is rewritten as,

  $$g_N(x, \lambda) = (1-\lambda)(\nabla f(x) - \nabla f(x_0)) + \lambda \nabla f(x) = 0. \tag{6.4.4}$$

- Relaxation schemes
  After finding one stationary point by using the homotopy scheme, the relaxation schemes can be employed to determine the other stationary points in the searching space. The idea is to use a special form of Eq. (6.4.2) as simple as possible which requires the information of one stationary point. One example can be expressed as

  $$g_R(x, \lambda) = \nabla f(x) - (1-\lambda)v = 0, \tag{6.4.5}$$

where v is a given normalized constant vector in R^n. The stationary points satisfying Eq. (6.4.1) will also satisfy $g_R(x, 1) = 0$. Therefore, for an arbitrary v, the relaxation schemes can trace g_R for λ starting from 1. When relaxation trajectories pass through $\lambda = 1$, another stationary point is found. To increase the chance of finding all the stationary points, a network of relaxation trajectories can be set up to perform multiple relaxation schemes systematically. The vector v can be chosen to be one vector inside a set of orthonormal basis vectors $\{e_1, e_2, \ldots, e_n\}$. When v equals to e_i, the ith constraint in Eq. (6.4.1) is released while the other constraints remain enforced. Therefore, the different constraints can be set relaxed in turn by varying v to each of the basis vectors.

7 Mode Selection

In this chapter, mode selection in the driven method will be discussed. As we know, there might be more than one mode propagating in the operating frequency range. For analysis, it would be useful and important to select the specific mode which is of interest. There are two aspects for the mode selection, one is to stimulate a certain mode by the provided excitation and the other is to distinguish different modes from each other when several modes exist in mode dispersion analysis.

7.1 Mode Excitation

In principle, with appropriately arranged electric and magnetic current sources with different polarization or distributions inside the solution domain, all the relevant modes can be excited. Since the electric and magnetic fields of one mode will not be exactly zero at identical locations. Additionally, current density excitation has the advantage that it can be designed to select a desired eigenmode. The experience from the excitation of cavity resonators, e.g. external and internal excitations, can be used as a source of reference.

7.1.1 External Excitation of Cavity Resonator

For a cavity resonator there are several methods to couple the external energy into the resonator or the other way around [Bahl & Bhartia, 2003], [Russer, 2006], [Guru & Hiziroğlu, 2004]. As shown in Fig. 7.1, inductive coupling by a current loop, capacitive coupling by an electric pole and aperture coupling or the combination of different coupling techniques can all realize the energy interchange between the resonators and the external region.

- Current Loop (inductive coupling)
  The plane of the current loop is placed perpendicular to the direction of the magnetic field in the cavity.
- Electric Probe (capacitive coupling)
  The probe is placed parallel to the direction of the electric field in the cavity.
- Aperture
  A open aperture between the cavity and the input waveguide can make the direction of a field component in the cavity the same as the one in the waveguide.

For a particular mode in a cavity, the excitation can be accomplished either by coupling the electric field by an electric probe, or by coupling the magnetic field by a current

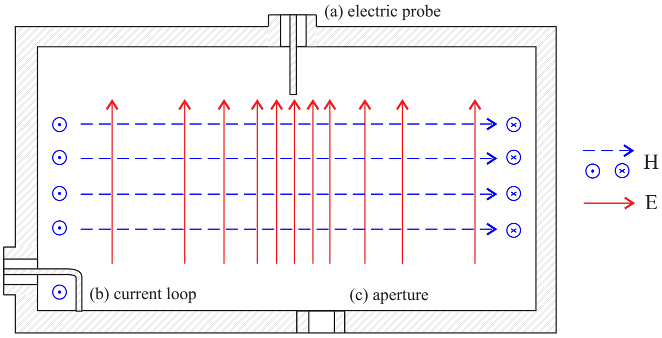

Figure 7.1: Resonator coupling methods. (a) electric probe: parallel to the E-field, (b) current loop: perpendicular to the H-field, (c) aperture.

loop, at the location where the corresponding field component in the cavity is supposed to be the highest. For example considering a rectangular waveguide resonator shown in Fig. 7.1, the TE_{10} mode can be stimulated.

7.1.2 Internal Excitation of Cavity Resonator

The modes in a cavity consist of both irrotational and solenoidal modes [Kurokawa, 1958], [Collin, 1991]. The electric field $\boldsymbol{E}$ can be expanded in terms of solenoidal modes $\boldsymbol{E}_n$ and irrotational modes $\boldsymbol{F}_n$ in form of

$$\boldsymbol{E} = \sum_n (A_n \boldsymbol{E}_n + B_n \boldsymbol{F}_n). \tag{7.1.1}$$

Here the solenoidal modes $\boldsymbol{E}_n$ are the solutions of the equations

$$\begin{aligned} (-\nabla \times \nabla \times + k_n^2)\boldsymbol{E}_n = (\nabla^2 + k_n^2)\boldsymbol{E}_n &= 0, && (7.1.2)\\ \nabla \cdot \boldsymbol{E}_n &= 0, && (7.1.3)\\ \boldsymbol{n} \cdot \boldsymbol{E}_n &= 0, \quad \text{on } S, && (7.1.4) \end{aligned}$$

and the irrotational modes $\boldsymbol{F}_n$ are the solutions of

$$\begin{aligned} (\nabla^2 + l_n^2)\boldsymbol{F}_n &= 0, && (7.1.5)\\ \nabla \times \boldsymbol{F}_n &= 0, && (7.1.6)\\ \boldsymbol{n} \times \boldsymbol{F}_n &= 0, \quad \text{on } S, && (7.1.7) \end{aligned}$$

where S is the closed surface of a volume V. When there is a current $\boldsymbol{J}(\boldsymbol{r})$ in the cavity, the electric field due to the current is a solution of

$$\nabla \times \nabla \times \boldsymbol{E} - k_0^2 \boldsymbol{E} = -j\omega\mu_0 \boldsymbol{J}. \tag{7.1.8}$$

With the expansion shown in Eq. (7.1.1), the differential equation (7.1.8) can be rewritten as

$$\sum_n [(k_n^2 - k_0^2)A_n \boldsymbol{E}_n - k_0^2 B_n \boldsymbol{F}_n] = -j\omega\mu_0 \boldsymbol{J}. \tag{7.1.9}$$

Scalar multiply Eq. (7.1.9) by $\boldsymbol{E}_n$ and $\boldsymbol{F}_n$ in turn and integrate over the volume V to obtain

$$(k_n^2 - k_0^2)A_n = -j\omega\mu_0 \iiint_V \boldsymbol{E}_n(\boldsymbol{r}') \cdot \boldsymbol{J}(\boldsymbol{r}') dV', \tag{7.1.10}$$

$$-k_0^2 B_n = -j\omega\mu_0 \iiint_V \boldsymbol{F}_n(\boldsymbol{r}') \cdot \boldsymbol{J}(\boldsymbol{r}') dV'. \tag{7.1.11}$$

Insert Eq. (7.1.10) and (7.1.11) back into Eq. (7.1.1) to obtain the solution for $\boldsymbol{E}$

$$\boldsymbol{E}(\boldsymbol{r}) = -j\omega\mu_0 \iiint_V \sum_n \left[\frac{\boldsymbol{E}_n(\boldsymbol{r})\boldsymbol{E}_n(\boldsymbol{r}')}{k_n^2 - k_0^2} - \frac{\boldsymbol{F}_n(\boldsymbol{r})\boldsymbol{F}_n(\boldsymbol{r}')}{k_0^2} \right] \cdot \boldsymbol{J}(\boldsymbol{r}') dV', \tag{7.1.12}$$

where

$$\bar{\boldsymbol{G}}_e(\boldsymbol{r}, \boldsymbol{r}') = \sum_n \left[\frac{\boldsymbol{E}_n(\boldsymbol{r})\boldsymbol{E}_n(\boldsymbol{r}')}{k_n^2 - k_0^2} - \frac{\boldsymbol{F}_n(\boldsymbol{r})\boldsymbol{F}_n(\boldsymbol{r}')}{k_0^2} \right] \tag{7.1.13}$$

is the dyadic Green's function for the electric field in the cavity. From Eq. (7.1.12) we can see that the field modes, which have the field components sharing the same direction with the current excitation, can be excited. Therefore, a particular mode can be selected. In [Russer, 2006], the frequency, where the system is operated, is also proved to influence the efficiency of the mode excitation. The closer the operation frequency to the resonance frequency of a certain mode, the better the mode can be excited. With current density excitation, in principle all the modes can be stimulated while as well some particular mode can be selected by some carefully designed current density excitation.

7.2 Mode Distinction

In many occasions the structure under analysis can work with several modes in the operating frequency range. For dispersion analysis which is mainly concerning with mode dispersion as mentioned in section 4.6.4, it is crucial to distinguish between different modes. Different from the waveguide discussed in section 4.6, resonators can be considered as waveguides with certain length p in wave propagation direction which enforces the wavenumber to satisfy an integer multiple of π phase shift in wave propagation direction. Take a rectangular waveguide resonator as an example. Fig. 7.2 depicts its geometry dimension.

The cutoff wavenumber of the waveguide mode is

$$k_{cmn} = \sqrt{(\frac{m\pi}{a})^2 + (\frac{n\pi}{b})^2}, \quad m, n = 0, 1, 2, \ldots. \tag{7.2.1}$$

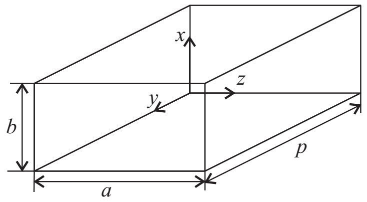

Figure 7.2: Rectangular waveguide cavity resonator.

Therefore, the resonant wavenumber can be expressed as

$$k_{mnl} = \sqrt{(\frac{m\pi}{a})^2 + (\frac{n\pi}{b})^2 + (\frac{l\pi}{p})^2}, \quad m, n, l = 0, 1, 2, \ldots. \tag{7.2.2}$$

In Eq. (7.2.2) the component $(\frac{l\pi}{p})^2$ is actually the propagation constant β^2 in the waveguide as Eq. (4.5.14). In a periodic structure, p is the length of one unit cell. With the assumption of infinite length of the whole configuration, the periodic structure can also be considered as a waveguide configuration. $(\frac{l\pi}{p})^2$ defines the phase shift between the periodic boundaries in wave propagation direction. Consequently, the cutoff wavenumber k_{cmn} as the eigenvalue according to a specific eigenmode and the field distribution on the cross section of the wave propagation direction can be used to distinguish different modes. Especially for degenerate modes which share the same cutoff wavenumber k_{cmn}, the field distribution which must be orthogonal between different modes can be used to distinguish the modes, as shown in Fig. 4.7. Some examples of mode distinction are given in chapter 8.

8 Applications

8.1 Classical Rectangular Waveguide: A Verification Example for Small Attenuation Scenarios

In this section, a classical rectangular waveguide, whose propagation constant and attenuation constant can be calculated analytically, is considered to verify the driven eigenproblem computation in small attenuation scenarios.

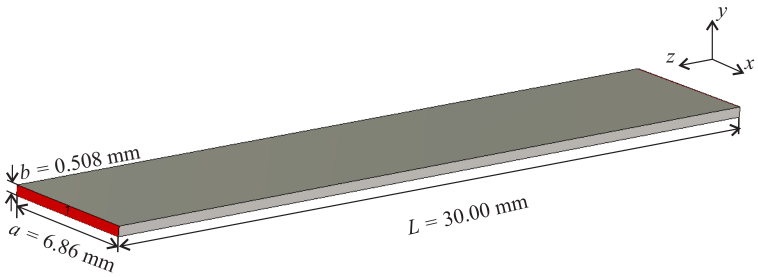

Figure 8.1: Configuration of the rectangular waveguide with a length of 30.0 mm.

Model Setup

A rectangular waveguide with a cross section of $a = 6.86$ mm, $b = 0.508$ mm, and with length of $L = 30.0$ mm is filled with dielectric material of $\varepsilon_r = 2.33$ and $\tan\delta = 0.0012$ as depicted in Fig. 8.1. This kind of a classical rectangular waveguide can be modeled analytically. In [Pozar, 2004], the wavenumber, the cutoff wavenumber, the propagation constant and the attenuation constant for TE and TM modes in rectangular waveguides are summarized, which are listed in Tab. 8.1. Here, k is the wavenumber of the material filling of the waveguide. k_c is the cutoff wavenumber of the TE_{mn} or TM_{mn} modes and β is the propagation constant. In rectangular waveguides, which are closed, there are no radiation losses but dielectric and conductive losses may exist. If the metal is assumed ideal, conductive losses are null and only dielectric losses according to α_d are considered. With the geometrical dimension of the rectangular waveguide, the dispersion and attenuation curve can be directly plotted. CST MWS also provides some convenient numerical solvers to model the rectangular waveguide. Two waveguide ports can be set at the two ends of the rectangular waveguide in wave propagation direction in the CST MWS transient solver. The dispersion and attenuation behaviors can be obtained by monitoring the S-parameters over the ports.

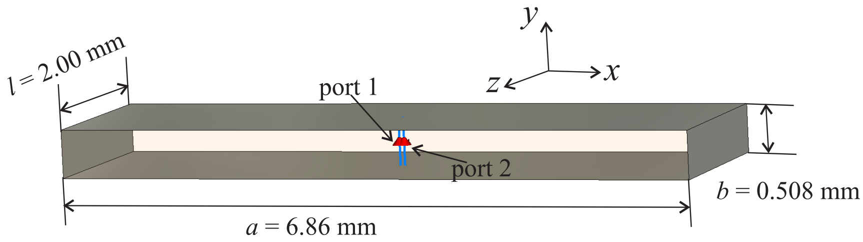

Figure 8.2: Configuration of the unit cell of the rectangular waveguide with a length of 2.00 mm.

Quantity	TE_{mn} Mode	TM_{mn} Mode
k	$\omega\sqrt{\mu\varepsilon}$	$\omega\sqrt{\mu\varepsilon}$
k_c	$\sqrt{(m\pi/a)^2+(n\pi/b)^2}$	$\sqrt{(m\pi/a)^2+(n\pi/b)^2}$
β	$\sqrt{k^2-k_c^2}$	$\sqrt{k^2-k_c^2}$
α_d	$\frac{k^2\tan\delta}{2\beta}$	$\frac{k^2\tan\delta}{2\beta}$

Table 8.1: Propagation constant and attenuation constant for TE and TM modes in rectangular waveguides.

The rectangular waveguide with the same configuration but modeled as a unit cell with a length of $l = 2.00$ mm is analyzed with the driven eigenproblem computation method. For a closed waveguide without radiation losses there are only conductive and dielectric losses both of which are small. Therefore, the perturbation method can be employed to analyze the attenuation in the rectangular waveguide. As mentioned in section 2.2, the driven eigenproblem computation is implemented in the CST MWS frequency domain solver. The unit cell of the rectangular waveguide is discretized with a tetrahedral mesh and two discrete ports are placed in the center of it to stimulate and monitor the field, respectively, as shown in Fig. 8.2. The two ports are placed next to each other in order to make sure they observe the same field inside the structure.

Dispersion and Attenuation Analysis

Fig. 8.3 indicates the perfect agreement among the results from the unit cell employing the driven method and that from the long length rectangular waveguide using the transient solver in CST MWS and the analytical method, in both the propagation constant and the attenuation constant. The blue lines are the dispersion curve which match to each other perfectly among the three methods. The black lines indicate the dielectric loss of the rectangular waveguide which also show great agreement among the results from the three methods.

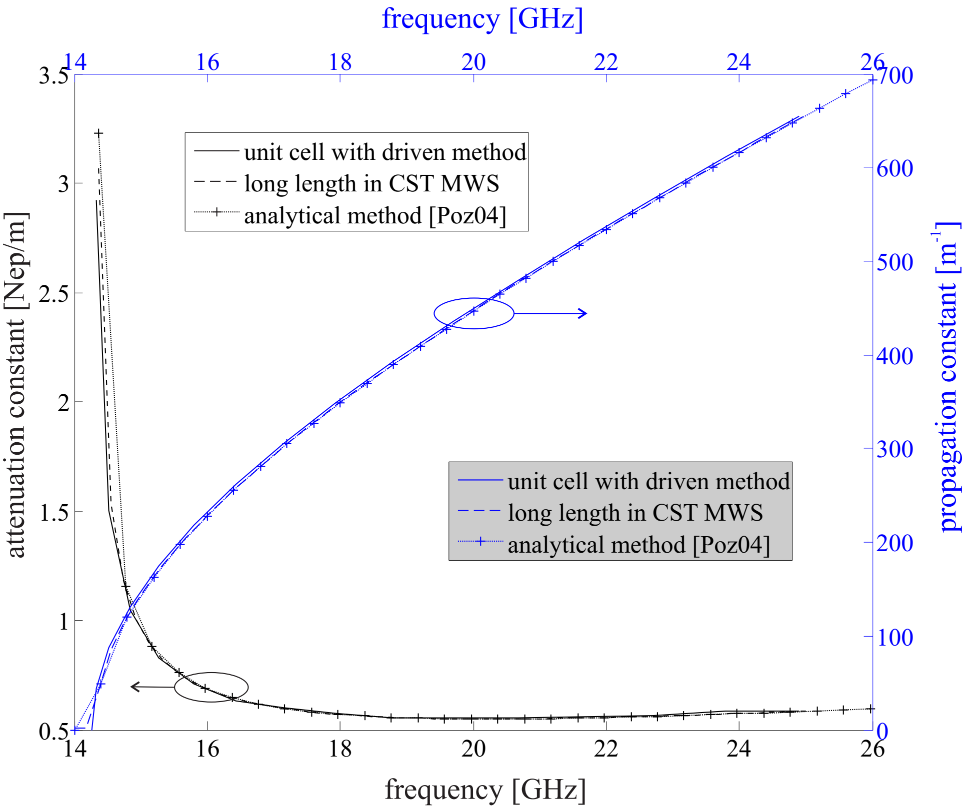

Figure 8.3: Propagation and attenuation constants of the rectangular waveguide in Fig. 8.1 compared by results from the analytical method, from CST MWS and from the driven method.

8.2 Substrate Integrated Waveguide (SIW): Small Radiation Example

Model Setup

An SIW structure as depicted in Fig. 3.7 with geometry parameters $d = 0.8$ mm, $s = 2.0$ mm, $w = 7.2$ mm, $h = 0.508$ mm and filled with a dielectric material of $\varepsilon_r = 2.33$ and $\tan\delta = 0.0012$ is analyzed. The SIW is designed to work at $14 - 26$ GHz. The bilateral gap s is smaller than $\lambda_0\sqrt{\varepsilon_r}/2$, which means the radiation losses from the gap would be quite small. This makes the SIW a good example for small radiation and can be analyzed with the driven method with port excitation mentioned in section 5.2. The unit cell depicted in Fig. 8.4(a) is modeled with the driven method in the frequency solver of CST MWS.

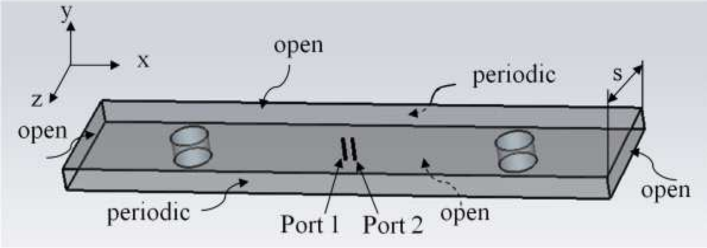

(a) unit cell of SIW with discrete ports in the center.

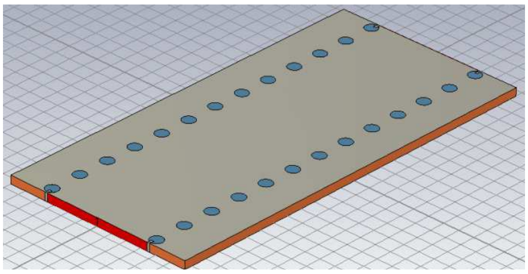

(b) SIW with 14 unit cells with waveguide ports at both ends.

Figure 8.4: Geometrical configuration of SIWs. (a) Unit cell of SIW with discrete ports. (b) SIW with 14 unit cells with waveguide ports at both ends in CST MWS

Two discrete ports are set in the center of the unit cell to stimulate the structure and monitor the resonance behavior, respectively. The periodic boundaries with some phase shifts are employed in wave propagation direction. By sweeping the frequencies, the resonance frequencies can be found for certain phase shifts between the periodic boundaries. The pairs of phase shifts and resonance frequencies form the dispersion curve over a frequency range. The perturbation method is employed for the attenuation analysis. The reference example is an SIW structure with basically the same geometrical parameters but a longer length of 28 mm depicted in Fig. 8.4(b), which equals to 14 unit cells. The reference example is analyzed with the transient solver of CST MWS with the waveguide ports at both ends. Then, the S-parameter between the two ports are obtained to perform the dispersion and attenuation analysis.

Dispersion and Attenuation Analysis

In the driven method with the discrete ports inside the unit cell, the fundamental mode of the resonator can be stimulated. By monitoring the scattering parameters, the resonance frequency for a certain phase shift between the periodic boundaries, which is always accompanied with a maximum or a minimum of the scattering matrix, can be found as shown in Fig. 8.5. It is apparent that $|S_{11}|^2 + |S_{21}|^2 \neq 1$, which means there are some losses present in the unit cell resonator. Sweeping the phase difference between the periodic boundaries, the corresponding ω_{res} can be found to form the dispersion curve as mentioned in section 5.2 as Eq. (5.2.1). As depicted in Fig. 8.6, for each phase difference $\Delta\varphi$ there is only one corresponding resonance frequency ω_{res} which means there is no higher mode except the fundamental mode TE_{10} in the operation frequency range.

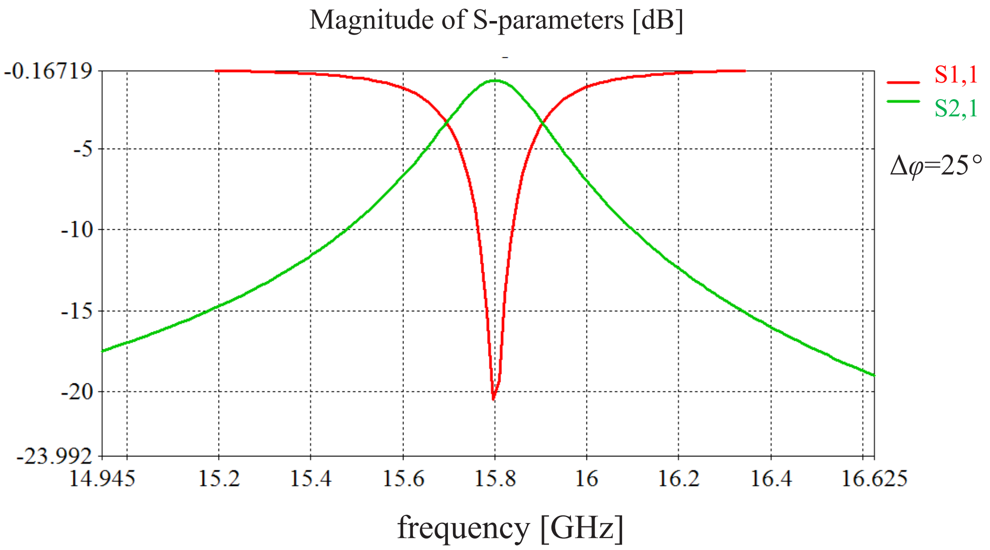

Figure 8.5: The scattering parameters of the unit cell depicted in Fig. 8.4(a) with the phase shift $\Delta\varphi = 25°$.

The dispersion curve obtained by the driven method with the unit cell agrees excellently with the results from CST MWS for the longer SIW as shown in Fig. 8.4(b). The attenuation constants from the two methods agree with each other also quite well with a trivial deviation which can be reduced by increasing the accuracy of the integration of the observable in the perturbation method.

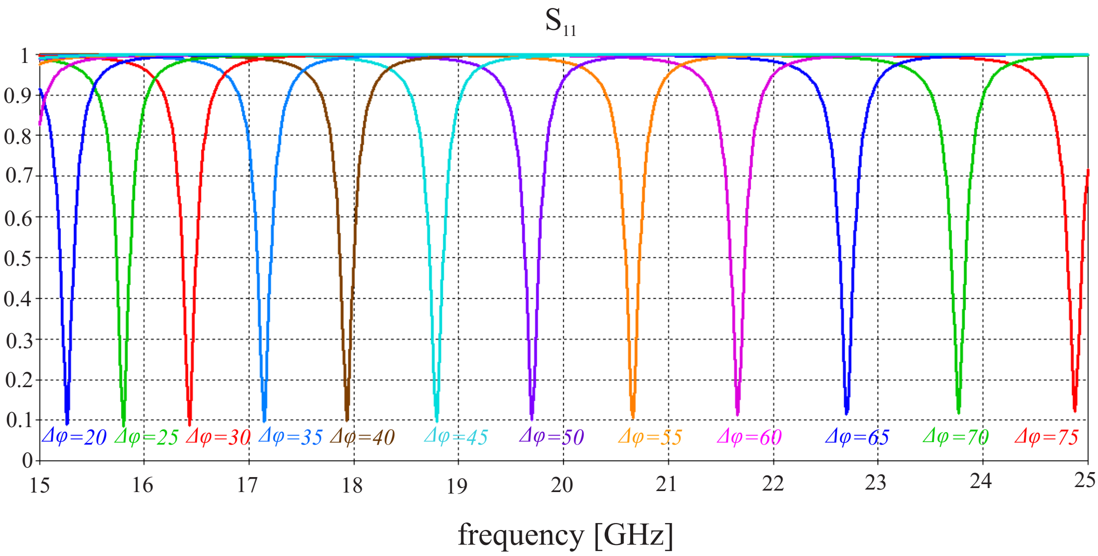

Figure 8.6: Sweeping the phase difference $\Delta\varphi$ to get corresponding resonance frequencies ω_{res} for the SIW unit cell depicted in Fig. 8.4(a).

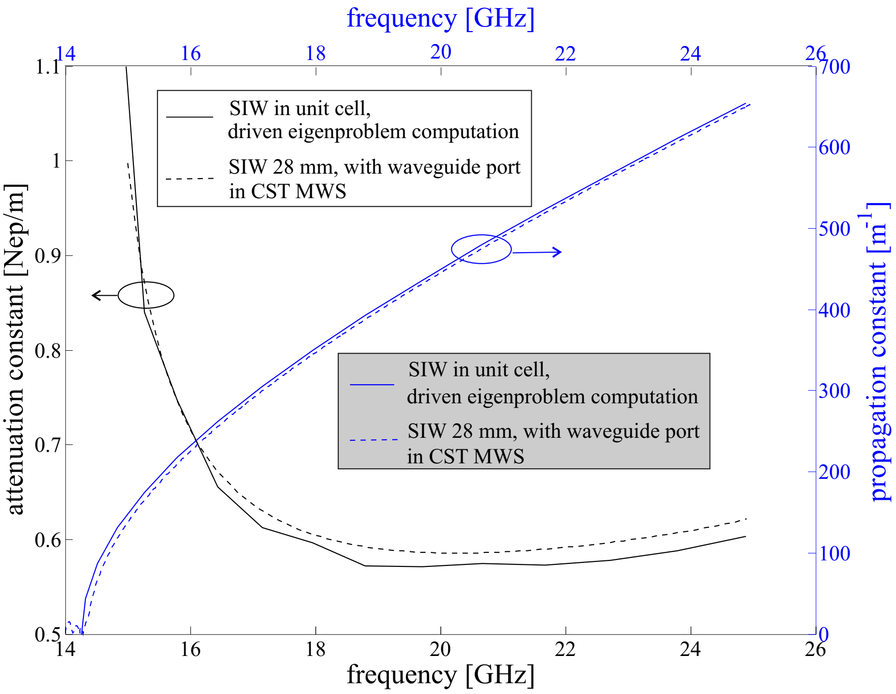

Figure 8.7: Propagation and attenuation constant of the fundamental mode in a SIW in Fig. 8.4 computed with driven method and compared with a SIW of length of 28 mm with waveguide ports in CST MWS

8.3 CRLH Leaky Wave Antenna: Interdigital Design Analysis

Model Setup

Here a composite right-/left-handed leaky-wave antenna (CRLH LWA) based on a SIW structure [Weitsch & Eibert, 2010] as depicted in Fig. 8.8 is analyzed by the driven method. The leaky-wave antenna is composed of the unit cell shown in Fig. 8.9 which is realized on a single-layer printed circuit board (PCB) with a 1.524 mm thick dielectric substrate Rogers RO4003 of $\varepsilon_r = 3.38$ and $\tan\delta = 0.0027$. The top copper plate is periodically slotted in an interdigital manner in order to obtain some specific capacitance. The two rows of "teeth" which interdigitate into each other introduce a capacitive gap between them. The slots are terminated by two lateral rows of vias and generate an additional shunt inductance by allowing extra transverse currents.

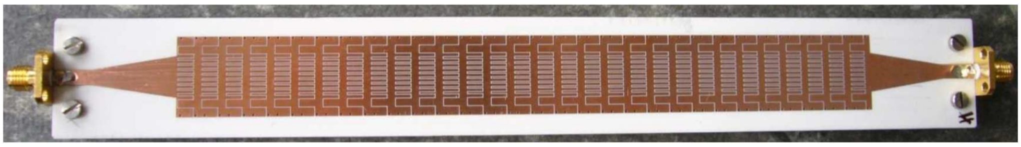

Figure 8.8: Fabricated CRLH leaky-wave antenna [Weitsch & Eibert, 2010].

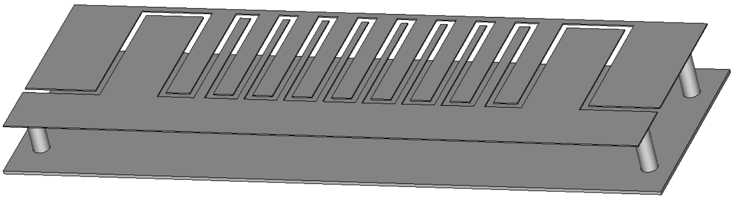

Figure 8.9: A unit cell of the CRLH LWA with a periodic length of 5.9 mm [Weitsch & Eibert, 2010].

Dispersion and Attenuation Analysis

Modeling this kind of structure, which has much finer details, e.g. the slot in this example, compared to the length of the structure will lead to an extremely large number of mesh cells and an extremely long simulation time if the whole structure is discretized and analyzed. For example modeling a CRLH LWA with 88.5 mm, which consists of 15 unit cells, in the frequency domain solver of CST MWS will generate over $1,000,000$ mesh cells and 2 hours simulation time with a 12-core CPU. However, by employing the driven method in CST with discrete ports, only one unit cell with 5.9 mm length will be considered and modeled. This can reduce more than 90% mesh cell and around 75%

simulation time. In this CRLH LWA, besides the conductive and dielectric losses there are also radiation losses. However, the losses are still low which can be analyzed by the perturbation method. Fig. 8.10 depicts the dispersion curves of the CRLH LWA, where the results from the driven method, and scattering matrix approach (SMA) as well as matrix-pencil (MP) method [Weitsch & Eibert, 2010] are compared.

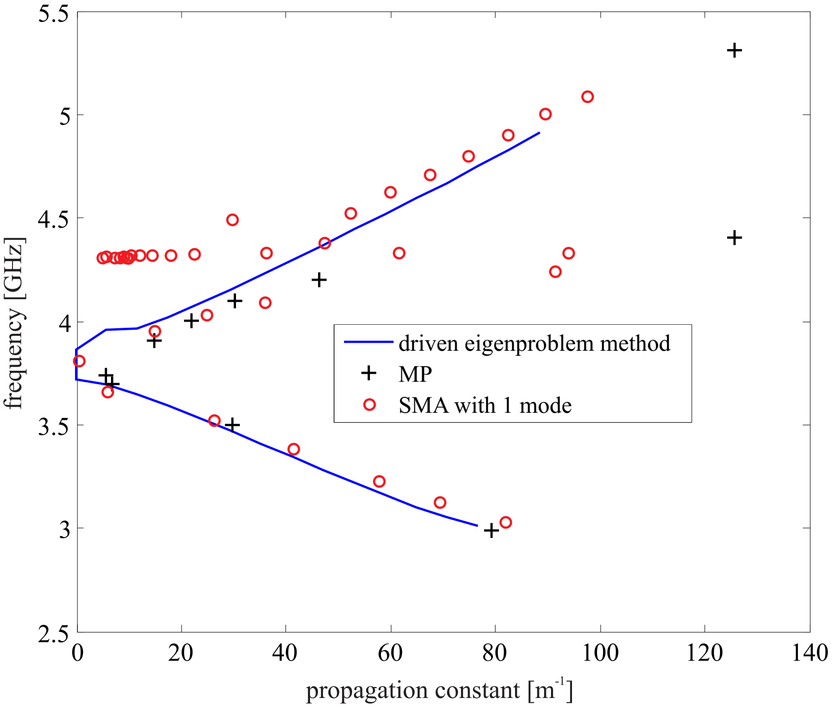

Figure 8.10: Propagation constant of the CRLH leaky-wave antenna from driven eigenproblem method, Matrix-Pencil (MP), and scattering matrix approach (SMA) [Weitsch & Eibert, 2010].

In Fig. 8.10, a good agreement can be observed among the three sets of data from driven method, SMA, and MP. The results from the driven eigenproblem computation in blue shows a bandgap between the left- and right-handed phase constant, which locates between 3.73 GHz and 3.86 GHz. However, the SMA method does not detect the bandgap between the LH and RH which might be caused by the limited mode number considered in the port as mentioned in section 4.3. The driven method can also avoid the blur in the SMA method around 4.3 GHz which is caused by the cutoff frequency of the H_{10}-rectangular waveguide mode.

Fig. 8.11 indicates a satisfying agreement between the driven method and measurements. Some deviations are due to the fabrication and material tolerance like the underetching and material inaccuracies. Since the perturbation method is only valid for propa-

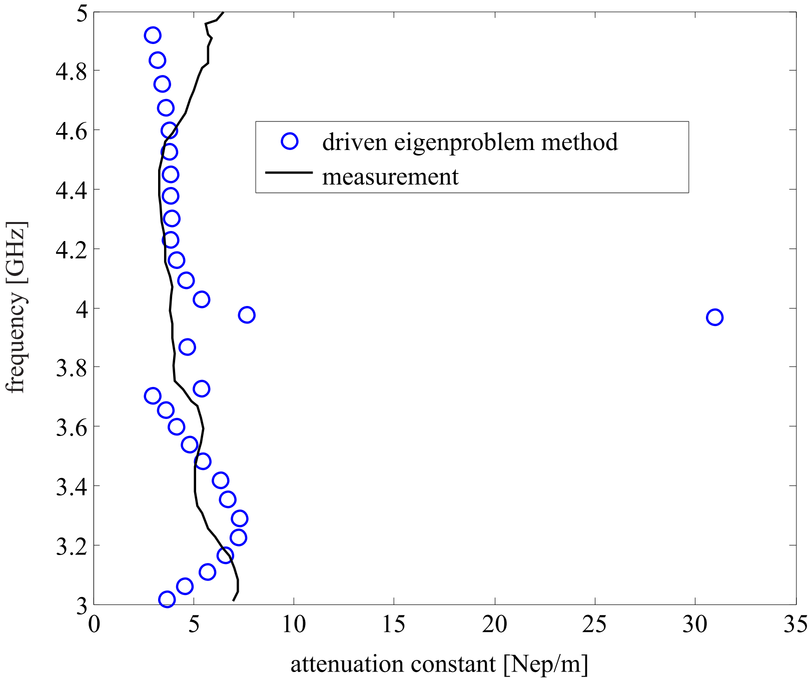

Figure 8.11: Propagation constant of the CRLH leaky-wave antenna from driven eigenproblem method, Matrix-Pencil (MP), and scattering matrix approach (SMA) [Weitsch & Eibert, 2010].

gating waves with relatively small attenuation, it is not possible to compute the attenuation constant in the bandgap between 3.73 GHz and 3.86 GHz with this approach in CST MWS. Therefore, there are deviations between the driven method and the measurement around the bandgap frequency. This problem can, however, be solved by using the FEBI implementation where the complex phase shift can be taken into account on the periodic boundary condition. When the evanescent and leaky modes can be described on the boundaries, the attenuation behavior inside the bandgap can be directly calculated.

8.4 Periodic Modulated Grounded Dielectric Corrugated Leaky Wave Antenna: Multi-mode Analysis

8.4.1 Model in 1D Periodic

The periodic modulated grounded dielectric corrugated slab works as an example to verify the FEBI implementation of the driven eigenproblem method. The acceleration methods mentioned in chapter 6 will be employed to achieve faster convergence in the iteration steps. The periodically modulated grounded dielectric slab is a conventional waveguide functioning as a leaky waveguide, which exhibits metamaterial-like behavior on higher space harmonics. With finite width, it has more than one propagation modes in the operating frequency range and it is analyzed to demonstrate the capability of the driven method in mode selection.

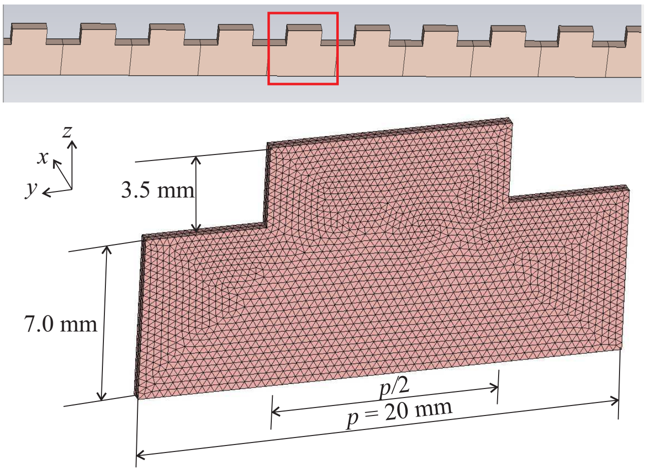

Figure 8.12: The dielectric corrugated leaky-wave antenna with infinite width along the x-axis and its unit cell.

Model Setup

Fig. 8.12 depicts the geometrical configuration of the corrugated dielectric slab working as a leaky wave antenna and the corresponding unit cell. The antenna is designed according to the design rule in [Schwering & Peng, 1983] with dielectric substrate Rogers TMM4 with relative permittivity $\varepsilon_r = 4.5$ and $\tan\delta = 0.002$ for operation in the frequency range $8-14$ GHz. Only the wavevector along the coordinate perpendicular to the grooves, here the y-axis, is considered. The antenna structure and the source distribution are assumed uniform in the coordinate parallel to the grooves, i.e. $k_x = 0$. The unit cell is discretized in tetrahedra. An impressed volume current density with x-component is applied in some of the tetrahedra as an excitation for TE-modes and the monitored quantity for finding the resonance peak is the electric field in several observation points inside the unit cell.

Dispersion and Attenuation Analysis

Fig. 8.13 depicts the reference model using the SMA approach as mentioned in section 4.4. The unit cell of the LWA is covered by 6-layer absorbing material with gradually increasing thickness and electromagnetic losses to the top in order to reduce the reflection for the impinging waves. At each port, 8 modes are considered for the modal expansion. Fig. 8.14 demonstrates the comparison of dispersion behaviors between the results from the driven method and the results with SMA technique. The light line separates the radiating waves from the purely guided waves. A perfect agreement between the two methods has been reached. Fig. 8.15 depicts the attenuation behavior of the structure, again the results from the driven method are compared to SMA technique. Some deviations are visible, which can probably be attributed to the different discretization models of the different approaches as well as the limited distance between the absorber and the antenna and the limited number of modes considered at each port in SMA. Increasing the number of the modes considered at each port in SMA, can reduce the deviation as shown in Fig. 8.15. SMA with 8 modes got closer results with the driven method than the one with 6 modes. However, it will at the same time increase the simulation time with SMA.

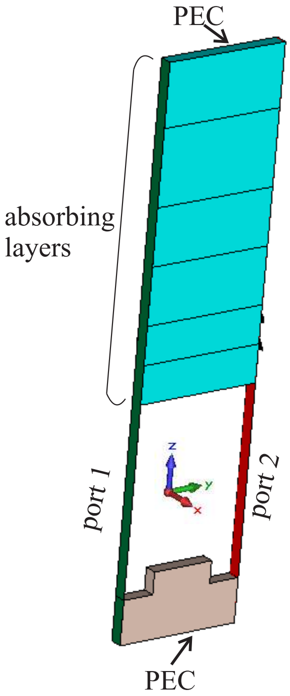

Figure 8.13: The simulation model in CST MWS for the grounded dielectric corrugated slab with absorbing layers and 8 modes at each port according to section 4.3.

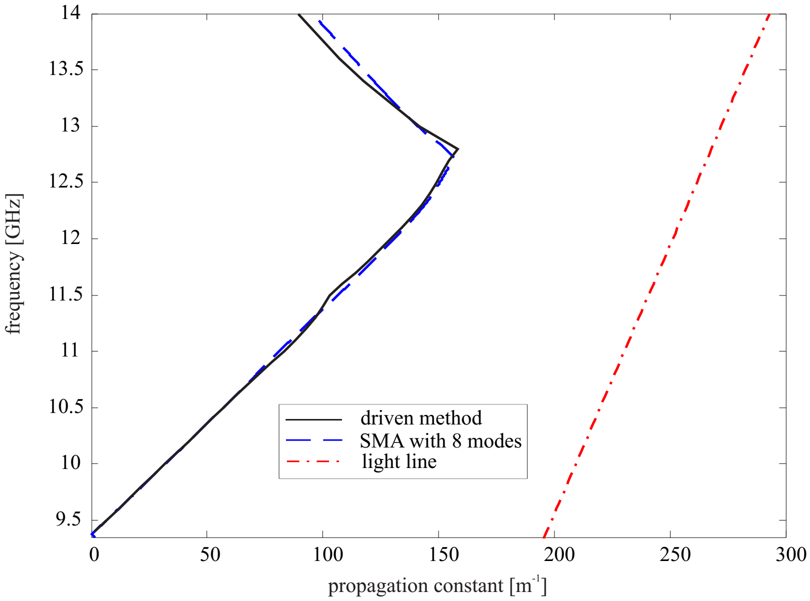

Figure 8.14: Dispersion diagram of the unit cell according to Fig. 8.12 compared to SMA results with 8 modes.

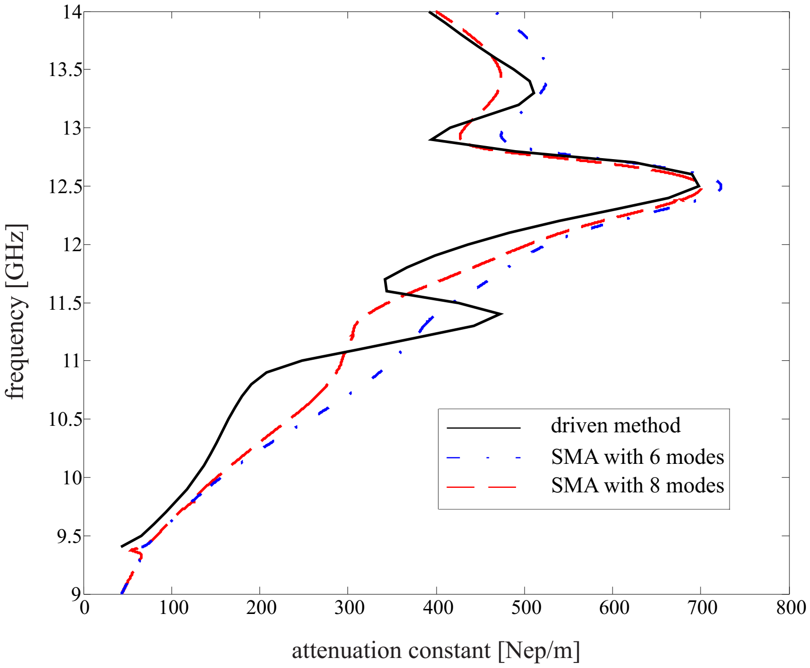

Figure 8.15: Attenuation constant of the unit cell according to Fig. 8.12 compared to SMA results with 6 and 8 modes at ports respectively.

Computational Efficiency Comparison

Tab. 8.2 demonstrates the computation time comparison between the driven method and the SMA with 8 modes at each port for the unit cell depicted in Fig. 8.12. The driven method which is implemented in FEBI and the SMA approach realized with the frequency domain solver in CST MWS are performed both on the same computer with the system configuration of Intel Core i7 CPU with 2.66 GHz and 12.0 GB RAM. For similar accuracy, SMA has to employ quite a thick air layer along the z-axis between the top of the unit cell and the bottom of the absorbing layers, which needs to be more than 5 times higher than the height of the unit cell. The air layer also requires a volume mesh. This leads to 8 times more mesh cells in SMA than the driven method which with FEBI employs the Green's function and boundary integral for the open boundary and the scattering field. Additionally, the SMA requires 8 modes at each port and generates a relatively large scattering matrix which can also cause computation time increase. The computation time for the driven method is an average among several frequencies. In this comparison, the driven method reveals a considerable advantage in both the number of mesh cell and the computation time with similar accuracy. The driven method reduced the number of mesh cells up to 87% and the computation time by 66%.

	the driven method	SMA
number of mesh cells	50,063 (1^{st} order tetrahedral)	397,567 (2^{nd} order tetrahedral)
computation time per frequency [s]	961.1	2692

Table 8.2: Computation time comparison between the driven method and SMA with 8 modes for the unit cell depicted in Fig. 8.12.

Convergence with Acceleration Method

As mentioned in chapter 6, some methods like Brent's and Powell's methods are employed to accelerate the convergence of the iteration in the eigenvalue searching. Fig. 8.16 demonstrates the convergence of the driven method based on FEBI with Brent's method acceleration for modeling the unit cell in Fig. 8.12. In both right- and left-handed regions, the iterations reach the satisfying convergence pretty fast. Comparing to the linear searching scheme, the Brent's method provides parabolic convergence which reduces the iteration steps greatly.

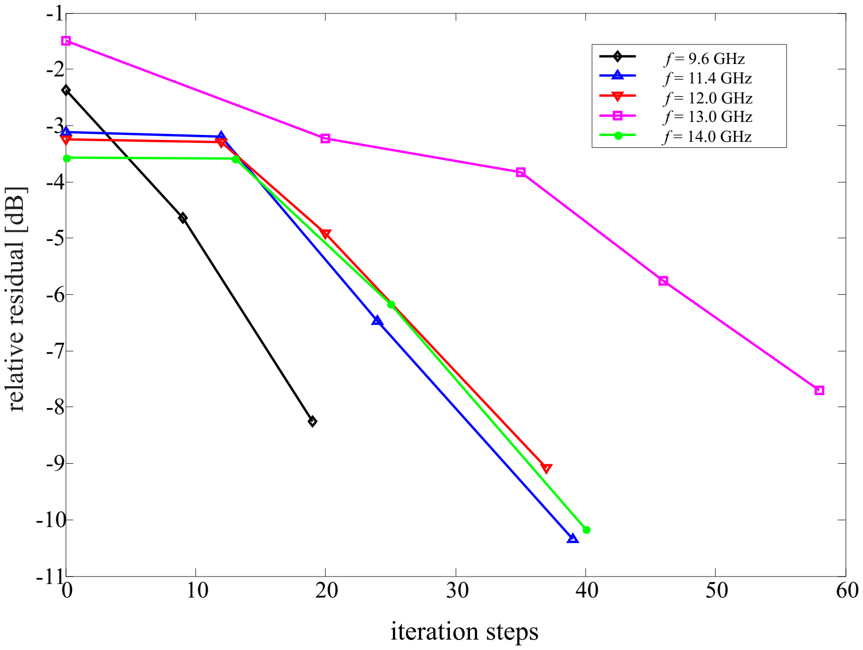

Figure 8.16: Convergence of the maximum iterations for the unit cell according to Fig. 8.12 at different frequencies. The residual is defined with respect to the accuracy of the complex wavenumber. One iteration corresponds to one parabola evaluation and the iterations are counted independently from search direction.

8.4.2 1D Periodic Model with Finite Width

Here the periodic corrugated grounded dielectric slab with finite width of $w = 14$ mm along the x-axis, as depicted in Fig. 8.17 is analyzed. Again, in the driven method the impressed volume current density is designed to excite the TE modes and only the wavenumber along the y-axis, which is perpendicular to the grooves, is considered. As reference, the SMA method employs the absorbing layers around the unit cell of the antenna to enclose the open configuration, as shown in Fig. 8.18. Therefore, only a limited number of modes is sufficient to yield accurate results. There are two modes found in the frequency range of interest, which is $8 - 14$ GHz.

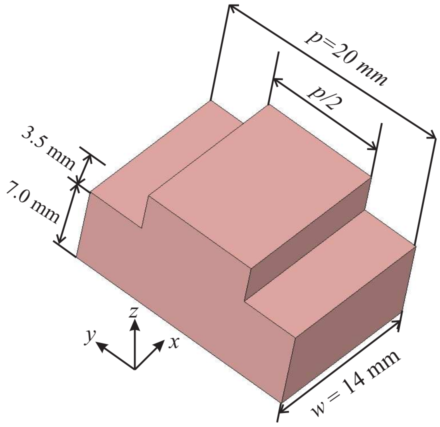

Figure 8.17: The periodic unit cell of the corrugated dielectric LWA with finite width.

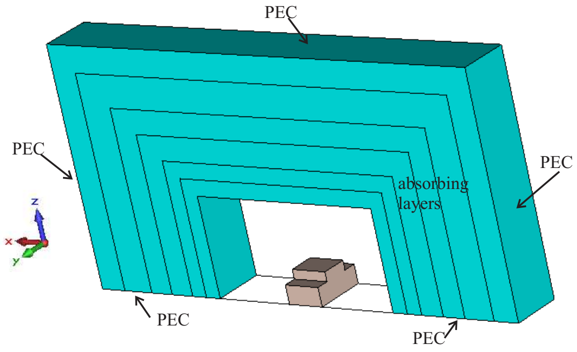

Figure 8.18: The CST MWS model for the periodic unit cell of the corrugated dielectric LWA with finite width in SMA with absorbing layers.

In Fig. 8.19, a perfect agreement for the propagation constant can be observed between the results from the driven method and the SMA approach with the absorbing layers. There are two modes in the operating frequency range, $8-14$ GHz. Both of them exhibit LH and RH behaviors in different frequency ranges. The first mode turns from a LH behavior into a RH one at 10.45 GHz while the second mode turns at 11.15 GHz.

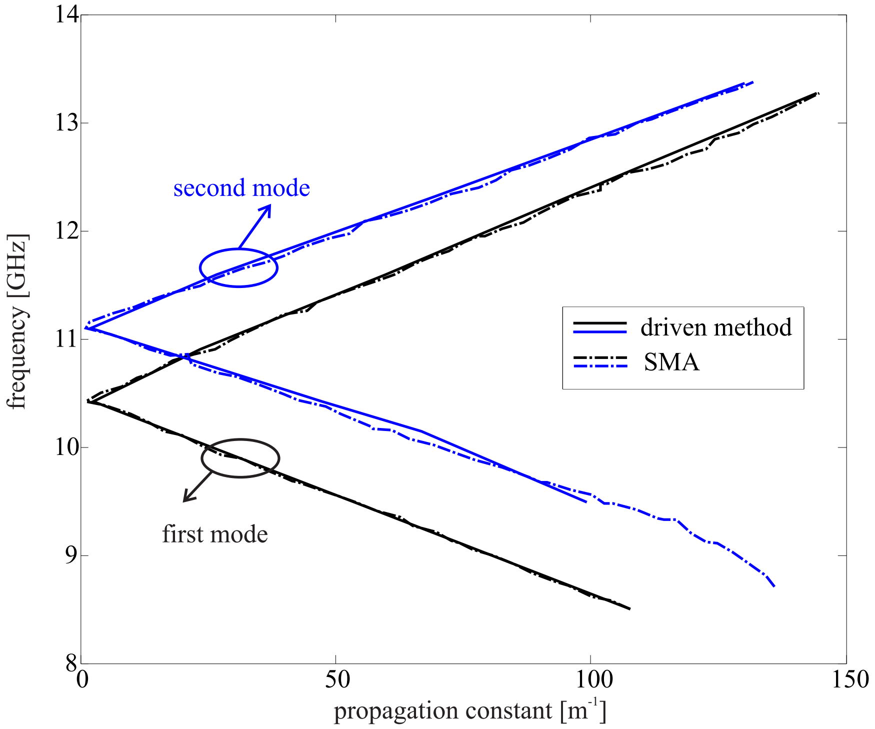

Figure 8.19: Dispersion diagram of the unit cell according to Fig. 8.17 compared to SMA with 8 modes.

For the attenuation constant depicted in Fig. 8.20, the results from the driven method agree very well with the ones from SMA approach and MP in [Weitsch & Eibert, 2012]. For SMA approach the limited air layer height in Fig. 8.18 makes the interference on the radiation field distribution between the simulation model and the absorbing layers not negligible. Also the finite number of modes considered at the ports in SMA might contribute to the deviation.

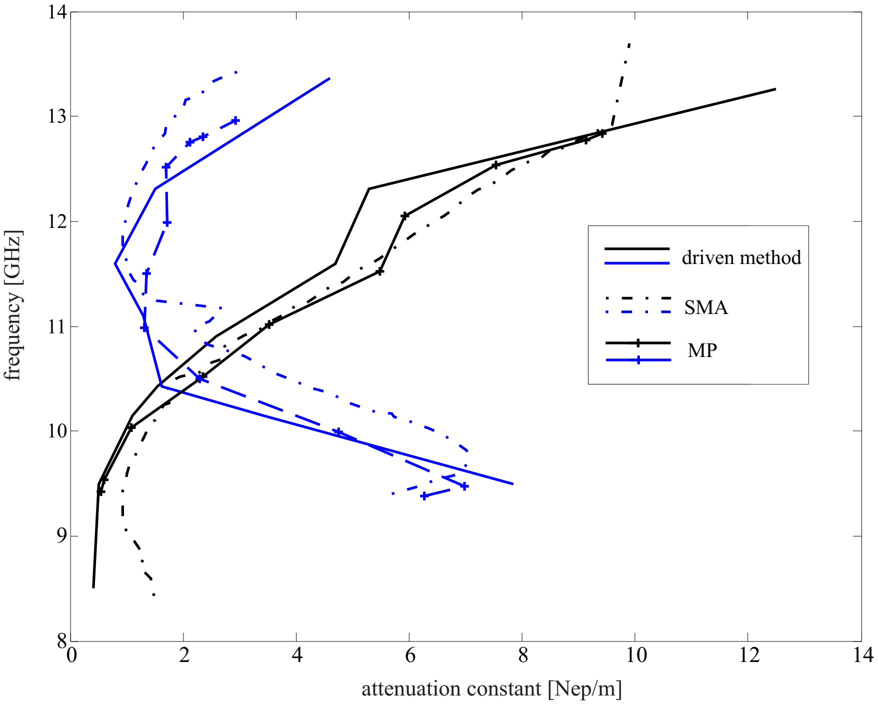

Figure 8.20: Attenuation constant of the unit cell according to Fig. 8.17 compared to SMA with 8 modes and matrix pencil (MP) from [Weitsch & Eibert, 2012].

Modal Field Solution For Different Modes At Different Frequencies

The modal field solution from the driven method can provide a good physical insight into the structure under analysis as well as it is an excellent tool to distinguish different modes. Fig. 8.21 demonstrates the E-field distribution at the cross section perpendicular to the wave propagation direction y-axis for the two modes at 13.3 GHz. It is clearly visible that there is more energy leaking out to the air for the first mode than the second mode at this frequency which also confirms the behavior of the attenuation constant in Fig. 8.20. The E-field distribution for the two modes at another frequency 10.0 GHz is depicted in Fig. 8.22. According to the attenuation diagram Fig. 8.20, at this frequency the second mode exhibits more radiation to the free space. The modal field distribution illustrates the same conclusion.

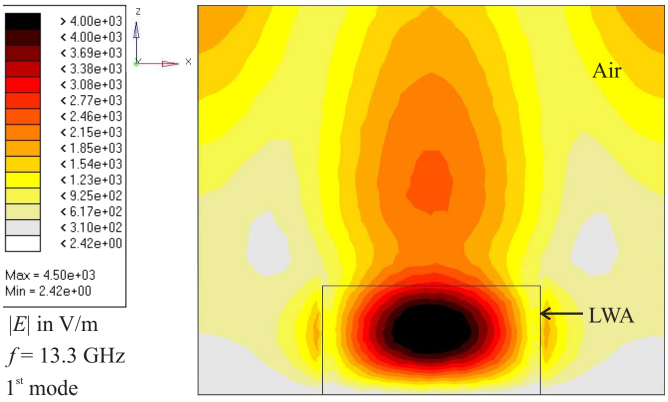

(a) first mode

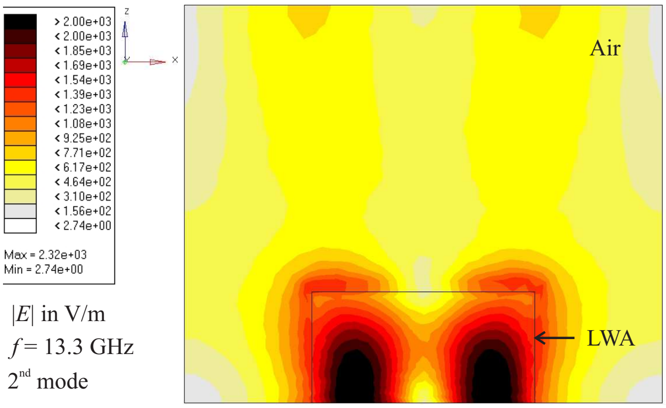

(b) second mode

Figure 8.21: Modal field distribution of the two modes at 13.3 GHz in the port of the corrugated slab in Fig. 8.17 in xz-plane. (a) first mode, (b) second mode.

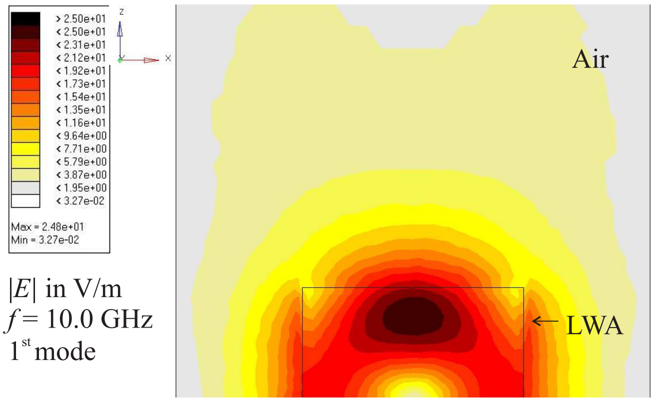

(a) first mode

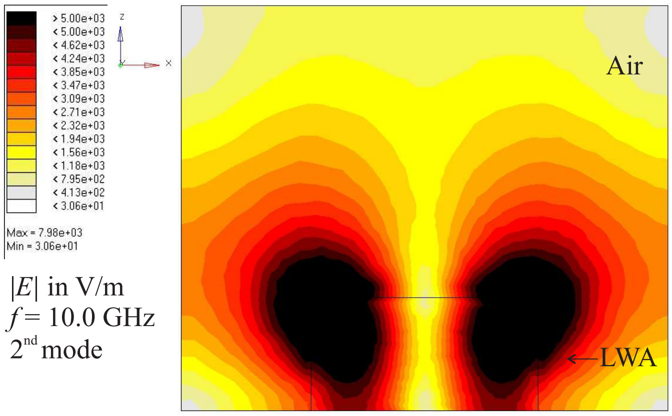

(b) second mode

Figure 8.22: Modal field distribution of the two modes at 10.0 GHz in the port of the corrugated slab in Fig. 8.17 in xz-plane. (a) first mode, (b) second mode.

8.5 Mushroom Structure for MTM: 2D Periodic Configuration

In this section, the mushroom configuration for a 2-dimensional metamaterial is analyzed to demonstrate the performance of the driven method for the 2-dimensional periodic configuration.

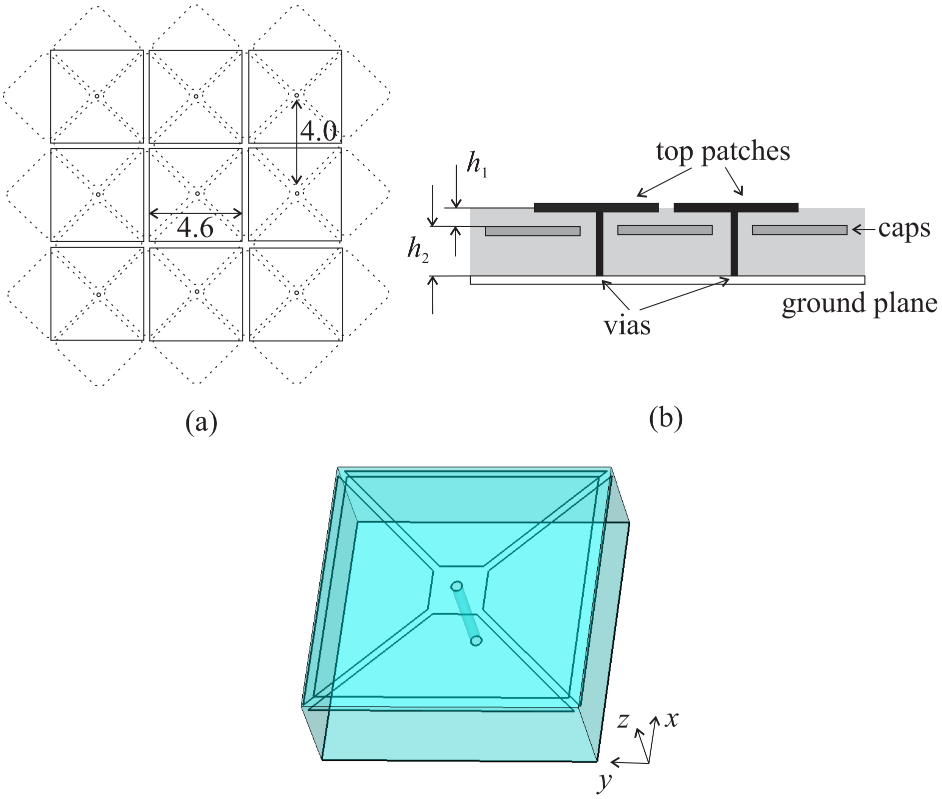

(a) (b)

(c)

Figure 8.23: The mushroom structure [Sanada et al., 2004] and its unit cell. The period of the unit cell is 5.0 mm × 5.0 mm. The mushroom structure consists of the top patches and a ground plane which are connected by vias. Between the top layer and the ground plane there is a dielectric substrate with $\varepsilon_r = 2.2$ and a cap layer under the top patches. (a) Dimensions of the top patches and the caps in mm. (b) The side view of the mushroom structure. The distance between the top patches and the caps is $h_1 = 0.127$ mm and the one between the caps and the ground plane is $h_2 = 1.697$ mm. (c) The unit cell of the mushroom structure.

Model Setup

As shown in Fig. 8.23, the mushroom structure consists of a layer of top patches and the ground plane. The top patches are connected to the ground plane by vias of 0.2 mm diameter. Between the top and the ground metal layers, a dielectric substrate with $\varepsilon_r = 2.2$ is sandwiched. Under the top patches inside the substrate there is a cap layer to introduce an extra series capacitor. The mushroom structure is periodic in x-and y-direction with the unit cell dimension of 5.0 mm × 5.0 mm. The thickness of the upper and lower substrates are $h_1 = 0.127$ mm and $h_2 = 1.697$ mm, respectively.

Dispersion and Attenuation Analysis

The mushroom structure is a 2D periodic configuration, along both the x- and y-direction. Therefore, the dispersion diagram is a 2D function $f_n(k_x, k_y)$, where n labels the number of the mode. In [Sanada et al., 2004], *Brillouin zone* and *irreducible Brillouin zone* were introduced to demonstrate the dispersion curve for 2D metamaterials. In this work, *irreducible Brillouin zone* is considered. The dispersion diagrams are computed by the driven method and compared to the results from [Sanada et al., 2004] obtained by full-wave (FEM) analysis with periodic boundary conditions applied at the edges of the unit cell as depicted in Fig. 8.23(c) along both the x- and y-directions. Fig. 8.24 shows the mesh configuration of the mushroom unit cell in Fig. 8.23(c). On the surface, triangular meshes are applied as depicted in Fig. 8.24(b) while in the substrate, the first order tetrahedral meshes are employed. In total, 31 193 tetrahedral mesh cells were generated for the driven method. The average computation time for one frequency with the driven method was 1 165.5 s. A perfect match can be observed in Fig. 8.25 between the results from the driven method and the reference [Sanada et al., 2004].

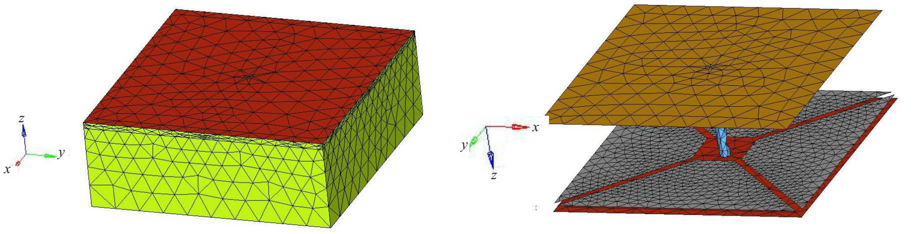

(a) The mesh configuration of the mushroom unit cell in Fig. 12(c). (b) The meshes for the top layer, the cap layer and the ground plane.

Figure 8.24: The mesh configuration of the mushroom unit cell.

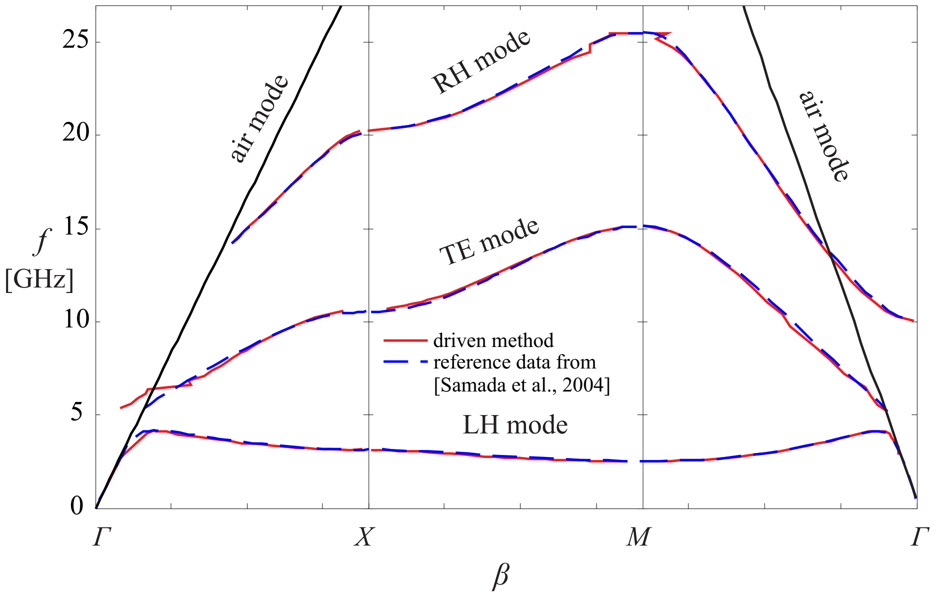

Figure 8.25: Dispersion diagrams of the mushroom structure in Fig. 8.23 compared to the reference data from [Sanada et al., 2004].

Fig. 8.26 and Fig. 8.27 give some examples of modal field distribution of the mushroom structure in irreducible Brillouin zone. Fig. 8.26 demonstrates the E-field distributions of the three modes in $\Gamma - X$ segment of irreducible Brillouin zone. The E-field distributions on different cross sections which belong to one mode are displayed in one column. LH mode at 2.62 GHz is in the first column, TE mode at 9.11 GHz is in the second column, and in the third column it is RH mode at 14.23 GHz. In each line collect the field distributions at one cross section. The first line shows the field distributions at xy-plane, the second line yz-plane, and the third line zx-plane. The E-field distributions for RH mode in different segments of irreducible Brillouin zone are depicted in Fig. 8.27. The E-field distributions at 14.23 GHz in segment $\Gamma - X$ are in the first column, the ones at 23.68 GHz in $X - M$ are in the second column, and the ones at 13.93 GHz in $M - \Gamma$ are in the third column.

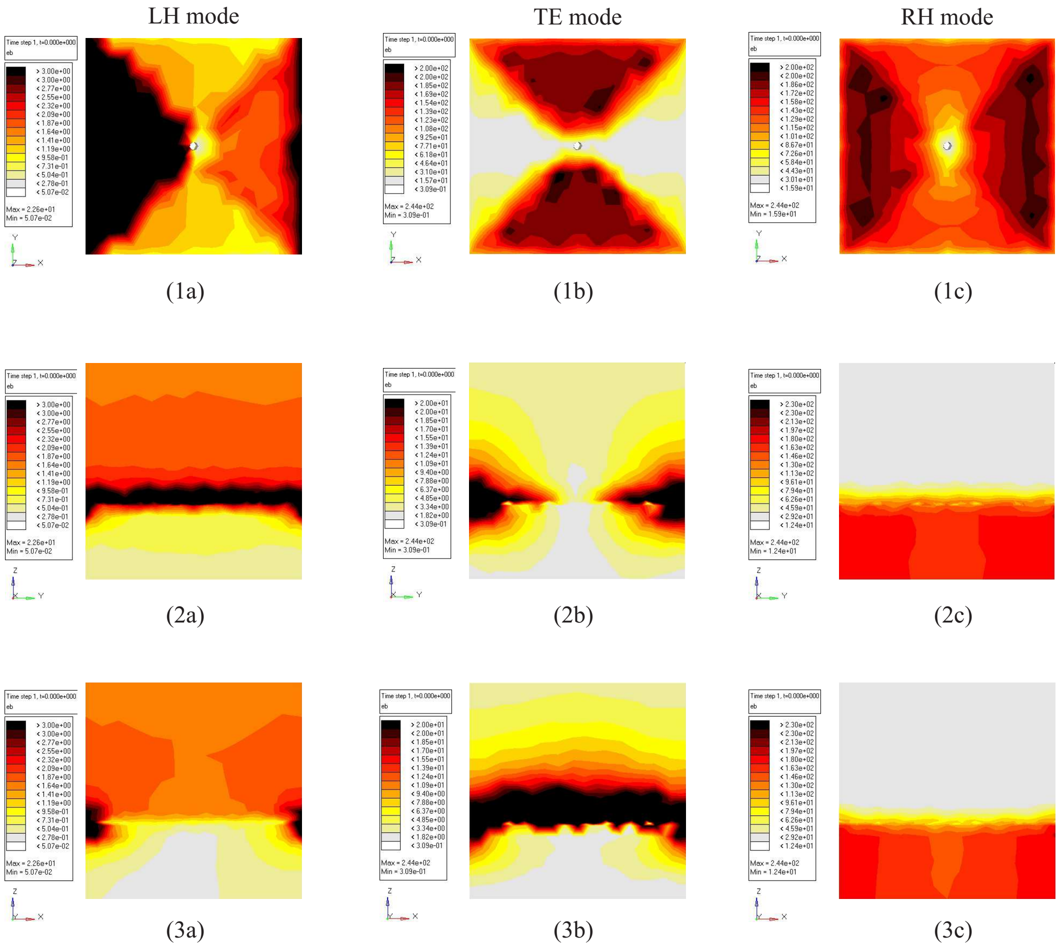

(1a) (1b) (1c)

(2a) (2b) (2c)

(3a) (3b) (3c)

Figure 8.26: Modal field distribution of the three modes of the mushroom structure in Fig. 8.23 in $\Gamma - X$ segment of irreducible Brillouin zone. The first column is LH mode, the second column is TE mode, the third column is RH mode. (a), (b), and (c) stand for the cross section of xy-, yz-, and zx-plane, respectively.

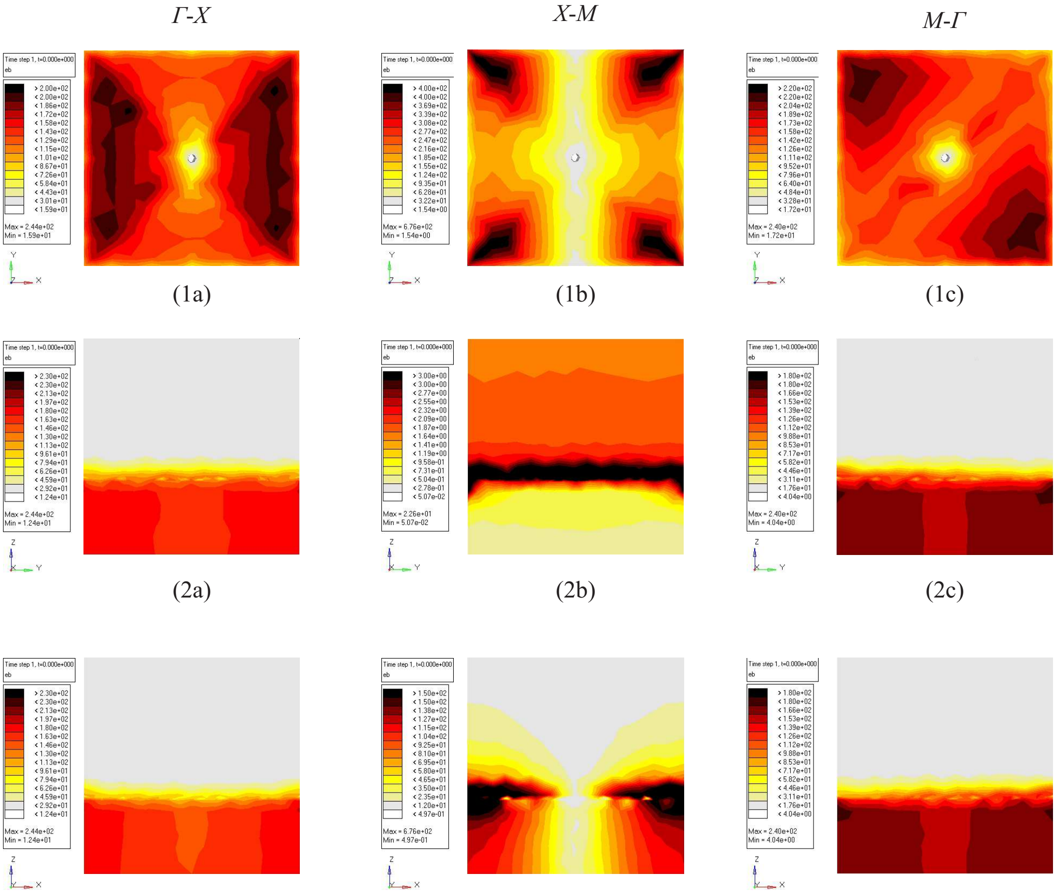

(1a) (1b) (1c)

(2a) (2b) (2c)

(3a) (3b) (3c)

Figure 8.27: Modal field distribution of the RH modes of the mushroom structure in Fig. 8.23 in irreducible Brillouin zone. The first column is in the segment $\Gamma - X$, the second column is in the segment $X - M$, the third column is in the segment $M - \Gamma$. (a), (b), and (c) stand for the cross section of xy-, yz-, and zx-plane, respectively.

9 Conclusions

The driven eigenproblem computation method opens up a new possibility to solve eigenproblems by solving the corresponding excitation problems in the eigenvalue domain. It is suitable especially for periodic structures, like metamaterials and substrate integrated waveguides, which according to Floquet's theorem can be analyzed in an appropriately discretized unit cell with periodic boundary conditions. The unit cell can be analogized to a resonator in the eigenproblem aspect with the resonance frequencies as eigenvalues. Instead of directly solving the eigenproblem in the resonator as many other eigenproblem-based numerical solvers do, the driven method intends to find the eigenvalues, here the resonance frequencies, by providing the excitations to the system. Therefore, the source free eigenproblems are transformed into excited eigenvalue problems. Additionally, solving the excitation problem directly in the eigenvalue domain, other than time domain as other excitation algorithms do, can concentrate the energy to an isolated mode and avoid the restrain of limited observation time.

Providing excitations to the system is realized in this work by two methods. One is port excitation based on electric circuits and network theory. The other is internal distributed current densities excitation. The port excitation, which couples external energy into the structure under analysis, is vivid, explicit and compatible with other commercial numerical solvers, e.g. CST Microwave Studio, and easy to regularize the resonance behavior by port impedances. However, the coupling coefficient between the excitation ports and the structure under analysis will influence searching of eigenvalues, the resonance frequencies, through S-parameters. Although this can be solved by monitoring other observables like the fields in the solution domain, its application is sometimes restricted to small attenuation scenarios by the limitation in the flexibility of the periodic boundary configurations. The perturbation method is employed with the port excitation to analyze the attenuation for guided modes. The attenuation inside the stop band for evanescent and leaky modes can not be analyzed by the perturbation method. On the other hand, the distributed current densities excitation can stimulate in principle all possible modes by electric and magnetic current densities with different distributions and polarizations in the solution domain. With the expectation and understanding of the fields in the solution domain, some specific modes of the fields can be excited by appropriately designed current densities. Moreover, this kind of excitations has more freedom in eigenvalues searching since some arbitrary observable of the field solution, such as the electric field in the solution domain, or some integral measure of it can be evaluated. The distributed current densities excitation is implemented in a hybrid finite element boundary integral solver (FEBI). FEBI employs a spectral domain integral equation with a Floquet mode based periodic Green's function interior to the edge-based periodic boundary condition and the surface integral equation formulations exterior to the boundary for the scattering and radiation of the open structures. In FEBI, a complex wavevector is allowed in the periodic boundaries and Green's functions, which makes evanescent and leaky modes as well as guided modes analysis possible. Additionally FEBI with doubly periodic configuration is more robust in one- and two-dimensional artificial material compositions like metamaterials.

The eigenvalue (frequency, wavevector) and eigenmodes can fully characterize the properties of a microwave system. Searching the eigenvalues and eigenmodes in an excited resonator can be realized by monitoring the port S-parameters or the field quantities in the solution domain, which always reach maxima at the resonance frequency. This makes the eigenvalue searching in the resonator an optimization procedure. With some initial estimations based on the previous solutions, the driven method repeats the iterations of the solution of the excitation problem with slightly varying parameters. This can be performed by sweeping the frequency with a fixed wavevector as well as scanning the complex plane of the wavevector at a fixed frequency, which is more suitable for the complex modes like evanescent and leaky modes. Some methods like Brent's and Powell's methods are introduced to accelerate the speed of convergence of the searching iterations. When more than one mode is relevant in the operating frequency range, a global optimization is needed to detect all the local extrema corresponding to the different modes.

The driven method shows the great versatility and accuracy in the dispersion and attenuation analysis of periodic structures. The examples of a classical rectangular waveguide and a substrate integrated waveguide verifies the good accuracy of the driven method compared to analytical methods. In contrast to the scattering matrix approach based on the modal series expansion, the driven method is more robust and accurate in the composite right-/left-handed leaky wave antenna example. The periodically modulated grounded dielectric corrugated leaky wave antenna examples also demonstrate the efficiency of the driven method for one-dimensional open periodic structures where the computation consumption and time are greatly reduced while the accuracy is maintained compared to the scattering matrix approach. Even with multiple modes operation, the driven method can still easily distinguish among different modes and analyze the mode dispersions. A two-dimensional metamaterial based on mushroom structure shows the capability of the driven method in even more complicated structures.

10 Appendix

10.1 General Properties of the Eigenfunctions

Take a wave propagating with a propagation constant β in a waveguide with uniform cross section along the y-axis as an example. The electromagnetic fields for TE, TM, or TEM can be represented as $\phi(x,z)e^{-j\beta y}$ which have to satisfy the Helmholtz equations,

$$(\nabla_t^2 + k_c^2)\phi(x,z) = 0, \tag{10.1.1}$$

where ∇_t is a Nabla operator in the transverse plane, here is $x-z$ plane. $k_c = \sqrt{k_x^2 + k_z^2}$ is called cutoff wavenumber which is a constant quantity and depends only on the geometry of the guide. Once k_c is obtained, the propagation constant $\beta = k_y$ is given by

$$\beta = k_y = \sqrt{k^2 - k_c^2}, \tag{10.1.2}$$

with $k = \omega\sqrt{\mu\varepsilon}$ the wavenumber of the material filling the transmission line or waveguide region. Here the function $\phi(x,z)$ satisfying (10.1.1) is called the eigenfunction and constant k_c is the eigenvalue. There can be a set of doubly infinite number of eigenfunctions,

$$\phi_{mn}, \quad m,n = 0,1,2,\ldots,\infty, \tag{10.1.3}$$

according to the different boundary conditions, e.g. the Dirichlet's boundary condition

$$\phi(x,z) = 0, \quad \text{on the boundary}, \tag{10.1.4}$$

or the Neumann's boundary condition

$$\frac{\partial\phi}{\partial n} = 0, \quad \text{on the boundary}, \tag{10.1.5}$$

and with corresponding eigenvalue k_{mn}.

Orthogonality

The eigenfunctions are orthogonal to each other. Consider two eigenfunctions ϕ_{mn} and $\phi_{m'n'}$ which both satisfy the wave equations,

$$(\nabla^2 + k_{mn}^2)\phi_{mn} = 0. \tag{10.1.6}$$

$$(\nabla^2 + k_{m'n'}^2)\phi_{m'n'} = 0. \tag{10.1.7}$$

Multiply Eq. (10.1.6) with $\phi_{m'n'}$ and subtract the result from the multiplication of Eq. (10.1.7) and ϕ_{mn}, we get

$$\phi_{m'n'}\nabla^2\phi_{mn} - \phi_{mn}\nabla^2\phi_{m'n'} = (k^2_{m'n'} - k^2_{mn})\phi_{mn}\phi_{m'n'}. \tag{10.1.8}$$

Integrate the both sides of Eq. (10.1.8) and due to the Green's second identity, we can obtain

$$\int_l \left(\phi_{m'n'}\frac{\partial\phi_{mn}}{\partial n} - \phi_{mn}\frac{\partial\phi_{m'n'}}{\partial n}\right) dl = (k^2_{m'n'} - k^2_{mn})\int_s \phi_{m'n'}\phi_{mn} ds, \tag{10.1.9}$$

where s is the cross-sectional area, and l is the contour of the cross section. Because ϕ_{mn} and $\phi_{m'n'}$ satisfy either the Dirichlet's or the Neumann's boundary condition, the left side of Eq. (10.1.9) will vanish and it can be rewritten as

$$(k^2_{m'n'} - k^2_{mn})\int_s \phi_{m'n'}\phi_{mn} ds = 0. \tag{10.1.10}$$

Therefore when $m \neq m'$ and $n \neq n'$, $k_{mn} \neq k_{m'n'}$, the integral in Eq. (10.1.10) must be zero, which can be written as

$$\int_s \phi_{mn}\phi_{m'n'} ds = N_{mn}\delta_{mm'}\delta_{nn'}, \tag{10.1.11}$$

with

$$\delta_{mm'} = \begin{cases} 1 & \text{for} \quad m = m' \\ 0 & \text{for} \quad m \neq m' \end{cases} \tag{10.1.12}$$

and N_{mn} is the normalizing factor

$$N_{mn} = \int_s \phi^2_{mn} ds. \tag{10.1.13}$$

Completeness

The eigenfunctions form a complete set, with which any continuous function $f(\boldsymbol{r})$ can be expanded, as

$$f(\boldsymbol{r}) = \sum_m^\infty \sum_n^\infty A_{mn}\phi_{mn}(\boldsymbol{r}), \tag{10.1.14}$$

where $\boldsymbol{r} = x\hat{x} + y\hat{y}$. A_{mn} is the coefficient which can be defined as

$$A_{mn} = \frac{\int_s f(\boldsymbol{r})\phi_{mn}(\boldsymbol{r})ds}{\int_s \phi_{mn}(\boldsymbol{r})^2 ds}. \tag{10.1.15}$$

A delta function $\delta(\boldsymbol{r} - \boldsymbol{r'})$ can also be expressed in a series expansion of eigenfunctions,

$$\delta(\boldsymbol{r} - \boldsymbol{r}') = \sum_m^\infty \sum_n^\infty \frac{\phi_{mn}(\boldsymbol{r})\phi_{mn}(\boldsymbol{r}')}{\int_s \phi_{mn}(\boldsymbol{r})^2 ds}. \tag{10.1.16}$$

10.2 General Matrix System for CRLH 2D Networks

Similar to the CRLH 1D network, a general structure of CRLH 2D network as shown in Fig. 10.1 with the unit cell as depicted in Fig. 10.2 is considered.

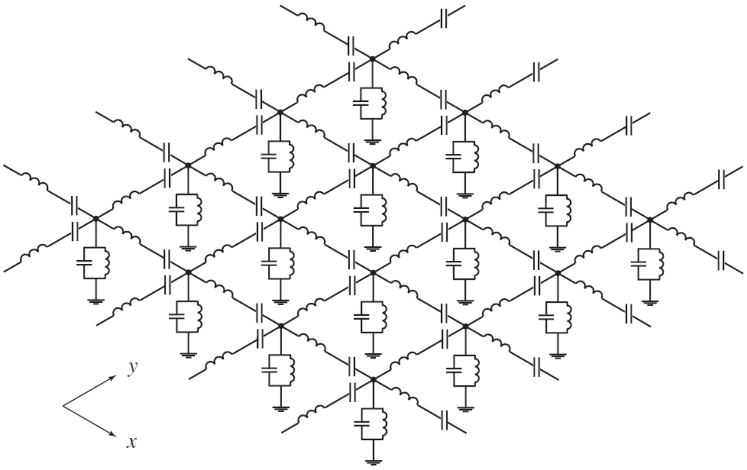

Figure 10.1: A 2D CRLH network consisting of the unit cell depicted in Fig. 10.2 repeated along both the x- and y-axis.

The input and output voltages and currents can be related using the transmission matrix $[ABCD]$ as shown in Fig. 10.2(b) and thee center node voltage V_0 can be obtained when the periodic boundary conditions are applied with periods p_x and p_y along the x- and y-axis, respectively [Caloz & Itoh, 2006]

$$V_x^{i0} = V_0 = \frac{D_x^i V_x - B_x^i I_x}{A_x^i D_x^i - B_x^i C_x^i}, \tag{10.2.1}$$

$$V_y^{i0} = V_0 = \frac{D_y^i V_y - B_y^i I_y}{A_y^i D_y^i - B_y^i C_y^i}, \tag{10.2.2}$$

$$V_x^{o0} = V_0 = (A_x^o V_x + B_x^o I_x) e^{-jk_x p_x}, \tag{10.2.3}$$

$$V_y^{o0} = V_0 = (A_y^o V_y + B_y^o I_y) e^{-jk_y p_y}, \tag{10.2.4}$$

$$V_s h^0 = V_0 = \frac{-B_{sh} I_{sh}^i}{A_{sh} D_{sh} - B_{sh} C_{sh}}, \tag{10.2.5}$$

$$\tag{10.2.6}$$

where k_x and k_y are the wavenumbers along the x- and y-axis, respectively. Additionally,

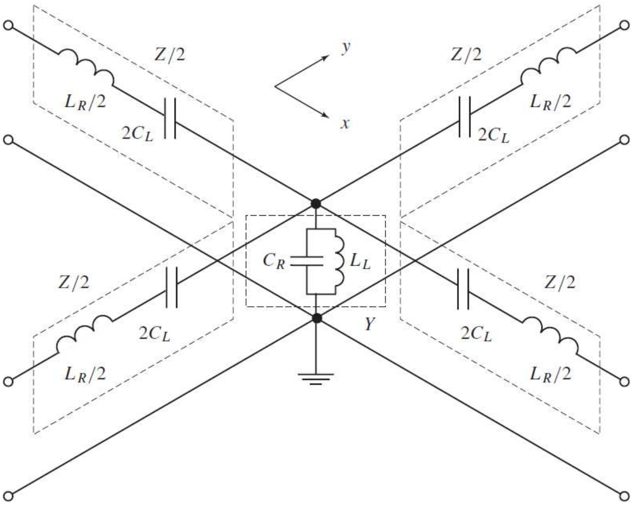

(a) The unit cell of the CRLH 2D network in Fig. 10.1. The network is periodic along x- and y-axis with the period of k_x and k_y, respectively.

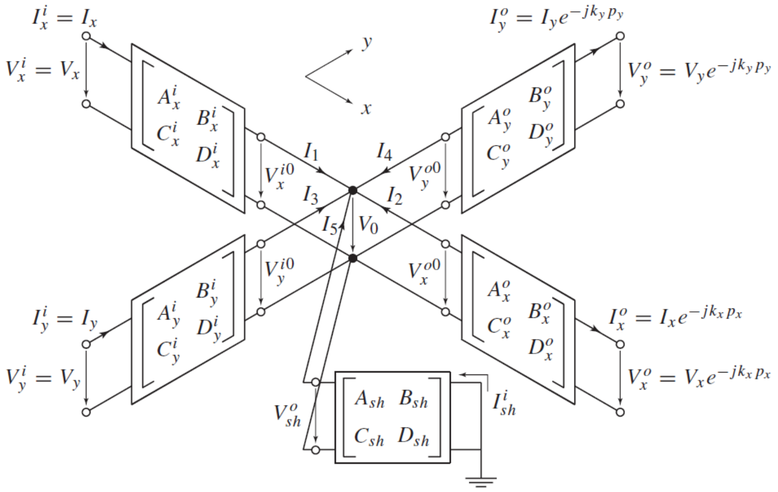

(b) The matrix representation of the unit cell. The output currents and voltages are related to the input currents and voltages by the periodic boundary conditions. The phase shift can be represented as $\varphi_x = k_x p_x$ and $\varphi_y = k_y p_y$ where k_x and k_y are the wavenumbers, respectively.

Figure 10.2: Unit cell of the 2D CRLH network in Fig. 10.2 [Caloz & Itoh, 2006].

according to Kirchoff's current law the current for the center node can be obtained as

$$\begin{aligned}\sum_{k=1}^{5} I_k =& \frac{-C_x^i V_x + A_x^i I_x}{A_x^i D_x^i - B_x^i C_x^i} + \frac{-C_y^i V_y + A_y^i I_y}{A_y^i D_y^i - B_y^i C_y^i} \\ & - (C_x^o V_x + D_x^o I_x) e^{-jk_x p_x} - (C_y^o V_y + D_y^o I_y) e^{-jk_y p_y} \\ & + \frac{A_{sh} I_{sh}^i}{A_{sh} D_{sh} - B_{sh} C_{sh}} = 0. \end{aligned} \tag{10.2.7}$$

Combining Eq. (10.2.1) to (10.2.5) with (10.2.7) a linear matrix system for the unknowns V_x, I_x, V_y, and I_y can be obtain

$$[M] \begin{pmatrix} V_x \\ I_x \\ V_y \\ I_y \end{pmatrix} = \begin{pmatrix} 0 \\ 0 \\ 0 \\ 0 \end{pmatrix}, \tag{10.2.8}$$

where

$$[M] = \begin{pmatrix} \alpha - \frac{D_x^i A_{sh}}{B_{sh} \Delta_x^i} & \beta + \frac{B_x^i A_{sh}}{B_{sh} \Delta_x^i} & \gamma & \delta \\ \alpha & \beta & \gamma - \frac{D_y^i A_{sh}}{B_{sh} \Delta_y^i} & \delta + \frac{B_y^i A_{sh}}{B_{sh} \Delta_y^i} \\ \alpha - \frac{A_x^o A_{sh} e_x}{B_{sh}} & \beta - \frac{B_x^o A_{sh} e_x}{B_{sh}} & \gamma & \delta \\ \alpha & \beta & \gamma - \frac{A_y^o A_{sh} e_y}{B_{sh}} & \delta + \frac{B_y^o A_{sh} e_y}{B_{sh}} \end{pmatrix}, \tag{10.2.9}$$

with

$$\alpha = -C_x^o e_x - \frac{C_x^i}{\delta_x^i}, \beta = -D_x^o e_x - \frac{A_x^i}{\delta_x^i}, \gamma = -C_y^o e_y - \frac{C_y^i}{\delta_y^i}, \delta = -D_y^o e_y - \frac{A_y^i}{\delta_y^i}, \tag{10.2.10}$$

$$\Delta_u^i = A_u^i D_u^i - B_u^i C_u^i, \quad (u = x, y), \tag{10.2.11}$$

$$e_x = e^{-jk_x p_x}, \text{ and } e_y = e^{-jk_y p_y}. \tag{10.2.12}$$

This system has a nontrivial solution when

$$\det [M] = \det [M(k_x, k_y; \omega)] = 0. \tag{10.2.13}$$

When an isotropic network with impedances $Z/2$ and admittance Y, which is as shown in Fig. 10.2(a), is considered, Eq. (10.2.13) can be simplified after substitution of the appropriate $ABCD$ parameters [Pozar, 2004]

$$\begin{aligned}
&A_x^i = A_y^i = A_x^o = A_y^o = 1,\\
&B_x^i = B_y^i = B_x^o = B_y^o = Z/2,\\
&C_x^i = C_y^i = C_x^o = C_y^o = 0,\\
&D_x^i = D_y^i = D_x^o = D_y^o = 1,\\
&A_{sh} = 1,\ B_{sh} = 0,\ C_{sh} = Y,\ D_{sh} = 1,\\
&\Delta_u^i = 1,\ (u = x, y)\ \text{(reciprocal network branches).} \qquad (10.2.14)
\end{aligned}$$

After some calculations, we can obtain

$$\frac{(1-e^{-jk_xp_x})^2}{e^{-jk_xp_x}} + \frac{(1-e^{-jk_yp_y})^2}{e^{-jk_yp_y}} - ZY = 0, \qquad (10.2.15)$$

which can also be written as

$$2 - \cos(k_xp_x) - \cos(k_yp_y) - \frac{\chi}{2} = 0, \qquad (10.2.16)$$

where χ is defined as

$$\begin{aligned}
\chi &= (\frac{\omega}{\omega_R})^2 + (\frac{\omega_L}{\omega})^2 - \kappa\omega_L^2, && (10.2.17)\\
\omega_R &= \frac{1}{\sqrt{L_RC_R}}\ \text{(rad/s)}, && (10.2.18)\\
\omega_L &= \frac{1}{\sqrt{L_LC_L}}\ \text{(rad/s)}, && (10.2.19)\\
\kappa &= L_RC_L + L_LC_R\ \ (\text{s/rad})^2. && (10.2.20)
\end{aligned}$$

Therefore, along the Brillouin zone (BZ) of the periodic lattice, the wavenumbers k_x and k_y can be derived as

$$\begin{aligned}
\Gamma - X(0 < k_xp_x < \pi, k_yp_y = 0) : k_x &= \frac{1}{p_x}\cos^{-1}(1 - \frac{\chi}{2}), && (10.2.21)\\
X - M(k_xp_x = \pi, 0 < k_yp_y < \pi) : k_y &= \frac{1}{p_y}\cos^{-1}(3 - \frac{\chi}{2}), && (10.2.22)\\
M - \Gamma(0 < k_up_u < \pi, u = x, y) : k_u &= \frac{1}{p_u}\cos^{-1}(1 - \frac{\chi}{4}). && (10.2.23)
\end{aligned}$$

10.3 Periodic Green's Function

Consider a periodic structure with period ρ_a in the x axis and ρ_b in y axis, and one unit cell defined by $0 < x < \rho_a$, $0 < y < \rho_b$, and $-\infty < z < \infty$. Within the unit cell, the Green's function G has to satisfy

$$(\nabla^2 + \boldsymbol{k}^2)G = -\delta(x - x')\delta(y - y')\delta(z - z'). \qquad (10.3.1)$$

Expanding G in the Floquet series,

$$G = \sum_m \sum_n g_{mn}(z, z')e^{-jk_{xm}x - jk_{yn}y}, \tag{10.3.2}$$

where $k_{xm} = k_{x0} + 2m\pi/\rho_a$ and $k_{ym} = k_{y0} + 2n\pi/\rho_b$. Substituting Eq. (10.3.2) into (10.3.1) and noting that

$$\delta(x - x') = \sum_m \frac{e^{-jk_{xm}(x-x')}}{\rho_a}, \tag{10.3.3}$$

$$\delta(y - y') = \sum_n \frac{e^{-jk_{yn}(y-y')}}{\rho_b}, \tag{10.3.4}$$

then G can be written as

$$G = \sum_{m=-\infty}^{\infty} \sum_{n=-\infty}^{\infty} \frac{e^{-jk_{xm}(x-x') - jk_{yn}(y-y')}}{2jk_{zmn}(\rho_a \rho_b)} e^{-jk_{zmn}|z-z'|}, \tag{10.3.5}$$

and $k_{zmn} = \pm\sqrt{k_0^2 - k_{xm}^2 - k_{yn}^2}$. If the k_{xm} and k_{yn} are treated as the transverse wave vector $\boldsymbol{k}_{tmn} = \boldsymbol{k}_{t00} + 2\pi(\frac{m}{\rho_a}\hat{x} + \frac{n}{\rho_b}\hat{y})$ and consider $\boldsymbol{\rho}$ as the projection of the field point $\boldsymbol{r}$ on the xy-plane with $\boldsymbol{r} = \boldsymbol{\rho} + z\hat{z}$, the G can be rewritten as

$$G(\boldsymbol{r}, \boldsymbol{r}') = \sum_{m=-\infty}^{\infty} \sum_{n=-\infty}^{\infty} \frac{e^{-j\boldsymbol{k}_{tmn}\cdot(\boldsymbol{\rho}-\boldsymbol{\rho}')}}{2Ajk_{zmn}} e^{-jk_{zmn}|z-z'|}. \tag{10.3.6}$$

Here A is the area of the cross section of the unit cell's top or bottom boundary surface.

List of Figures

Bibliography

[Abramowitz & Stegun, 1984] Abramowitz, M. & Stegun, I. A. (1984). *Pocketbook of Mathematical Functions.* Frankfurt am Main: Verlag Harri Deutsch.

[Akhmanov & Nikitin, 1997] Akhmanov, A. & Nikitin, S. Y. (1997). *Physical Optics.* Oxford University Press.

[Asvestas, 1980] Asvestas, J. S. (1980). The physical optics method in electromagnetic scattering. *Journal of Mathematical Physics*, 21(2), 290–299.

[Baba, 1981] Baba, N. (1981). Convergence of a random optimization method for constrained optimizations problems. *Journal of Optimization Theory and Applications*, 33(4), 451–461.

[Bahl & Bhartia, 2003] Bahl, I. & Bhartia, P. (2003). *Microwave Solid State Circuit Design.* Wiley-Interscience, second edition.

[Bao et al., 2012] Bao, J., Tong, C., Zou, X., & Yu, D. (2012). Ridged substrate integrated waveguide. In *International Conference on Microwave and Millimeter Wave Technology (ICMMT)*, volume 2 (pp. 1–4).

[Basu et al., 2006] Basu, S., Pollack, R., & Roy, M. (2006). *Algorithms in Real Algebraic Geometry.* Berlin: Springer.

[Baum et al., 1991] Baum, C. E., Rothwell, E. J., Chen, K.-M., & Nyquist, D. P. (1991). The singularity expansion method and its application to target identification. *Proceeding of the IEEE*, 79(10), 1481–1492.

[Bérenger, 1994] Bérenger, J. P. (1994). A perfectly matched layer for the absorption of electromagnetic waves. *Journal of Computational Physics*, 114(2), 185–200.

[Bondeson et al., 2005] Bondeson, A., Rylander, T., & Ingelstrom, P. (2005). *Computational Electromagnetics.* New York: Springer Science.

[Bozzi et al., 2006] Bozzi, M., Perregeini, L., & Wu, K. (2006). Direct determination of multi-mode equivalent circuit models for discontinuities in substrate integrated waveguide. In *2006 IEEE MTT-S International Microwave Symposium Digest, June 11–16, San Francisco, USA* (pp. 68–71).

[Bozzi et al., 2009] Bozzi, M., Rerregrini, L., Wu, K., & Arcioni, P. (2009). Current and future research trends in substrate integraged waveguide technology. *Radioengineering*, 18(2), 201–208.

[Brent, 2002] Brent, R. P. (2002). *Algorithms for Minimization without Derivatives.* Englewood Cliffs, Prentice Hall.

[Caloz & Itoh, 2002] Caloz, C. & Itoh, T. (2002). Application of the transmission line theory of left-handed (LH) materials to the realization of a microstrip lh transmission line. In *Progress in IEEE International Symposium on Antenna and Propagation and USNC/URSI National Radio Science Meeting, June 2002, San Antonio, USA*, volume 52 (pp. 412–415).

[Caloz & Itoh, 2003] Caloz, C. & Itoh, T. (2003). Novel microwave devices and structures based on the transmission line approach of meta-materials. In *2003 IEEE MTT-S International Microwave Symposium Digest, June 8–13, Philadelphia, USA*, volume 1 (pp. 195–198).

[Caloz & Itoh, 2006] Caloz, C. & Itoh, T. (2006). *Electromagnetic Metamaterials: Transmission Line Theory and Microwave Applications.* New Jersey: Wiley-interscience.

[Cassivi et al., 2002] Cassivi, Y., Perregrini, L., Arcioni, P., Wu, K., & Conciauro, G. (2002). Dispersion characteristics of substrate integrated rectangular waveguide. *IEEE Microwave and Wirless Components Letters*, 12(9), 333–335.

[Cesari & Abel, 1972] Cesari, C. S. & Abel, J. F. (1972). *Introduction to the Finite Element Method: a Numerical Approach for Engineering Analysis.* New York: Van Nostrand Reinhold.

[Chen et al., 1988] Chen, G. L., Owens, T. L., & Whealton, J. H. (1988). Theoretical study of the folded waveguide. *IEEE Trans. Plasma Sci.*, 16(2), 305–311.

[Chen et al., 2011] Chen, H., Schmidt, C. H., Che, W., & Eibert, T. F. (2011). Dispersion and attenuation analysis of substrate integrated waveguide by driven eigenproblem compuation. In *European Conference on Antenna and Propagation (EuCAP), April 2011, Rome, Italy* (pp. 643–646).

[Collin, 1991] Collin, R. E. (1991). *Field Theory of Guided Waves.* New York: IEEE Press.

[CST, 2011] CST (2011). 3d em field simulation mws microwave studio - cst computer simulation technology. `http://www.cst.com`.

[Davidson, 2005] Davidson, D. B. (2005). *Computational Electromagnetics for RF and Microwave Engineering.* Cambridge, UK: Cambridge University Press.

[Derudder et al., 1998] Derudder, H., de Zutter, D., & Olyslager, F. (1998). Analysis of waveguide discontinuities using perfectly matched layers. *Electronics Lett.*, 34(2), 21385–2140.

[Derudder et al., 2001] Derudder, H., Olyslager, F., de Zutter, D., & van den Berghe, S. (2001). Efficient mode-matching analysis of discontinuities in finite planar subsrates using perfectly matched layers. *IEEE Transactions on Antennas and Propagation*, 49(2), 185–195.

[Deslandes & Wu, 2006] Deslandes, D. & Wu, K. (2006). Accurate modeling, wave mechanisms, and design considerations of a substrate integrated waveguide. In *2002 IEEE MTT-S International Microwave Symposium Digest, June 2–6, Seattle, USA*, volume 54.

[Duran & Grossmann, 1986] Duran, M. A. & Grossmann, I. E. (1986). An outer-approximation algorithm for a class of mixed-integer nonlinear programs. *Mathmatical Programming*, 36, 307–339.

[Earl & Deem, 2005] Earl, D. J. & Deem, M. W. (2005). Parallel tempering: theory, applications, and new perspectives. *Physical Chemistry Chemical Physics*, 7, 3910–3916.

[Eibert et al., 2011] Eibert, T., Weitsch, Y., & Chen, H. (2011). Dispersion analysis of periodic structures by solving corresponding excitation problems. In *German Microwave Conference (GeMIC)* (pp. 1–4). Darmstadt, Germany.

[Eibert et al., 2003] Eibert, T. F., Erdemli, Y. E., & Volakis, J. L. (2003). Hybrid finite element-fast spectral domain multilayer boundary integral modeling of doubly periodic structures. *IEEE Transactions on Antennas and Propagation*, 51(9), 2517–2520.

[Eibert et al., 1999] Eibert, T. F., Volakis, J. L., Wilton, D. R., & Jackson, D. R. (1999). Hybrid FE/BI modeling of 3D doubly periodic structures utilizing triangular prismatic elements and a MPIE formulation accelerated by the Ewald transformation. *IEEE Transactions on Antennas and Propagation*, 47(5), 843–850.

[Eibert et al., 2012] Eibert, T. F., Weitsch, Y., Chen, H., & Gruber, M. E. (2012). Solving periodic eigenproblems by solving corresponding excitation problems in the domain of the eigenvalue. *Progress in Electromagnetics Research*, 126, 65–84.

[Felsen & Marcuvitz, 1994] Felsen, L. B. & Marcuvitz, N. (1994). *Radiation and Scattering of Waves*. IEEE Press.

[Garcia & Gould, 1980] Garcia, C. B. & Gould, F. J. (1980). Relations between several path-following algorithms and local and global newton methods. *SIAM Review*, 22(3), 263–274.

[Grbic & Eleftheriades, 2002] Grbic, A. & Eleftheriades, G. V. (2002). A backward-wave antenna base on negative refractive index L-C network. In *Progress in IEEE International Symposium on Antenna and Propagation and USNC/URSI National Radio Science Meeting, June 2002, San Antonio, USA*, volume 4 (pp. 340–343).

[Greivenkamp, 2004] Greivenkamp, J. E. (2004). *Field Guide to Geometrical Optics*. SPIE Press Book.

[Grigoropoulos et al., 2005] Grigoropoulos, N., Sanz-Izquierdo, B., & Young, P. R. (2005). Substrate integrated folded waveguides (SIFW) and filters. *IEEE Microwave Wireless Compon. Lett.*, 15(12), 829–831.

[Grigoropoulos & Young, 2004] Grigoropoulos, N. & Young, P. R. (2004). Compact folded waveguides. In *34th European Microwave Conference, Amsterdam, Holland, 12.–14.10.2004* (pp. 973–976).

[Guru & Hiziroğlu, 2004] Guru, B. S. & Hiziroğlu, H. R. (2004). *Electromagnetic Field Theory Fundamentals*. Cambridge Unveristy Press, second edition.

[Hamacher, 2006] Hamacher, K. (2006). Adaptation in stochastic tunneling global optimization of complex potential energy landscapes. *Europhysics Letters*, 74(6), 944.

[Hamacher & Wenzel, 1999] Hamacher, K. & Wenzel, W. (1999). The scaling behaviour of stochastic minimization algorithms in a perfect funnel landscape. *Physical Review E*, 59(1), 938–941.

[Harrington, 1968] Harrington, R. F. (1968). *Field Computation by Moment Methods*. New York: The Macmillan Co.

[Heaviside, 1888] Heaviside, O. (1888). On electromagnetic waves, especially in relation to the vorticity of the impressed forces, and the forced vibration of electormagnetic systems. *Philosophical Magazine*, 25, 130–156.

[Hong et al., 2006] Hong, W., Liu, B., Wang, Y., Lai, Q., Tang, H., Yin, X., Dong, Y., Zhang, Y., & Wu, K. (2006). A new guided wave structure for microwave and millimeter wave application. *Joint 31st International Conference on Infrared and Millimeter Waves and 14th International Conference on Terahertz Electronics*, (pp. 18–22).

[Hopfer, 1955] Hopfer, S. (1955). The design of ridged waveguides. *IRE Transactions on Microwave Theory and Techniques*, 10, 20–29.

[Ishimaru, 1991] Ishimaru, A. (1991). *Electromagnetic Wave Propagation, Radiation, and Scattering*. ISBN 0-13-249053-6. Prentice Hall.

[IYER & Eleftheriades, 2002] IYER, A. K. & Eleftheriades, G. V. (2002). Negative refractive index metamaterials supporting 2-D waves. In *2002 IEEE MTT-S International Microwave Symposium Digest, June 2–6, Seattle, USA*, volume 2 (pp. 412–415).

[Jibetean & de Klerk, 2006] Jibetean, D. & de Klerk, E. (2006). *Global Optimization of Rational Functions: A Semidefinite Programming Approach*. Open Access publications from Tilburg University urn:nbn:nl:ui:12-174725, Tilburg University.

[Jin, 2002] Jin, J. (2002). *The Finite Element Method in Electromagnetics*. New York: John Wiley & Sons, Inc.

[Kalos & Whitlock, 2008] Kalos, M. H. & Whitlock, P. A. (2008). *Monte Carlo Methods*. Wiley-VCH.

[Karageorchis, 2001] Karageorchis, A. (2001). The method of fundamental solutions for the calculation of the eigenvalues of the Helmholtz equation. *Applied Mathematics Letters*, 14, 837–842.

[Kavasseri, 2007] Kavasseri, R. G. (2007). A computational algegraic geometry based global optimization technique to address economic dispatch. In *IEEE Power Engineering Society General Meeting* (pp. 1–8).

[Keller, 1987] Keller, H. B. (1987). *Lectures on Numerical Methods in Bifurcation Problems*. Heidelberg, Germany: Springer Verlag.

[Keller, 1962] Keller, J. B. (1962). Geometrical theory of diffraction. *Journal of the Optical Society of America*, 52(2), 116–130.

[Kirkpatrick et al., 1983] Kirkpatrick, S., Gelatt, C. D., & Vecchi, M. P. (1983). Optimization by simulated annealing. *Science*, 220(4598), 671–680.

[Kitagawa, 1988] Kitagawa, T. (1988). On the numerical stability of the method of fundamental solution applied to the Dirichlet problem. *Applied Mathematics Letters*, 5, 123–133.

[Kitagawa, 1991] Kitagawa, T. (1991). Asymptotic stability of the fundamental solution method. *Journal of Computaional and Applied Mathematics*, 38, 263–269.

[Kittel, 1964] Kittel, C. (1964). *Introduction to Solid State Physics*. Wiley Text Books, seventh edition.

[Kong, 2009] Kong, J. A. (2009). *Electromagnetic Wave Theory*. New York, USA: Wiley Interscience, second edition.

[Kurokawa, 1958] Kurokawa, K. (1958). The expansions of electromagnetic fields in cavities. *IRE Trans. Microwave Theory Tech.*, MTT-6, 178–187.

[Liberti, 2008] Liberti, L. (2008). *Introduction to Global Optimization*. Online available at http://www.lix.polytechnique.fr/ liberti/teaching/globalopt-lima.pdf.

[Lu & Chew, 1995] Lu, C. C. & Chew, W. C. (1995). The use of Huygens' equivalence principle for solving 3D volume integral equation of scattering. *IEEE Transactions on Antennas and Propagation*, 43(5), 500–507.

[Luan & Tan, 2011] Luan, X. & Tan, K. (2011). A novel ridge substrate integrated waveguide antenna for WLAN application. In *International Workshop on Antenna Technology (iWAT)* (pp. 302–305).

[Luan & Tan, 2012] Luan, X. & Tan, K. (2012). Ultra-wideband bandpass filter based on ridged substrate integrated waveguide. In *International Conference on Microwave and Millimeter Wave Technology (ICMMT)*, volume 4 (pp. 1–4).

[Matyas, 1965] Matyas, J. (1965). Random optimization. *Automation and Remote Control*, 26(2), 246–253.

[Maxwell, 1873] Maxwell, J. C. (1873). *Treatise on Electricity and Magnetism.* Oxford: Clarendon Press.

[Metropolis & Ulam, 1949] Metropolis, N. & Ulam, S. (1949). The Monte Carlo method. *Journal of the American Statistical Association*, 44(247), 335–341.

[Michalski, 1985] Michalski, K. A. (1985). On the efficient evaluation of integrals arising in the Sommerfeld halfspace problem. *IEE Proceedings H, Microwaves, Antennas and Propagation*, 132(5), 312–318.

[Oliner, 2003] Oliner, A. A. (2003). A planar negative-refractive-index medium without resonant elements. In *2003 IEEE MTT-S International Microwave Symposium Digest, June 8–13, Philadelphia, USA*, volume 1 (pp. 191–194).

[Pendry et al., 1998] Pendry, J. B., Holden, A. J., Robbins, D. J., & Stewart, W. J. (1998). Low frequency plasmons in thin-wire structures. *Journal of Physics: Condensed Matter*, 10, 4785–4809.

[Pendry et al., 1999] Pendry, J. B., Holden, A. J., & Stewart, W. J. (1999). Magnetism from conductors and enhanced nonlinear phenomena. *IEEE Transactions on Microwave Theory and Techniques*, 47(11), 2075–2084.

[Pendry et al., 1996] Pendry, J. B., Holden, A. J., Stewart, W. J., & Youngs, I. (1996). Extremely low frequency plasmons in metallic mesostructure. *Physical Review Letters*, 76(25), 4773–4776.

[Pozar, 2004] Pozar, D. M. (2004). *Microwave Engineering.* Hoboken: Wiley.

[Russer, 2006] Russer, P. (2006). *Electromagnetics, Microwave Circuit and Antenna Design for Communications Engineering.* Artech House, second edition.

[Sanada et al., 2004] Sanada, A., Caloz, C., & Itoh, T. (2004). Planar distributed structures with negative refractive index. *IEEE Transactions on Microwave Theory and Techniques*, 52(4), 1252–1263.

[Schuhmann et al., 2005] Schuhmann, R., Lubkowski, G., & Weiland, T. (2005). Fullwave simulations and extraction of effective material parameters for left-handed metamaterials. In *German Microwave Conference (GeMIC)* Ulm, Germany.

[Schuster, 1904] Schuster, A. (1904). *An Introduction to the Theory of Optics.* London: Edward Arnold.

[Schwering & Peng, 1983] Schwering, F. K. & Peng, S. T. (1983). Design of dielectric grating antennas for millimeter-wave applications. *IEEE Transactions on Microwave Theory and Techniques*, 31(2), 199–209.

[Sievenpiper et al., 1999] Sievenpiper, D., Zhang, L., Broas, R. F. J., Alexopolous, N. G., & Yablonovitch, E. (1999). High-impedance surface electromagnetic surfaces with a forbidden frequency band. *IEEE Transactions on Microwave Theory and Techniques*, 47(11), 2059–2074.

[Smith et al., 2000] Smith, D. R., Padilla, W. J., Vier, D., Nemat-Nasser, S., & Schultz, S. (2000). Composit medium with simultaneously negative permeability and permittivity. *Physical Review Letters*, 84(18), 4184.

[Sommerfeld, 1949] Sommerfeld, A. (1949). *Partial Differential Equations in Physics*. Academic Press.

[Swendsen & Wang, 1986] Swendsen, R. H. & Wang, J. S. (1986). Replica Monte Carlo simulation of spin glasses. *Physical Review Letters*, 57, 2607–2609.

[Tamir & Oliner, 1963] Tamir, T. & Oliner, A. A. (1963). Guided complex waves. part 1: Fields at an interface. *Proceeding of the IEE*, 110(2), 310–324.

[Teixeira & Chew, 1996] Teixeira, F. L. & Chew, W. C. (1996). PML-FDTD in cylindrical and spherical grids. *IEEE Microwave and Guided Wave Lett.*, 7, 285–287.

[Tuy, 1998] Tuy, H. (1998). *Conves Analysis and Global Optimization*. Dodrecht: Kluwer Academic Publishers.

[Ufimtsev, 2007] Ufimtsev, P. Y. (2007). *Fundamentals of the Physical Theory of Diffraction*. Wiley-IEEE Press, first edition.

[Černý, 1985] Černý, V. (1985). Thermodynamical approach ot the traveling salesman problem: an efficient simulation algorithm. *Journal of Optimization Theory and Applications*, 45, 41–51.

[Veselago, 1968] Veselago, V. G. (1968). The electrodynamics of substances with simultaneously negative values of ε and μ. *Physics-Uspekhi*, 10(4), 509–514.

[Weise, 2008] Weise, T. (2008). *Global Optimization Algorithms Theory and Application*. Self-Published, second edition. Online available at http://www.it-weise.de/.

[Weitsch et al., 2011] Weitsch, Y., Chen, H., & Eibert, T. F. (2011). Dispersion analysis of periodic structures by solving corresponding excitation problems. *Frequenz*, 65(7-8), 247–252.

[Weitsch & Eibert, 2010] Weitsch, Y. & Eibert, T. F. (2010). Composite right-/left-handed interdigital leaky-wave antenna on a substrate integrated waveguide. In *European Conference on Antenna and Propagation (EuCAP), April 2010, Barcelona, Spain*.

[Weitsch & Eibert, 2011] Weitsch, Y. & Eibert, T. F. (2011). Eigenvalue computation of open periodically composed waveguides by series expansion. In *Progress in IEEE*

Antennas and Propagation Society International Symposium, July 2011, Spokane, WA, USA (pp. 321–324).

[Weitsch & Eibert, 2012] Weitsch, Y. & Eibert, T. F. (2012). Modal series expansion of eigensolutions for closed and open periodic waveguides. *IEEE Transactions on Antennas and Propagation*, 60(12), 5881–5889.

[Xu et al., 2006] Xu, F., Wu, K., & Hong, W. (2006). Domain decomposition FDTD algorithm combined with numerical tl calibration technique and its application in parameter extraction of substrate integrated circuits. *IEEE Transactions on Microwave Theory and Techniques*, 54(1), 329–338.

[Xu et al., 2007] Xu, F., Wu, K., & Hong, W. (2007). Finite-difference time-domain modeling of periodic guided-wave structures and its application to the analysis of substrate integrated nonradiative dielectric waveguide. *IEEE Transactions on Microwave Theory and Techniques*, 55(12), 2502–2511.

[Xu et al., 2003] Xu, F., Zhang, Y., Hong, W., Wu, K., & Cui, T. J. (2003). Finite-difference frequency-domain algorithm for modeling guided-wave properties of substrate integrated waveguide. *IEEE Transactions on Microwave Theory and Techniques*, 51(11), 2221–2227.

[Yang & Beck, 1998] Yang, C. M. & Beck, J. L. (1998). Generalized trajectory methods for finding multiple extrema and roots of functions. *Journal of Optimization Theory an Applications*, 97(1), 211–227.

[Yee, 1966] Yee, K. S. (1966). Numerical solution of initial boundary value problems involving Maxwell's equations. *IEEE Transactions on Antennas and Propagation*, 14(3), 302–307.